University of California
Santa Barbara

# Epitaxial Growth, Nanofabrication, and Mass Transfer of InGaN Micro-LEDs for Displays

A dissertation submitted in partial satisfaction
of the requirements for the degree

Doctor of Philosophy
in
Materials

by

David Hwang

Committee in charge:

Professor Steven P. DenBaars, Chair
Professor Shuji Nakamura
Professor James S. Speck
Professor Umesh K. Mishra

September 2018

The dissertation of David Hwang is approved.

---

Shuji Nakamura

---

James S. Speck

---

Umesh K. Mishra

---

Steven P. DenBaars, Committee Chair

July 2018

Epitaxial Growth, Nanofabrication, and Mass Transfer of InGaN Micro-LEDs for Displays



by

David Hwang

*To mom, dad, Jenny, and Lily for their endless and unwavering love*

*... and feeding me delicious food*

# Acknowledgments

"Give a man a fish, and you feed him for a day. Teach a man to fish, and you feed him for a lifetime." This quote has motivated me since high school and has been especially relevant in the last five years. My time in graduate school was not only a time to learn, but also a time to learn ***how to learn***. When I joined Professor Steven DenBaars's group, I knew very little about LEDs and even less about nitrides. Group meetings went over my head and the work being done was confusing. However, there was a great deal of support within my group, graduate program, and the greater Santa Barbara community. Without these supporters, I would not have finished this dissertation, and I owe them a great deal of gratitude.

To begin with, my advising committee has been an outstanding source of wisdom. Professor DenBaars has placed a great deal of trust in his students (including me) to work on cutting edge research. His optimism and openness to new and sometimes non-sensical ideas were enabling and allowed me to take risks. Professor Shuji Nakamura has also been very encouraging. His reception of my ideas was always positive, and he would propose alternative solutions and ideas to consider. Professor James Speck helped me focus on what was important. His desire to truly understand the science and mechanisms behind results made me think deeper about my work. Professor Umesh Mishra always inspired me to think of innovative solutions. After our conversations (either in his TMP course on innovation or in the hallway discussing results), I would always walk away learning something new or discovering new things to try in my research projects.

The work in this thesis would not have been possible without a host of staff. The Materials Department and SSLEEC administrative staff helped keep procedures orderly. They made it possible for me to do research and attend conferences without having to worry about expenses. The MOCVD staff, including Stacia Keller, Mike Iza, David Whitlatch, and Brian Carralejo, ensured the reactors were running and available to the students. The CNSI staff and MRL staff were also terrific in maintaining the host of characterization tools needed. Last but not least, the cleanroom staff was extremely attentive to students and users, and I cannot think of a better place to try out all these research ideas. UCSB is unique since there are such dedicated groups of people maintaining tools so students may focus on their research.

My research group mates were crucial to my initial education of nitrides and the execution of my research. From group meetings to whiteboard sessions, I learned an incredible amount from them. The μLED sub-group was also essential in helping carry out some of the work. In particular, I am grateful to Chris P, Asad, Matt, Lesley, Ryan L., and Pavel. Near the end, there were times when Matt, Ryan, and I would trade shifts in the cleanroom - someone would start a process in the morning and hand it off to the next person at night in order to accomplish my somewhat crazy timelines.

I would be remiss not to mention the incredible friends I've made throughout this journey. 1217 and my (f)roomates (Henrique, Brandon, Jon, Justin, and Nathan) truly helped me find a home at UCSB in my first year and kept things comical throughout graduate school. If I hadn't moved into the Mill House (Dan, John, Tobias, Anirudh, Chris Z., and Elliot), I probably would have graduated sooner. But then again, I would have lost my sanity, as my housemates were always there at the end of a long day to keep me motivated to work. Opal was a ridiculously educational and entertaining venture. From test driving cars to scropal, Chris P. and Asad were the best teammates one could have at the New Venture Competition.

The music community of Santa Barbara was a wonderful addition and distraction from research. I am forever grateful to have met and learned from Professor Margo Halsted and the carillon studio. The carillon has become such a big part of my life, and I am eager to continue traveling the world to play all the carillons. The Santa Barbara City College Orchestra has also been a tremendous source of relaxation and laughter. Although Jackie and I would be dead tired before our 3 hour rehearsals on Tuesday nights, Jim Mooy would always wake us up with a great selection of orchestral music and hilarious anecdotes.

Most importantly, I would not have been able to complete my PhD without my family (mom, dad, and Jenny) and my girlfriend Lily. Throughout their and my lifetimes, my parents have sacrificed a lot for Jenny and me. From the the expensive piano/violin lessons to driving nearly an hour to go to IB, my parents have stopped at nothing to ensure I do the best I can. Without Jenny (and her proofreading/editing of my college essays), I probably wouldn't have gotten into the schools I attended or been so successful in school. She also helped me in the tough times of transitioning to new environments. Finally, Lily has been a loving source of inspiration and motivation. Despite being in an extremely stressful period of life herself, she was always there encouraging me to finish. In addition, she was a huge help as an editor and proofreader. I dedicate this thesis to them and their endless love.

# Curriculum Vitæ

David Hwang
dhwang@ucsb.edu

## Education

**University of California, Santa Barbara**
**Ph.D. in Materials** — Santa Barbara, CA
Advisor: Professor Steven P. DenBaars — 2013-2018
GPA: 3.84, National Science Foundation Graduate Research Fellow

**University of Florida**
**B. S. in Materials Science and Engineering** — Gainevsville, FL
**Minor in Business Administration**
GPA: 3.98 (*summa cum laude*) — 2008-2013

## Academic & Industry Experience

- **Facebook Reality Labs** — Cork, Ireland
  *Research Scientist* — Employed as of August 2018

- **Apple, Inc** — Cupertino, CA
  *Emerging Displays Intern* — June 2017 – August 2017
  - Designed predictive models in LightTools to design light sources at the die, component, and system levels.
  - Automated simulations via MATLAB scripts to test various DOEs and generate over 500 runs.

- **UC Santa Barbara Materials Department** — Santa Barbara, CA
  *Graduate Student Researcher* — September 2013 – September 2018
  - Wrote and grew over 400 MOCVD recipes for III-nitride p-n diodes and LEDs on planar sapphire, patterned sapphire, and freestanding *c*-plane GaN.
  - Developed 6+ nanofabrication process flows and lithography mask layouts for flip-chip LEDs and $\mu$LEDs.
  - Modeled LED structures using Monte Carlo ray tracing in Synopsys LightTools software.
  - Trained and managed 6 graduate students in $\mu$LED growth, nanofabrication, testing, and characterization.
  - Set up a lab station combining photoelectrochemical etching and transfer printing for $\mu$LED mass transfer.

– Prepared 3 journal articles, wrote 3 patents, and presented in 6 conferences (national and international).

- **UC Berkeley Department of EECS** Berkeley, CA
  *Undergraduate Student Researcher (Summer REU)* July 2012 – August 2012
  - Investigated methods to create transistors using electrically-purified, single-chirality carbon nanotubes by doing thin-film deposition and using atomic force microscopy.
  - Fabricated full-color, flexible active-matrix organic light emitting diode devices.
  - Co-authored 1 publication, presented 1 poster presentation, and 1 oral presentation.

- **University of Florida MSE Department** Gainesville, FL
  *Undergraduate Student Researcher* August 2012 – May 2013
  - Studied the use of carboxymethyl cellulose as a binder for ZnS-cathodes in Li-ion batteries with Professor Kevin Jones.

- **Northwestern University** Evanston, IL
  *Undergraduate Student Researcher (Summer REU)* July 2011 – August 2011
  - Worked with transparent conducting oxides for plasmonic applications in Professor RPH Chang's group in the Materials Research Science and Engineering Center
  - Results: Developed a method to deposit a conformal layer of $SiO_2$ on ITO nanorods, resulting in contributions to "Infrared Plasmonics with Indium Tin-Oxide Nanorod Arrays" in Nano Letters.

- **General Electric Aviation** Cincinnati, OH
  *Materials Engineer Co-Op* January 2011 – May 2011
  - Conducted jet engine component analysis through non-destructive examination, sectioning, metallographic and SEM evaluation, and documentation for the major engine components.

## Refereed Journal Publications

6. M. S. Wong, **D. Hwang**, A. I. Alhassan, C. Lee, R. Ley, S. Nakamura, and S. P. DenBaars, "High efficiency of III-nitride micro-light- emitting diodes by sidewall passivation using atomic layer deposition," *Optics Express*, **26** (2018), 21324.

5. **D. Hwang**, A. Mughal, M. S. Wong, A. I. Alhassan, S. Nakamura, S. P. DenBaars, "Micro-Light-Emitting Diodes with III-Nitride Tunnel Junction Contacts Grown by Metalorganic Chemical Vapor Deposition," *Applied Physics Express*, **11** (2018), 012102.

4. C. D. Pynn, L. Chan, F. L. Gonzalez, A. Berry, **D. Hwang**, H. Wu, T. Margalith, D. E. Morse, S. P. DenBaars, M. J. Gordon, "Enhanced light extraction from free-standing InGaN/GaN light emitters using bio-inspired backside surface structuring," *Optics Express*, **25** (2017), 15778.

3. **D. Hwang**, A. Mughal, C. Pynn, S. Nakamura, S. P. DenBaars, "Sustained high external quantum efficiency in ultrasmall blue III-nitride micro-LEDs," *Applied Physics Express*, **10** (2017), 032101.

2. **D. Hwang**, B. P. Yonkee, B. SaifAddin, R. M. Farrell, S. Nakamura, J. S. Speck, S. P. DenBaars, "Photoelectrochemical liftoff of LEDs grown on freestanding c-plane GaN substrates," *Optics Express*, **24** (2016), 22875.

1. C. Wang, **D. Hwang**, Z. Yu, K. Takei, J. Park, T. Chen, B. Ma, and A. Javey, "User-interactive electronic skin for instantaneous pressure visualization," *Nature Materials*, **12** (2013), 899.

## Awards and Recognition:

Best Student Presentation Award Winner at the 11th International Symposium on Semiconductor Light Emitting Devices (ISSLED) October 2017

UCSB Outstanding Graduate Student Researcher Achievement Award (awarded by Professor Shuji Nakamura and SSLEEC Faculty) November 2016 and 2017

National Science Foundation Graduate Research Fellowship Recipient 2015 – 2018

UF Hall of Fame Inducted in Spring 2012

UF Asian Pacific Islander American (APIA) Hall of Fame Inducted in Spring 2012

Tau Beta Pi Florida Alpha Chapter Inducted in Spring 2012

UF Adamson Scholarship Fall 2009

## Selected Patents

2. US Provisional Patent entitled "Self-Emissive Inorganic LED-Based Display and Methods for Preparing the Same" (filed April 2016)
   Authors: David Hwang, Steven P. DenBaars, James S. Speck, and Shuji Nakamura

1. US Patent No. 62/069,644 (Patent Pending) and PCT Application entitled "FLEXIBLE ARRAYS OF MICRO-LEDS USING A PHOTOELECTROCHEMICAL (PEC) LIFTOFF TECHNIQUE" (filed late 2015)
   Authors: David Hwang, Nathan G. Young, Ben Yonkee, Burhan Saifaddin, Steven P. DenBaars, James S. Speck, and Shuji Nakamura

## Chaired Symposia

1. David Hwang, Natalie Larson, and Wennie Wang, "Transforming the Diversity Landscape," TMS 2016 Annual Meeting & Exhibition, Nashville, TN, Feb. 15, 2016.

## Invited Presentations

4. David Hwang, "LEDs: Enablers of the Future," FLIR, Goleta, CA, February 2, 2017.

3. David Hwang, Natalie Larson, Wennie Wang, "Highlights from the Transforming the Diversity Landscape Symposium: The Importance of Empathy on the Individual and Program Level," TMS DMMM2, Northwestern University, Evanston, IL, July 25, 2016.

2. David Hwang, Chris Pynn, Asad Mughal, "Opal: enabling brighter, thinner displays for smarter, more energy efficient devices," presented to the founder and executive board of Ixia, Calabasas, CA, July 20, 2016.

1. David Hwang, "LEDs: Enablers of the Future," UC Santa Barbara Board of Trustees Annual Meeting, Santa Barbara, CA, May 14, 2016.

## Research Presentations

7. David Hwang, Asad J. Mughal, Matthew S. Wong, Ryan Ley, Christopher D. Pynn, Abdullah I. Alhassan, Shuji Nakamura, Steven P. DenBaars, "Micro-Light-Emitting Diodes with III-Nitride Tunnel Junction Contacts Grown by Metalorganic Chemical Vapor Deposition," ICMOVPE 2018, Nara, Japan, June 3, 2018.

6. David Hwang, Asad J. Mughal, Christopher D. Pynn, Matthew S. Wong, Abdullah I. Alhassan, James S. Speck, Shuji Nakamura, Steven P. DenBaars, "High Efficiency, Ultrasmall InGaN $\mu$LEDs for Displays," 11th ISSLED, Banff, Canada, October 12, 2017.

5. David Hwang, Asad J. Mughal, Christopher D. Pynn, Lesley Chan, Dave Bothman, James S. Speck, Shuji Nakamura, Steven P. DenBaars, "Development of III-Nitride $\mu$LEDs for Display Applications," 2016 SSLEEC Annual Review, Santa Barbara, CA, November 3, 2016.

4. David Hwang, Benjamin Yonkee, James S. Speck, Shuji Nakamura, Steven P. DenBaars, "Development of c-plane thin-film flip-chip LEDs fabricated by photoelectrochemical (PEC) liftoff," CSW 2016, Toyama, Japan, June 26 - 30, 2016.

3. David Hwang, "LEDs: Lighting the Path to Futuristic Displays (and Cool Gadgets)," Grad Division and GSA Lunch & Learn, Santa Barbara, CA, June 3, 2016.

2. David Hwang, Benjamin Yonkee, James S. Speck, Shuji Nakamura, Steven P. DenBaars, "Flip-Chip GaN LEDs using Photoelectrochemical Liftoff," TMS 2016 Annual Meeting & Exhibition, Nashville, TN, Feb. 16, 2016.

1. David Hwang, Nathan G. Young, Benjamin Yonkee, Burhan Saifaddin, James S. Speck, Shuji Nakamura, Steven P. DenBaars, "Development of Photoelectrochemical (PEC) Liftoff of GaN devices," 2014 SSLEC Annual Review, Santa Barbara, CA, November 6, 2014 (Poster presentation).

## Competitions

**UC Santa Barbara Grad Slam 2016** Santa Barbara, CA
*Finalist* April 15, 2016

- Grad Slam is an award-winning campus-wide competition for the best three-minute talk by a graduate student hosted by the Graduate Division.
- Explained my technical research topic in general terms to lay audiences in a three minute speech to become one of ten finalists that had a starting field of 80 graduate students and won the People's Choice prize.

**UC Santa Barbara New Venture Competition 2016** Santa Barbara, CA
*Finalist and Cliff Hannel Innovation Award Winner (Team Opal)* May 19, 2016

- The New Venture Competition (NVC) is UC Santa Barbara's premier entrepreneurial experience, giving students a detailed understanding of how to launch their own successful technology start-up.

- Created a business model, analyzed potential markets, and conducted consumer surveys about a business idea formulated around the team's graduate research.
- Crafted and delivered a fifteen minute business pitch about a technical product to a panel of entrepreneurs and local business leaders.

**Macy's Challenge Marketing Case Competition** New York City, NY
*Regional and National Winner* April 2012

- Led my team to win the local UF competition and became a finalist in this national marketing competition.
- Designed a marketing campaign to attract millennials to Macy's stores.

**Disney's Creative Inc. Case Competition** Orlando, FL
*Winner* July 2011

- Created a social-media based marketing campaign for a Disney event and recommended strategies with social networks (Facebook, Twitter, YouTube, UStream), QR codes, and augmented reality.

**Capital One Business Case Competition** Richmond, VA
*Finalist* July 2010

- Came up with a new solution (in the form of a college lifestyle friendly credit card) to attract college students to Capital One and make them lifetime customers.

## Teaching Experience

**UCSB Materials Department** Santa Barbara, CA
*Teaching Assistant* April 2016 – June 2016

- Taught sections and held office hours for a graduate level course (MAT227) on metalorganic chemical vapor deposition (MOCVD) taught by Professor Steven DenBaars
- Course evaluations indicated "excellent" (55%) and "very good" (45%) performance.

**UF Chemistry Department** Gainesville, FL
*Teaching Assistant* January 2009 – December 2010

- Taught a discussion section as a freshman one hour a week for General Chemistry 2 (CHM2046) under Professor James Horvath and held weekly office hours in the Chemistry Learning Center, and 40% of my students earned grades of A

## Outreach

UCSB NSF GRFP Workshop and Panel — Santa Barbara, CA
*Panelist* — October 5, 2016

Congressional Visits Day (sponsored by Material Advantage) — Washington, DC
*Attendee* — April 18 - 19, 2016

Visited CA Representatives of Congress to discuss the importance of funding for research in basic science and engineering.

S&T MESA Day (hosted by UCSB MESA, SASE, LI, NSBE) — Santa Barbara, CA
*Volunteer Judge, Science Demo Volunteer* — 2015, 2016

Demonstrated concepts relating to fiber optics and waveguiding to K-12 students

Family Ultimate Science Exploration (sponsored by UCSB CNSI) — Santa Barbara, CA
*Volunteer* — 2014, 2015

It's a Materials World (sponsored by UCSB MRL) — Santa Barbara, CA
*Volunteer* — 2014, 2015

Buckyball Workshop (sponsored by UCSB MRL) — Santa Barbara, CA
*Volunteer* — November 9, 2015

NanoDays (sponsored by UCSB CNSI) — Santa Barbara, CA
*Volunteer* — 2014, 2015

Santa Barbara County K-12 Science Fair — Santa Barbara, CA
*Judge* — March 6, 2015

Engineers Week — Gainesville, FL
*Volunteer* — 2011, 2012

## Abstract

Epitaxial Growth, Nanofabrication, and Mass Transfer of InGaN Micro-LEDs for Displays

by

David Hwang

High efficiency III-nitride light-emitting diodes (LEDs) have drastically improved solid-state lighting. They are sold in stores and are gradually replacing compact fluorescent lightbulbs because they use less power and last longer. III-nitrides are on the cusp of entering another market. As the size of mobile electronics shrink over time, display technologies must also move to smaller form factors while maintaining high efficiencies. To achieve these goals, III-nitride LEDs are once again a candidate to overtake the state of the art.

Incumbent technologies, such as liquid crystal displays (LCDs) and organic LED (OLED) displays, have major issues with power efficiency. A new technology, termed the micro-LED (µLED) display, is poised to enter the market in the next few years. A µLED display is made of inorganic LEDs (such as InGaN or AlGaInP) with dimensions typically below 40 µm. µLED displays are promising due to higher luminance (brightness) than OLEDs, wider viewing angles, and significantly higher energy efficiencies.

In this thesis, advances in InGaN µLED epitaxial design, nanofabrication, and mass transfer are discussed. Chapter 1 introduces the III-V families (arsenides, phosphides, nitrides) and provides insight into µLED design. While the majority of IngaN µLEDs are grown on sapphire or silicon, there are many reasons to explore homoepitaxial growth on freestanding GaN (particularly on semipolar planes). Chapter 2 presents a comparison of external quantum efficiency (EQE) amongst various sized µLEDs and shows that high EQEs (40-45%) are sustained as the size of the µLED drops. Reasons for efficiency loss

are presented and designs aimed at improving μLED efficiencies are highlighted. Chapter 3 discusses the incorporation of tunnel junction contacts to μLEDs to enable new design space ($n$-type mirrors and multiple active region growths). Chapter 4 examines ideas to eliminate the drop of efficiency with decreasing μLED size that incorporates a current aperture and reduction of dry etch damage at the active region sidewall. Chapter 5 highlights a new mass transfer method that is applicable to μLEDs grown on freestanding GaN, sapphire, or other substrates. Most of the commercial mass transfer techniques today use laser lift-off (LLO), which is incompatible with μLEDs grown on freestanding GaN. The technique in Chapter 5 combines photoelectrochemical (PEC) etching and transfer printing. With this method, red, green, and blue InGaN μLEDs have been transferred from their growth substrates (sapphire and freestanding GaN) to the same transparent and/or flexible substrates such as glass or acrylic without damage to the μLED. This thesis reports the first demonstration of red, green, and blue μLEDs all with an InGaN active region that have been transferred to the same substrate.

# Contents

# Chapter 1

# Introduction

## 1.1 Brief overview on displays

Display technologies surround our everyday lives. They feed information from our wrists as smartwatches, live in our pockets as smartphones, entertain us in our homes as large screen televisions, and flash advertisements on the street as store signs or digital billboards. Displays may be as simple as monochromatic (or even black and white) indicators or as complex as full-color (red, green, and blue, or RGB) displays. Full-color displays are made of pixels that have three sub-pixels (red, green, and blue) as shown in Figure 1.1. Beyond these applications, emerging technologies include near-eye displays (smartglasses or contact lens displays) and 3D displays (light-field or holographic displays) [1]. While many of these emerging displays have been portrayed in movies (advanced technologies of superheroes or spies), they have been demonstrated in academic settings, prototyped, or tested in the market.

Some of the earliest displays were cathode ray tubes (CRTs) from the late 1800s/early 1900s and were found in TVs and computer monitors amongst other applications. Inside

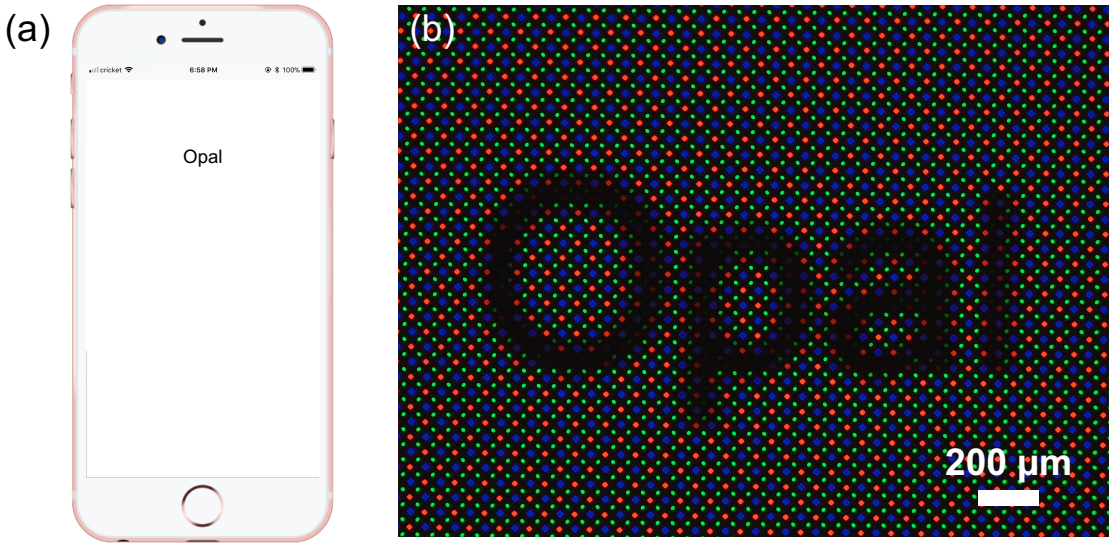


Figure 1.1: A smartphone with the text "Opal" on the screen. (a) Optical photograph and (b) optical micrograph of the display showing the RGB sub-pixels. Pixels are on the order of 10-20 µm for a pitch of ∼400 ppi.

the CRT is a vacuum tube with electron guns that served as the sources of light for the display. Electrons are accelerated and deflected (by electrostatic or magnetic deflection) towards RGB phosphor-coated screens. The electron guns are swept in a raster pattern to form the desired image. CRTs were the dominant display technology until they were replaced by liquid crystal displays (LCDs) around the early 2000s.

The light sources for LCDs are highly efficient blue light-emitting diodes (LEDs) made of GaN-based materials that are phosphor converted to white light. A strip of these white LEDs serve as the backlight unit (BLU) for the LCD, which may be physically located on the side of the display as in the case of TVs and computer monitors. This light is guided through various films (optical polarizers, liquid crystals, color filters, etc) to an array of pixels. Light is first guided through a polarizer to convert all of the randomly polarized light into polarized light. This polarized light passes through liquid crystals, where the orientation of the light may be rotated, and then goes through a second polarizer oriented

90° from the first polarizer. Because of the numerous layers, LCDs have limitations ins form factor (physically bulky) and energy efficiency due to large losses in the layers (∼3 to 5%). LCDs are "always on" because the BLU is always turned on; black screens are produced when the second polarizer absorbs or blocks the polarized light passed through the first polarizer and liquid crystals. Therefore, these black images still have some light that leaks through them. Despite these shortcomings, LCDs still have a big presence in television, computer monitor, and smartphone markets.

More recently, organic LED (OLED) displays entered the display market. Instead of using BLUs as light sources, the light source of the OLED display pixels are the OLEDs themselves. Thus, this type of display is self-emissive. OLED displays have been advertised as having darker blacks, higher contrast ratios, and lower power consumption. Pixels are only turned "on" when the individual OLEDs are turned on, so darker blacks and higher contrast ratios are possible. Compared with LCDs, OLED displays have fewer layers that absorb or block the light and thus have lower power consumption (∼10-20%). However, OLEDs have limited efficiencies due to the light generation mechanisms of OLED materials [2]. In OLEDs, electrons and holes recombine to form excitons, which are bound carriers. Light is emitted when this excited state decays. Excitons may either be in a singlet state (spin quantum number $s = 0$ with one spectral line) or triplet state (spin quantum $s = -1$, 0, or $+1$ and three states), and the probabilities for a singlet and triplet are 25% and 75%, respectively. In fluorescent organic molecules, decay of triplets is forbidden quantum mechanically, so the internal quantum efficiency (IQE) is limited to 25%. Phosphorescent materials may generate light from both singlets and triplets, so their efficiencies may be higher [3–6].

## 1.2 Motivation for inorganic µLED-based displays

High efficiency III-nitride light-emitting diodes (LEDs) have already drastically improved solid-state lighting and are steadily replacing compact fluorescent lightbulbs and other illumination sources [7,8]. As the size of portable and mobile electronics shrink over time, display technologies must also move to smaller form factors, reach ultra-high resolutions, and have high brightnesses while maintaining high efficiencies to prolong battery life. To achieve these goals, III-nitride LEDs are once again a candidate to overtake the state of the art.

µLEDs offer advantages over their large-area LED counterparts and over other types of displays (namely, LCDs and OLED displays). By reducing the pixel size to the order of micrometers, higher resolutions may be achieved as smaller pitches are possible. This shrinking also leads to potential improvements in transparency, thinness, and flexibility. µLED displays are self-emissive and only turn on pixels when needed. This emission mechanism allows for the same dark blacks and high contrast ratios as OLED displays. µLED displays offer higher luminance (brightness) levels, luminous efficacies, and longer lifetimes than their OLED counterparts [9, 10]. Several groups have fabricated single-color µLED-based arrays with pixels dimensions as small as 12 µm [9–13]. This self-emissive technology may be used in applications where high resolution, brightness, and efficiency are necessary, such as smartphones, smartwatches, head-mounted and near-eye displays [14], and picoprojectors [15]. Luminances have reached levels on the order of millions of nits [16], which is magnitudes of order higher than luminances OLEDs (∼tens of thousands of nits) [17].

To create µLED displays, pixel sizes must be reduced to 10 µm or smaller to increase the resolution and lower the cost. Since the light source of a µLED display is the µLED, a much higher number of µLEDs are needed than the number of LEDs required for LCD

BLUs. While LED costs have been reduced to fractions of cents, the number of µLEDs needed for large µLED displays is significant. Cost reduction may be done by decreasing the µLED size (and increasing the number of µLEDs per epitaxial wafer).

The choice of materials to be used for the RGB µLEDs is shown in Figure 1.2. The III-nitride family spans the entire visible spectrum by alloying GaN with InN or AlN, but there is a large lattice constant mismatch associated with such alloying. On the other hand, the III-phosphide family may span the yellow-green to red spectrum while staying lattice matched with GaAs. One figure of merit that may inform the material selection (and that has been used in the solid-state lighting field) is the external quantum efficiency (EQE). EQE is a measure of the light output power that escapes the LED divided by the number of electrons that are injected into the LED. Conventional wisdom says that red LEDs would be made out of AlGaInP, whereas green and blue LEDs would be made out of InGaN. External quantum efficiencies (EQEs) of inorganic LEDs have reached 50-60% for red AlGaInP LEDs [18], 40% for green InGaN LEDs [19], and 80-90% for blue InGaN LEDs [20]. However, red AlGaInP µLEDs have been shown to suffer from dramatic drops in EQE (see Figure 1.3). [21,22], so the III-nitride system may be needed to make a truly self-emissive full-color display. The following sections will briefly discuss the two material systems.

## 1.3 Overview of AlGaInP/GaAs

In general, LED epitaxy requires semiconductors with a direct bandgap, $p$- and $n$-dopants to form a $p$-$n$ junction, and substrates with similar lattice constants to the semiconductor. Light emission from a direct bandgap semiconductor only requires an electron and hole (two-body process). Light emission from an indirect bandgap semiconductor is a phonon-assisted process because of the difference in momentum (three-body). This three-

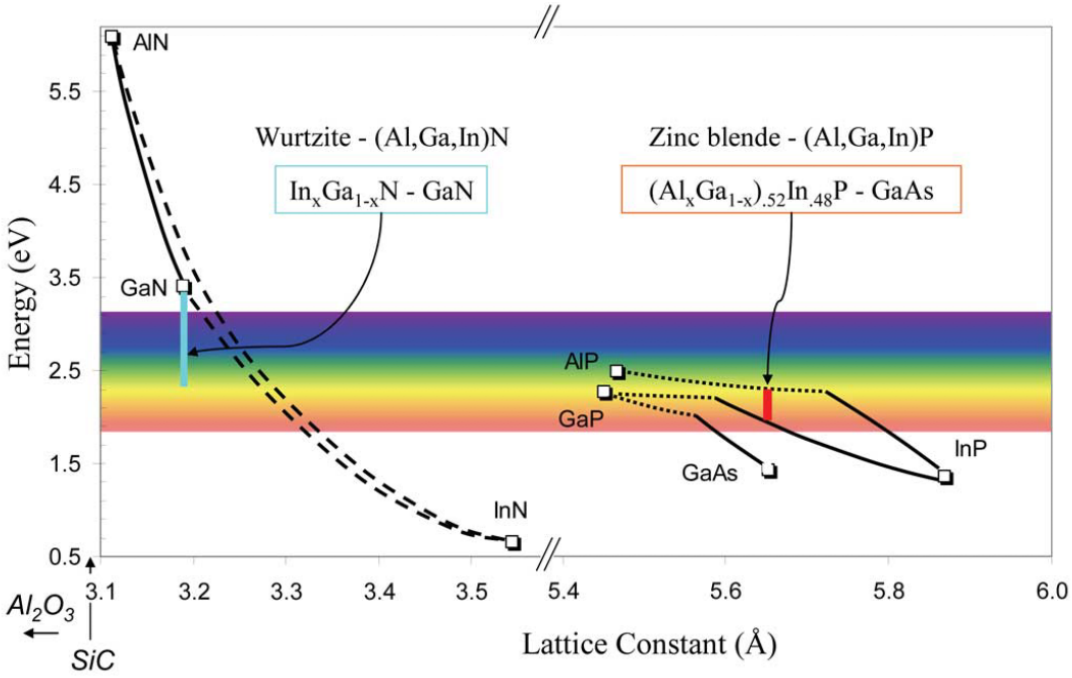


Figure 1.2: Energy (eV) or wavelength (nm) versus lattice constant (Å) for the III-N and III-P systems. Figure © 2007 IEEE [23].

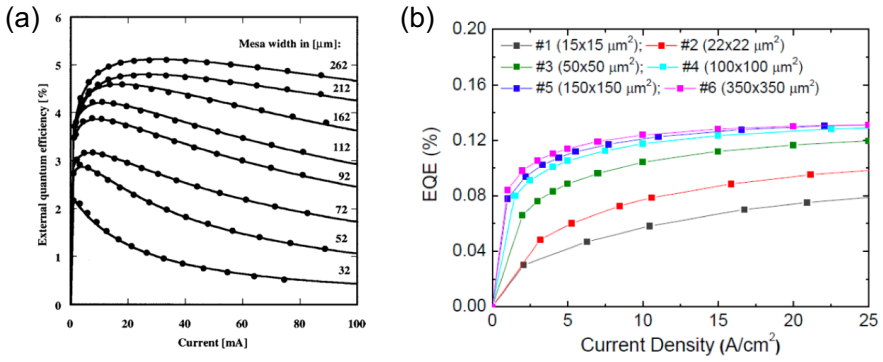


Figure 1.3: EQE versus µLED size measured by (a) Royo *et al.* (Reprinted from [P. Royo, R. P. Stanley, and M. Ilegems, *J. Appl. Phys.*, **91**, 2563 (2002)], with the permission of AIP Publishing) [21] and (b) Oh *et al.* [22].

body process is much less probable than a two-body process. For the conventional III-V semiconductors (III-phosphide and III-arsenides), similar lattice constants between semiconductor and substrate are essential to minimize dislocations that serve as nonradiative recombination sites. Dislocation densities above $10^4$ cm$^{-2}$ lead to tremendous losses in IQE [24]. The first red (and visible) LED was developed by Holonyak *et al.* in 1962 using GaAsP [25]. However, LEDs using GaAsP suffered from poor efficiencies due to lattice mismatch. Decades later, high efficiency red LEDs using AlGaInP grown on GaAs substrates were commercialized in the early 1990s [26–28]. AlGaInP and GaAs both have the zinc blende crystal structure, which has a face-centered cubic (FCC) lattice.

$(Al_xGa_{1-x})_yIn_{1-y}P$ is lattice matched to GaAs when $y$=0.48. InGaP ($x = 0$) has a direct bandgap (conduction band minimum is on the $\Gamma$ valley), but AlInP ($x = 1$) has an indirect bandgap ($X$ valley). The crossover between direct and indirect bandgap occurs around $x = 0.55$, which gives a bandgap of 2.24 eV or 553 nm. However, the densities of states in the indirect valleys is higher than that in the gamma valley, so occupation of indirect valleys is significant even below $x = 0.55$. Nevertheless, AlGaInP is usually the material of choice for the yellow-orange-red regime.

Although AlGaInP is lattice matched to GaAs, GaAs is opaque and absorbs in the visible spectrum. Many of the first LEDs kept the GaAs substrate (and have been referred to as "absorbing substrate LEDs"), and their EQEs were limited to below 2% [29, 30]. To avoid this issue, "transparent substrate LEDs" were created. GaP is a transparent substrate, but high quality AlGaInP cannot be grown on GaP due to its large mismatch. To create transparent substrate LEDs, AlGaInP LEDs are wafer bonded to a GaP wafer, and the GaAs is removed by a chemical etch [31–33]. Another major issue with AlGaInP LEDs is the light extraction and internal loss of light, and eventually, chip-shaping led to the state of the art red LED efficiencies. Krames *et al.* created truncated-inverted-pyramid (TIP) LEDs (Figure 1.4) by using angled dicing blades to improve the light

extraction. These LEDs reached peak efficiencies of 60.9% and 55% under pulsed and continuous wave measurements, respectively (emission wavelength of 650 nm) [18].

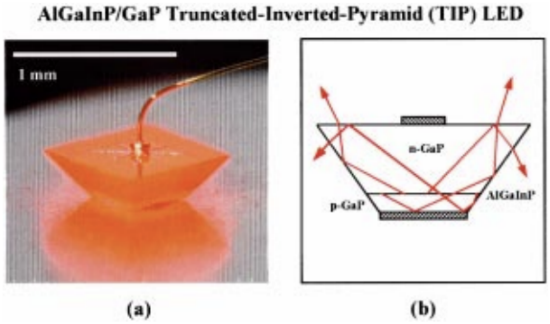


Figure 1.4: (a) Photomicrograph of a TIP LED; (b) schematic cross section showing means by which photons are redirected by total internal reflection (Reprinted from [M. R. Krames, M. Ochiai-Holcomb, G. E. Hofler, C. Carter-Coman, E. I. Chen, I.-H. Tan, P. Grillot, N. F. Gardner, H. C. Chui, J.-W. Huang, S. A. Stockman, F. A. Kish, M. G. Craford, T. S. Tan, C. P. Kocot, M. Hueschen, J. Posselt, B. Loh, G. Sasser, and D. Collins, *Appl. Phys. Lett.*, **75**, 2365 (1999)], with the permission of AIP Publishing) [18].

## 1.4 Overview of InGaN/GaN

GaN has the wurtzite crystal structure, which is hexagonal and shown in Figure 1.5. The wurtzite structure is non-centrosymmetric and lacks inversion symmetry, has polar bonds (gallium atoms bonded to nitrogen atoms), and has alternating layer of gallium and nitrogen. Due to these alternating layers, the charges within the bulk cancel each other out, but fixed sheet charges exist at the surface (negative at Ga face and positive at N face). When $c$-plane GaN is grown (in the $c$-direction, or [0001]), a spontaneous polarization exists in the $[000\bar{1}]$ direction, which leads to a polarization-induced electric field. This alignment of growth direction with spontaneous polarization is why the $c$-plane family $\{0001\}$ is termed the polar plane. Nonpolar planes exist and are orthogonal to $c$-plane. These nonpolar planes include the family of $a$-planes $\{11\bar{2}0\}$ and the family

of $m$-planes $\{10\bar{1}0\}$. These planes are charge neutral since each plane contains both gallium and nitrogen atoms, and no polarization exists along the growth direction. In between polar and nonpolar are the semipolar planes, which are planes that have at least two nonzero $h$, $i$, or $k$ Miller indices and a nonzero $l$ Miller index. Some examples include $(11\bar{2})$, $(20\bar{2}1)$, $(20\bar{2}\bar{1})$, $(30\bar{3}1)$, and $(30\bar{3}\bar{1})$. These planes have reduced but nonzero polarization fields.

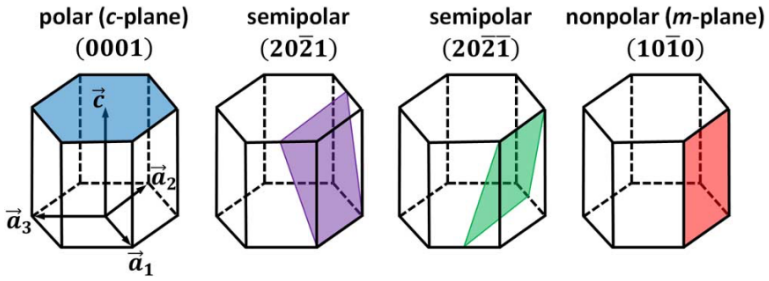


Figure 1.5: Orientations of GaN: polar $c$-plane (0001) (blue), semipolar $(20\bar{2}1)$ (purple), semipolar $(20\bar{2}\bar{1})$ (green), and nonpolar $m$-plane $(10\bar{1}0)$ (red). Figure © 2011 IEEE [34].

In addition to the spontaneous polarization, a piezoelectric polarization is induced by strain of the lattice. One relevant example is when InGaN is grown on GaN. As InN has a larger lattice constant than GaN, pseudomorphic growth of InGaN on GaN results in compressive strain of the crystal. This strain leads to charge generation, which gives a piezoelectric polarization in the [0001] direction (opposite of the spontaneous polarization direction). Piezoelectric polarization also exists when AlGaN is grown, but AlN has a smaller lattice constant that produces tensile stress. A major consequence of the polarization is the quantum-confined Stark effect (QCSE) [35]. The QCSE on InGaN/GaN may be visualized by the band diagram in Figure 1.6. Absent any polarization and electric fields, the bands are flat (Figure 1.6(a)). The polarization induced electric field tilts the bands, which spatially separates the electron and hole wavefunctions and reduces the energy gap between the conduction band minimum and valence band maximum (Figure

1.6(b)). These two effects lead to a reduced probability of radiative recombination (proportional to the square of the wavefunction overlap) and a red-shift of emission. However, with higher injection current, the fields are screened by carriers (Figure 1.6(c)), and the emission is blue-shifted.

GaN has been grown on a multitude of substrates either heteroepitaxially (silicon, silicon carbide and sapphire) or homoepitaxially (on freestanding GaN). When growing on foreign substrates, a seed/nucleation layer is grown at low temperatures first ($500 - 600°$C). The temperature is then raised to above 1000°C to coalesce the GaN. When growing heteroepitaxially, threading dislocation densities (TDD) may reach the order of $10^8$ cm$^{-2}$ and higher. When growing on freestanding GaN, a nucleation layer is unnecessary, and TDDs are of the order of $10^5 - 10^6$ cm$^{-2}$. Compared with the conven-

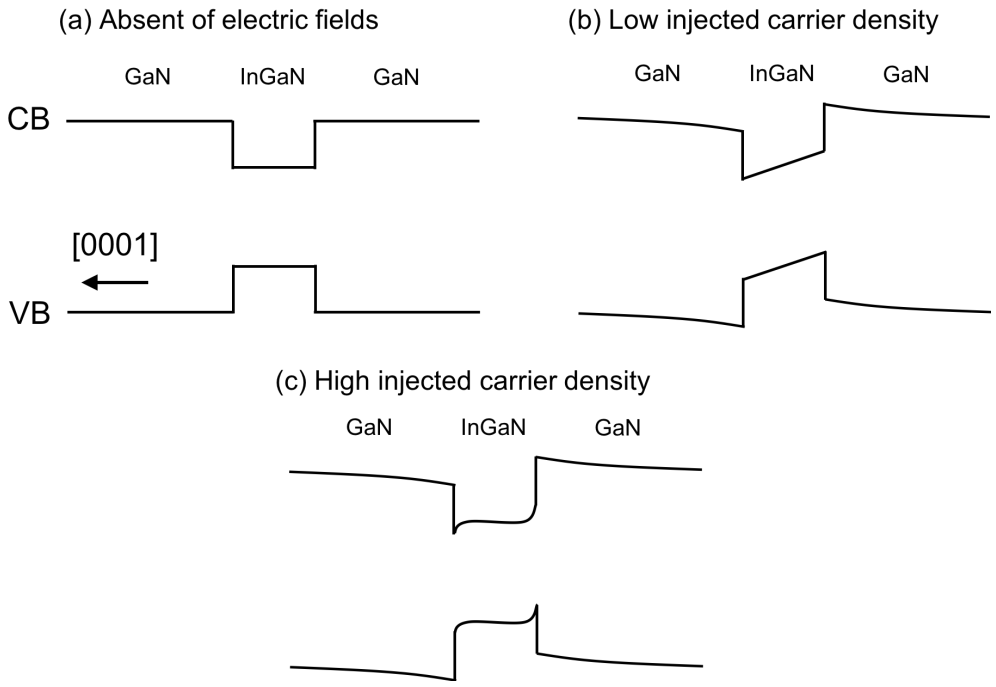


Figure 1.6: Schematic of band diagrams of InGaN quantum well/GaN barrier showing the quantum-confined Stark effect. (a) Flat bands without electric field, (b) tilted bands with polarization effects at low current, and (c) tilted bands at high current with screened carriers.

tional III-Vs (III-arsenides and III-phosphides), this dislocation density is tremendous, but light emission is still possible.

For growth of InGaN LEDs on foreign substrates, growths have predominantly been for $c$-plane although there have been studies on semipolar LEDs grown on silicon [36] and sapphire [37, 38]. One of the major challenges facing LEDs is the green gap and pushing to longer wavelengths with InGaN. For green, the highest EQE is around 42% [19] and was achieved by tuning the morphology of the active region. AlGaN barriers were incorporated to compensate for the strain generated by the InGaN and grown at higher temperatures to smooth out the morphology.

Besides optimizing growth to minimize defects, semipolar planes may be used because they have reduced polarization fields that lead to higher wavefunction overlap. Figure 1.7 shows that LEDs grown on $(20\bar{2}\bar{1})$ exhibited the most stable wavelength with current density and the narrowest line widths (lowest full-width at half max (FWHM)) [39]. Furthermore, other semipolar planes may be able to reach even longer wavelengths and enter the red regime. In general, emission wavelengths from InGaN grown on planes with higher inclination angles from $m$-plane were higher than that of $m$-plane [40]. The wavelengths of LEDs grown at the same temperature on $(11\bar{2}2)$, $(20\bar{2}1)$, and $m$-plane were 490, 438, and 415 nm, respectively. The inclination angles (from $m$-plane) of those planes are 32°, 15° toward $+c$-plane, and 0°, respectively.

## 1.5 Synopsis

This thesis will describe epitaxial growth, nanofabrication, and mass transfer of µLEDs for display applications. The µLED efforts at UCSB started around 2014 (4 years before time of press). Chapter 2 will detail the initial studies on µLED characterization. While many groups have studied the size-dependence of optoelectronic properties, the absolute

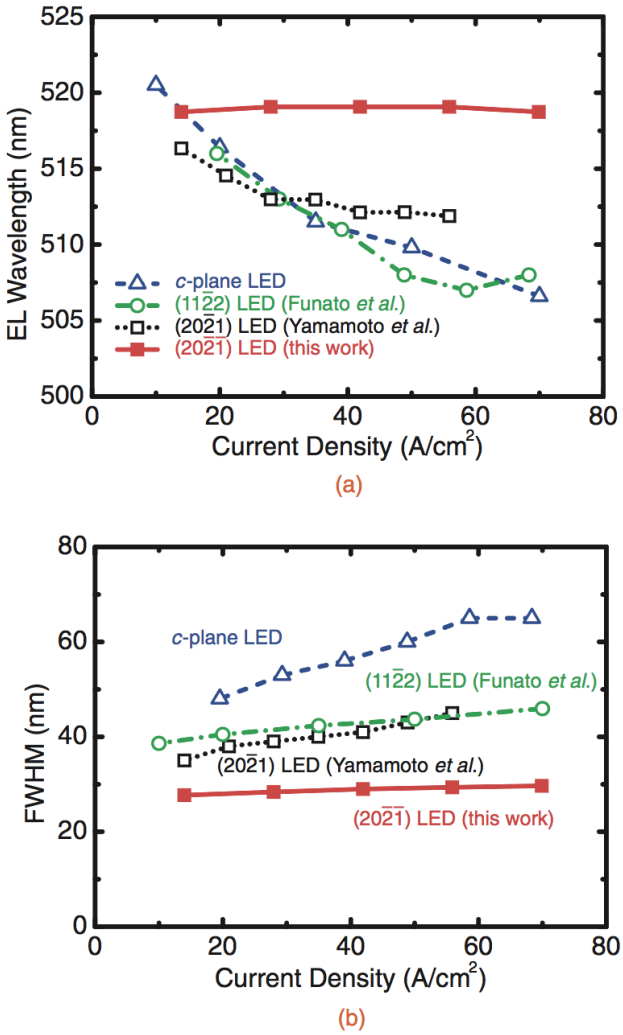


Figure 1.7: (a) Electroluminescence peak wavelength and (b) FWHM as functions of current density for the green (20$\bar{2}\bar{1}$) single quantum well LED. Copyright 2013 The Japan Society of Applied Physics [39].

EQEs were low (below 10%). Chapter 2.2 shows that high EQEs (40 to 50%) were sustained when reducing µLED dimensions from 100 µm to 10 µm. Reduction of EQE was attributed to the increasing perimeter to surface area ratio. Effects of passivating the sidewall with dielectric were also investigated to show that silicon oxide deposited by atomic layer deposition (ALD) suppressed reverse leakage current and improved EQE.

Chapter 3 discusses the use of tunnel junction contacts for µLEDs. GaN tunnel junction contacts have been shown to add large voltage penalties to large area InGaN LEDs because of incomplete activation. Activation is achieved by lateral diffusion of hydrogen, and since µLED dimensions are greatly reduced, activation may be possible. The use of tunnel junctions is useful for growing multiple LED active regions (potentially monolithic growth of different colored µLEDs) and for using $n$-type mirror contacts instead of tricky $p$-type mirrors (terminating the surface with $n$-GaN instead of $p$-GaN).

Since the mesa sidewall is an important feature of the µLED, Chapter 4 proposes a nanofabrication process that spatially separates the mesa sidewall and the active region sidewall. A mesa is typically etched in order to contact the $n$-GaN. If a current aperture is created to selectively confine holes to an area far from the mesa sidewall, less non-radiative recombination may occur. Here, ion implantation was used to define this current aperture, and other methods are suggested.

Finally, Chapter 5 presents a mass transfer method that is applicable not only to heteroepitaxially grown µLEDs on sapphire but also to homoepitaxially grown µLEDs on freestanding GaN substrates. All commercial techniques hitherto use a laser lift-off (LLO) method to release µLEDs from sapphire. There is much promise for µLEDs grown on freestanding GaN, but LLO is incompatible with such µLEDs. The proposed mass transfer process combines the use of lateral photoelectrochemical (PEC) etching and transfer printing. With this technique, red, green, and blue InGaN µLEDs were transferred to the same transparent and flexible acrylic substrate (see Figure 1.8 for a

preview). This thesis offers the first demonstration of red, green, and blue InGaN µLEDs (neither AlGaInP nor phosphor-converted) transferred to the same substrate.

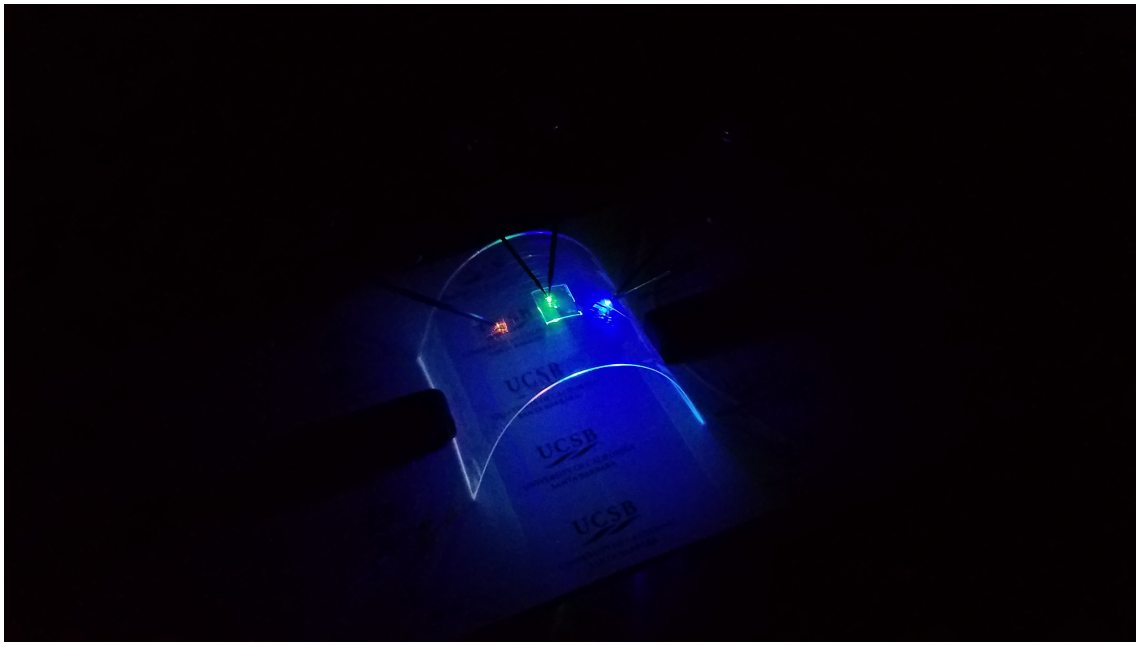


Figure 1.8: Optical photograph of red, green, and blue µLEDs on the same transparent and flexible substrate (acrylic) electrically lit up. The active region of the µLEDs were comprised of InGaN and not AlGaInP. See Chapter 5 for details of growth and fabrication.

# Chapter 2

# Initial Studies on Blue InGan µLEDs

## 2.1 Motivation for µLEDs

As discussed in Chapter 1, incumbent technologies (LCDs and OLED displays) are unable to meet requirements for future and emerging displays. These displays are likely to penetrate mobile and portable electronics markets, including smartphones, smartwatches, head-mounted and near-eye displays (for virtual reality (VR) or augmented reality (AR) applications), and picoprojectors. In these applications, some requirements include high brightnesses (high light output), low power consumption (high efficiencies), directionality (narrow emission patterns), ultra-high resolution (small pixels and small pixel pitches) and flexible form factor, to name a few. Ultra-high resolutions require that the light-emitting pixel sizes be reduced to around 10 µm or smaller. Academic interest in µLEDs has been steadily increasing since the year 2000. One of the first groups to study µLEDs is that of Professor Hong Xing Jiang at Kansas State University (currently at Texas Tech University) [11, 41–44]. Early work showed that an array of connected µLEDs could emit more light than a conventional large-area LEDs and advocated for the use of µLEDs

for solid-state lighting [41]. As shown in Figure 2.1, an array of small 10 µm diameter LEDs was fabricated to cover the same area as a 300 µm × 300 µm LED. Soon after, Jiang *et al.* created microdisplays for high resolution viewing or projection [42]. Several other groups have also fabricated single-color µLED-based arrays with pixel dimensions as small as 12 µm [9–13]. Many of these works dealt with the integration of single-color µLED arrays with Si CMOS technology and driving architectures.

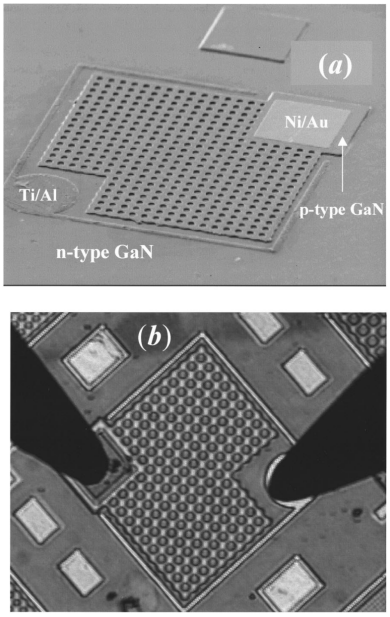


Figure 2.1: (a) SEM and (b) optical microscope images of approximately 200 interconnected µLEDs situated in an area of 300 × 300 µm$^2$. Reprinted from [S. X. Jin, J. Li, J. Y. Lin, and H. X. Jiang, *Appl. Phys. Lett.*, **77**, 3236 (2000)] with the permission of AIP Publishing [41].

In addition to the aforementioned display demonstrations, more fundamental studies aiming to characterize the performance of individual µLEDs have also been done. Commonly discussed attributes of µLEDs over their large-area counterparts include improved thermal management [45], enhanced light extraction [41,46], operation at higher current densities [47], and faster turn-on speeds [43] (which lends their use to visible light communication [48]). Despite these benefits, surface recombination at small dimensions has

been noted as a source of reduced quantum efficiencies (both internal quantum efficiency (IQE) and external quantum efficiency (EQE)) across the III-V family of compound semiconductors. For red AlGaInP LEDs, Royo *et al.* [21] and Oh *et al.* [22] fabricated devices and showed that the internal quantum efficiencies (IQEs) and external quantum efficiencies (EQEs) dropped as much as 5x with decreasing size. For blue InGaN LEDs, there have been some experimental [49, 50] and theoretical [51, 52] studies. Olivier *et al.* showed a ∼30% drop in EQE from a 100 µm diameter LED to a 10 µm diameter LED, although their efficiencies were very low (below 10%) [50]. In these experimental studies, the µLED measurements were done on chip. Silver *p*-contact mirrors were deposited on top of the mesa, and light output was measured out the backside of the sapphire substrate with a broad area photodetector. With this method, only a fraction of the light was collected by the photodetector. Bulashevich *et al.* created a hybrid LED model to study current spreading, heat transfer, carrier injection, and recombination and fit experimental data from the literature [51]. Their findings showed that surface recombination may actually reduce the maximum wall-plug efficiency by 5-7 percentage points. Konoplev *et al.* predicted more uniform current distribution in smaller LEDs (and more current crowding in large LEDs) and higher surface recombination for smaller LEDs [52].

Since smaller µLEDs have larger perimeter to area ratios, the effects at the sidewall becomes significantly more important. Chapter 2.2 shows the effects of µLED size while sustaining high EQEs. µLEDs were packaged and measured in a calibrated integrating sphere to collect all the light emitted from the chip. Chapter 2.3 further analyzes the quantum efficiencies of the µLEDs of Chapter 2.2 by using the ABC model for IQE. The B coefficient was assumed to be independent of size and carrier density, and A and C coefficients were extracted by curve fitting. Chapter 2.4 will discuss some sidewall passivation to provide further improvements to µLED designs. Finally, Chapter 2.5 will summarize the results of this chapter and provide future directions to improve InGaN

µLEDs. Since the sidewall becomes a critical feature with diminishing size, suggestions on how to minimize or even prevent nonradiative recombination at the sidewall will be offered.

## 2.2 Sustained high EQE of InGaN µLEDs

### 2.2.1 Experimental design

Standard III-nitride LED structures were grown by metalorganic chemical vapor deposition (MOCVD) on patterned sapphire substrates (PSS) [53]. Figure 2.2(a) shows the epitaxial structure and completed device fabrication. The growth consisted of a 1.4 µm unintentionally doped (UID) GaN template layer; 4 µm of Si-doped $n$-GaN; a 30-period Si-doped superlattice (SL) with 3 nm $In_{0.03}Ga_{0.97}N$ and 3 nm GaN, which was then capped with 20 nm of UID GaN. The active region consisted of 6 multiple quantum wells (MQWs) with 2.4 nm InGaN wells and 22 nm GaN barriers with emission at 447 nm. The barriers were grown in two steps in order to smooth out the morphology. 3 nm of GaN were grown at the same temperature as the InGaN wells followed by 19 nm grown at a temperature 50°C hotter than that of the InGaN. This increase in temperature increased the Ga adatom mobility so that any V-defects that originated from the InGaN wells were closed. After the high temperature GaN barrier was grown, the temperature was ramped back down 50°C to grow the low temperature GaN barrier and InGaN well. Above the active region was a 26 nm Mg-doped AlGaN electron blocking layer (EBL); a 120 nm Mg-doped $p$-GaN layer; and a 17 nm Mg-doped $p^+$-GaN contact layer.

After MOCVD growth, µLED structures of six varying areas were processed. Table 2.1 lists the device geometries of the devices that ranged from $10 \times 10$ µm$^2$ ($10^{-4}$ mm$^2$ in area) to $100 \times 100$ µm$^2$ (0.01 mm$^2$), and Figure 2.2(a) shows the structures. First, 100 nm

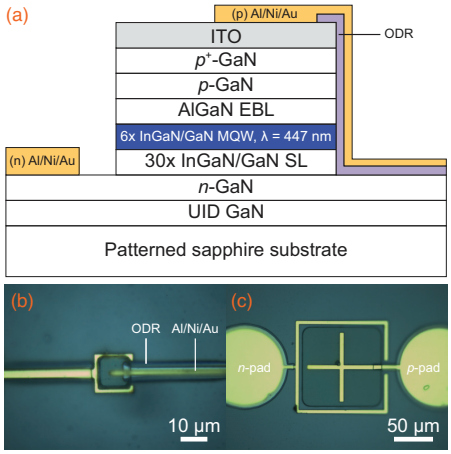


Figure 2.2: (a) Cross-sectional schematic of the epitaxially grown layers and processed devices. (b) Top-down optical micrograph of the processed device geometry for the $10\times10$ $\mu m^2$ device and (c) $100 \times 100$ $\mu m^2$ device. Figure from Hwang *et al.* [53]

Table 2.1: μLED Geometries

| μLED dimensions ($\mu m^2$) | Perimeter ($\mu m$) | Mesa area ($\mu m^2$) | Perimeter/area ($\mu m^{-1}$) |
|---|---|---|---|
| $10 \times 10$ | 40 | 100 | 0.4 |
| $20 \times 20$ | 80 | 400 | 0.2 |
| $40 \times 40$ | 160 | 1,600 | 0.1 |
| $60 \times 60$ | 240 | 3,600 | $0.0\bar{6}$ |
| $80 \times 80$ | 320 | 6,400 | 0.5 |
| $100 \times 100$ | 400 | 10,000 | 0.04 |

indium tin oxide (ITO) was deposited using electron beam (e-beam) evaporation to form a transparent p-contact. Square mesas were defined by using a reactive ion etch (RIE) to etch down through the ITO (using methane, hydrogen, and argon chemistry) to the *n*-GaN (using $SiCl_4$ at a bias of 200 W). An omnidirectional reflector (ODR) with 95.5% reflectance at 450 nm was deposited via ion beam deposition. The ODR consisted of alternating layers of silicon dioxide ($SiO_2$) and tantalum pentoxide ($Ta_2O_5$) with a final layer of aluminum oxide ($Al_2O_3$). Specifically, the seven layer dielectric was composed of 304.1 nm $SiO_2$, 121.4 nm $Ta_2O_5$, 355.7 nm $SiO_2$, 59.0 nm $Ta_2O_5$, 89.8 nm $SiO_2$, 53.5 nm

$Ta_2O_5$, and 59.5 nm $Al_2O_3$. Common $n$- and $p$-metal contacts and wire-bonding pads of 700/100/1000 nm Al/Ni/Au were deposited by e-beam evaporation. To keep the light-emitting area proportional between the different-sized µLEDs, the metal covered 10% of the mesa area in all cases. As shown in Figures 2.2(b)-(c), the ODR was deposited on the $n$-GaN to serve as a reflective layer underneath the contact pads and also came up over the sides of the mesa to prevent an electrical short between the $p$-contact metal and the $n$-GaN. The µLEDs were singulated into $0.7 \times 0.7$ mm$^2$ die and packaged by dicing, mounting onto silver headers, wire bonding, and encapsulating in transparent silicone with a refractive index of 1.41. The µLEDs were tested under continuous wave conditions in a calibrated integrating sphere.

### 2.2.2 Forward voltage of µLEDs

The dependence of forward voltage on drive current is plotted in Figure 2.3. Figure 2.3(a) shows that the forward voltage increased with device size. This increase can be explained by the larger areas of the µLEDs. The most resistive components of the devices were the ITO and p-GaN, and their areas were equal to the mesa size. With more area and volume of these layers, the spreading resistance increased. Consequently, Figure 2.3(b) shows that smaller µLEDs could be operated at higher current densities at a given voltage.

### 2.2.3 Optical results of µLEDs

Figure 2.4 shows EQE curves for each of the six µLEDs. The three largest µLEDs followed approximately the same trends, as did the three smallest µLEDs. The larger devices had higher EQEs than the smaller µLEDs but also had larger droop. These results can be understood by looking at the various contributors to the EQE, such as the IQE and

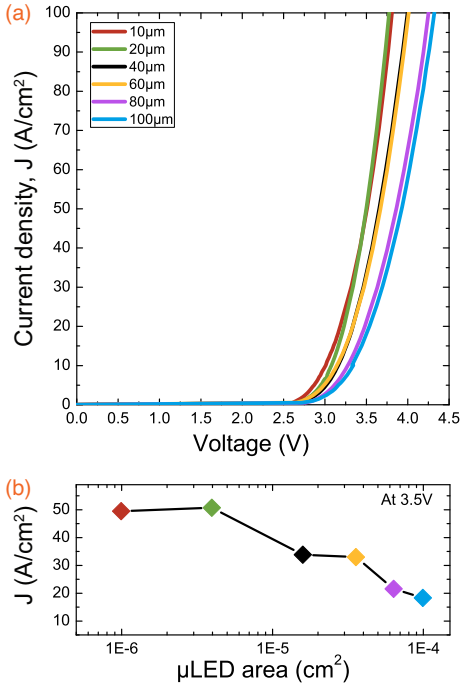


Figure 2.3: (a) Dependence of voltage on current density for the six different μLEDs (legend describes the mesa edge length). (b) Current density of the μLEDs at 3.5 V. The colors of the symbols correspond to the legend in (a). Figure from Hwang *et al.* [53].

extraction efficiency.

The structures were designed so that the metal coverage of the mesa was 10% in all sizes. This coverage ensured the light extraction efficiencies were similar so that the trends in EQE would be the same for IQE. IQE may be described with the ABC model:

$$\eta_{internal}, \text{IQE} = \frac{Bn^2}{An + Bn^2 + Cn^3} \tag{2.1}$$

The $A$ coefficient describes nonradiative recombination (e.g. Shockley-Read Hall recombination), the $B$ coefficient describes bimolecular radiative recombination, the $C$ coefficient describes Auger recombination, and $n$ is the carrier density.

Figure 2.5 conveys the effects of size on IQE. The peak EQEs shown in Figure 2.5(a)

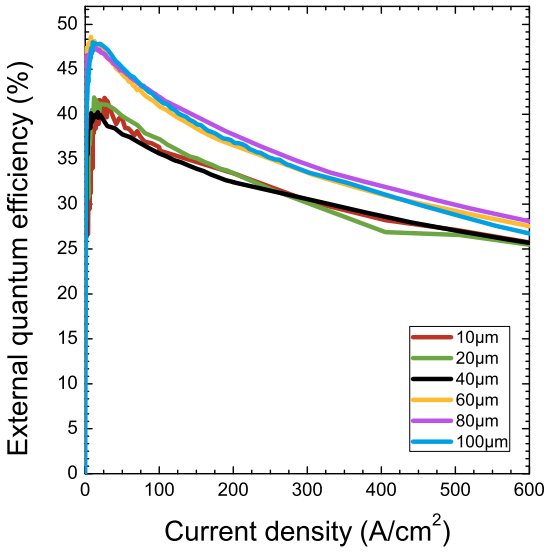


Figure 2.4: Dependence of EQE on current injection (legend describes the mesa edge length). Figure from Hwang *et al.* [53].

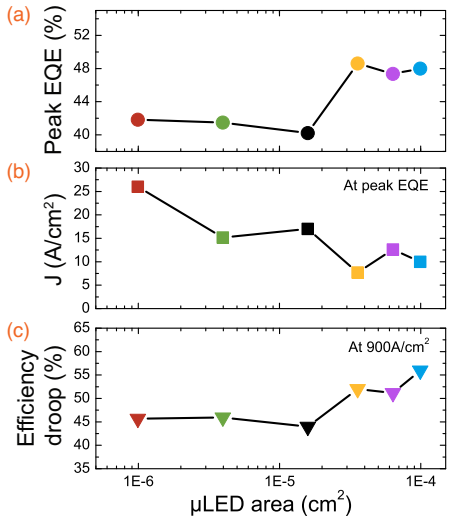


Figure 2.5: (a) Peak EQE, (b) current density at the peak EQE, and (c) efficiency droop at 900 A/cm$^2$ of the μLEDs. The colors of the symbols correspond to the legend in Figure 2.4. Figure from Hwang *et al.* [53].

were similar, ranging from 40.2% to 48.6%. The lower peak EQEs of the smaller µLEDs were a result of lowered IQE, which can be attributed to sidewall damage from dry etching. As shown in Table 2.1, the perimeter to area ratio was much larger for the smaller geometries. More exposed perimeter led to more sidewall damage, which caused more non-radiative recombination. In local areas around the perimeter, the effective $A$ coefficient may have increased (a more detailed description will be discussed in Chapter 2.3). With increased nonradiative recombination, the peak EQE was shifted to higher current densities, and Figure 2.5(b) demonstrates this effect. The current densities for the smallest and largest µLEDs at the peak EQE were 26 and 10 A/cm$^2$, respectively. Part of this nonradiative recombination may have been due to surface recombination. The surface recombination velocity of InGaN is on the order of $10^4$ cm/s compared with $10^5$ cm/s for AlGaInP [54]. Furthermore, the minority carrier diffusion length for InGaN is on the scale of hundreds of nanometers, whereas that of AlInGaP is micrometers. Because of these materials properties, ultra-small AlInGaP µLEDs may experience significant drops in EQE as the size diminishes, whereas InGaN µLEDs do not. Figure 2.5(c) shows the smaller µLEDs have lower efficiency droop. The droop at 900 A/cm$^2$ from the peak EQE for the smallest and largest µLEDs were 45.7% and 56.0%, respectively. This phenomenon can be explained by more uniform current spreading in the smaller devices since there was less area over which to spread the current. More uniform current spreading allows for more uniform light emission across the entire mesa. However, when current crowding occurs, some areas of the mesa will appear dim and light is not emitted in equal intensity. Therefore, the current density was higher in some areas and lower in others, leading to inhomogeneous light emission. This issue was exacerbated with increased current, so the efficiency drooped even more at high current densities.

The current spreading of the different µLEDs is illustrated in optical micrographs of µLED electroluminescence (EL) in Figure 2.6. Each row of images represents one

µLED size, and the resulting emission pattern is shown when current densities of 0.1 (left image), 1 (middle), and 10 A/cm$^2$ (right) were injected into the µLED. For the larger sizes, the current crowded around the edges of the mesa, so that the areas near the metal cross were dim. At small current densities of 0.1 A/cm$^2$, the effect was pronounced for the 100 × 100 µm$^2$ device. For µLEDs with edges of 40 µm and smaller, the current was able to effectively spread and produce photons across the entire mesa.

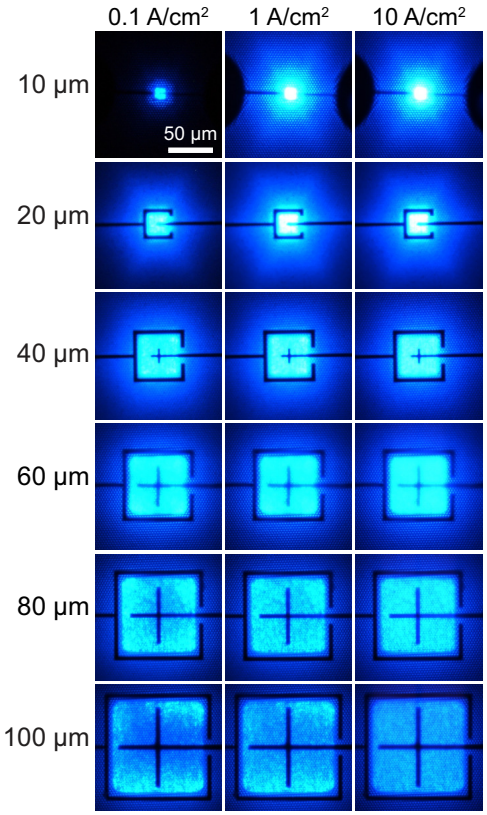


Figure 2.6: Optical micrographs of the µLED emission patterns at 0.1 (left), 1 (middle), and 10 A/cm$^2$ (right). The scale bar indicates 50 µm and is the same for all images. Figure from Hwang *et al.* [53].

To evaluate the light extraction efficiency contribution to EQE, Monte Carlo ray tracing was done in Synopsys LightTools using the materials properties in Table 2.2. The results confirmed there was at most a difference of 1.7 percentage points in extraction efficiencies (86.4% to 88.1%) between the sizes. As expected, the loss in layers such as

ITO, $p$-GaN, and $n$-GaN increased as the areas (and thus, the volume) of the devices increased due to their large coefficients of absorption. Smaller µLEDs should have more sidewall extraction than larger µLEDs because of the higher perimeter to area ratio. However, in this device scheme, the $n$-contact surrounded the mesa (see Figures 2.2(b)-(c)), which may then absorb the light emitted from the sidewalls so the increase in sidewall extraction was not large. Therefore, the light extraction efficiencies of all the devices were within 2 percentage points as shown in Table 2.3. Because the µLEDs were processed from the same epitaxial wafer, these results further support that the reduction in peak EQE with smaller sizes is not due to light extraction but likely from sidewall dry etching damage.

Table 2.2: Materials Properties

| Material | Refractive Index, $n$ | Absorption Coefficient, $\alpha$ ($cm^{-1}$) |
|---|---|---|
| ITO | 2 | 1000 |
| $n$-GaN | 2.5 | 7 |
| $p$-GaN | 2.5 | 100 |
| Al | 0.48 | $1.33 \times 10^6$ |
| Ni | 1.62 | $7.50 \times 10^5$ |
| Au | 1.47 | $5.18 \times 10^5$ |

Table 2.3: Extraction Efficiencies

| LED Edge Length (µm) | Extraction Efficiencies (%) |
|---|---|
| 10 | 86.4 |
| 20 | 87.8 |
| 40 | 88.1 |
| 60 | 87.7 |
| 80 | 87.2 |
| 100 | 86.9 |

### 2.2.4 Summary

In summary, we have shown that high EQEs may be maintained when decreasing the size of a InGaN/GaN µLED from 0.01 $mm^2$ to $10^{-4}$ $mm^2$. The peak EQEs of the largest and smallest µLEDs were 48.6% and 40.2%, respectively. The sidewall damage was more noticeable for the smaller µLEDs with larger perimeter to area ratios, as can be seen by the increased current density corresponding to the peak EQE (26 and 10 $A/cm^2$ for the largest and smallest µLED, respectively). While the larger µLEDs had higher EQEs, the current spreading for the smaller µLEDs was better, so the efficiency droop at 900 $A/cm^2$ was smaller for the smaller µLEDs. Ray tracing modeling revealed that the extraction efficiencies were similar for all the sizes, so the drop in EQE was due to sidewall damage. With these results, ultra-small µLEDs on the scale of $10 \times 10$ $\mu m^2$ may be used for high-resolution applications while achieving high efficiency.

## 2.3 ABC modeling

### 2.3.1 General description and mathematical formulation

The ABC model is described briefly in Section 2.2.3 by Equation 2.1 and illustrates how the IQE behaves with carrier density. The relationship between carrier density, $n$, and current density, $J$, is shown in Equation 2.2:

$$J = q \cdot w \cdot (An + Bn^2 + Cn^3), \tag{2.2}$$

where $q$ is the charge of an electron in Coulombs and $w$ is the total quantum wells' thickness. At low carrier densities, the $A$ coefficient dominates, and at high carrier densities, the $C$ coefficient dominates. For conventional large-area LEDs, peak EQEs

typically occur around 1-2 A/cm$^2$, which is in the low carrier density regime where SRH recombination dominates. The $B$ coefficient is assumed to be independent of current density and size, so a bulk value of $B$ is used for fitting differently sized µLEDs. A typical value for $B$ is $10^{-11}$ cm$^3$/s; $A$ and $C$ coefficients are on the order of $10^7 - 10^8$ s$^{-1}$ and $10^{-31}$ cm$^6$/s, respectively [55–57]. To extract $A$ and $C$ coefficients, experimental data may be fit with a polynomial. First, Equations 2.1 and 2.2 may be used to derive an expression for $n$:

$$\begin{aligned} Bn^2 &= IQE \cdot (AN + BN^2 + CN^3) \\ n &= \sqrt{\frac{IQE \cdot J}{q \cdot w \cdot B}} \end{aligned} \tag{2.3}$$

Taking the inverse of IQE then gives:

$$\begin{aligned} \frac{1}{\text{IQE}} &= \frac{An + Bn^2 + Cn^3}{Bn^2} \\ &= \frac{A}{B} \cdot \frac{1}{n} + \frac{C}{B} \cdot n + 1, \end{aligned} \tag{2.4}$$

which gives a relationship between the inverse of IQE and carrier density. Measured data relating current density and EQE may now be transformed to a relationship between $n$ and IQE (since EQE = IQE $\times\, \eta_{\text{extraction}}$), and $A$ and $C$ values may be fit to Equation 2.4.

### 2.3.2 Extraction of $A$ and $C$ coefficients

To extract the $A$ and $C$ coefficients of the µLEDs fabricated in Chapter 2.2, the EQE curves were first smoothed by a Gauss filter to remove noise. The fits were plotted over the original data points in Figure 2.7. Current density was converted to carrier density by Equation 2.3 and assuming a total quantum well thickness of $w = 15$ nm (each individual

quantum well was ∼2.4 nm, and there were six wells). IQE was obtained by multiplying EQE by extraction efficiency (see Table 2.3).

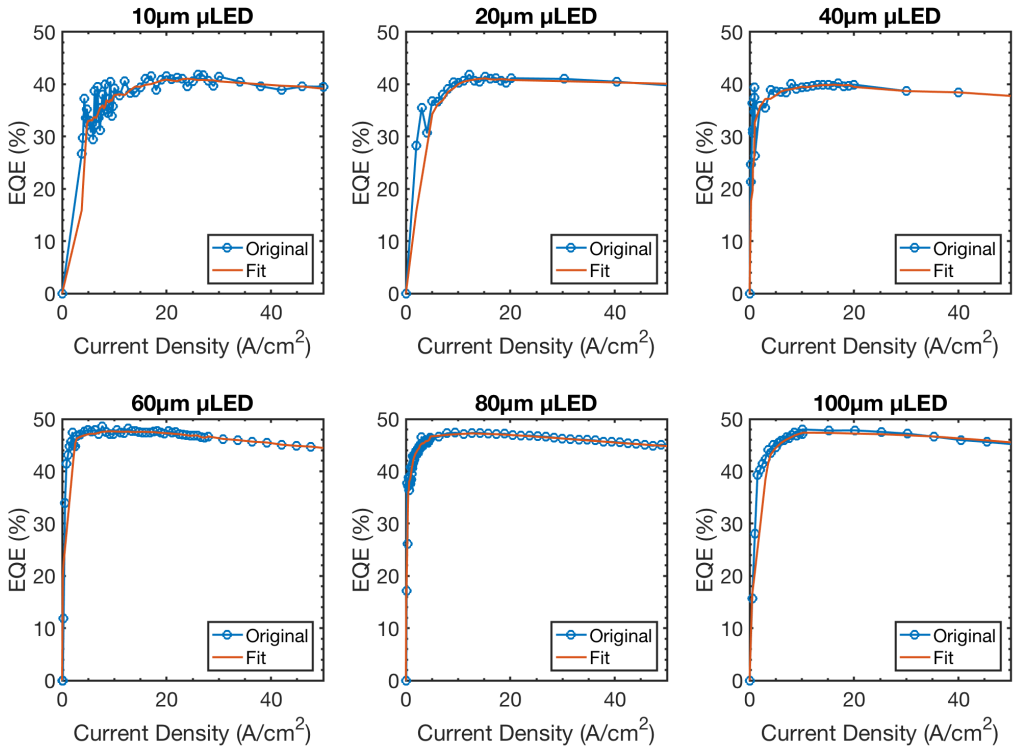


Figure 2.7: EQE curves smoothed by Gauss filter. The open blue circles are experimental data points, and the solid red lines are fits.

Figure 2.8 shows a plot of the inverse of IQE versus carrier density. Equation 2.4 was fit to the data by varying $A$ and $C$. At low carrier density, the first term, $\frac{A}{B} \cdot \frac{1}{n}$, dominated, and the behavior looked like $y = \frac{m}{x} + 1$, where $m$ was related to the $A$ coefficient. At high carrier density, the second term, $\frac{C}{B} \cdot n$, dominated, and the curve became linear with $y = n \cdot x + 1$, where $n$ was proportional to the $C$ coefficient. Using the extracted $A$ and $C$ coefficients from the fits in Figure 2.8, the expected IQE may be plotted using Equation 2.1. The resulting IQEs are shown in Figure 2.9 along with the experimental IQEs (experimentally measured EQEs divided by extraction efficiencies).

The fits generally followed the experimental data at high carrier densities ($> 5 \times 10^{19}$ cm$^{-3}$, above peak EQE). However, the fits strayed from the measured data points below $1 \times 10^{19}$ cm$^{-3}$. These disparities originated from the lack of clear data at low current densities (see Figure 2.7). The original data was noisy, and some of the behavior was lost in the smoothing process. The light output powers of the smaller µLEDs were typically in the range of microwatts, so obtaining more data points at low current densities requires more sensitive measurement systems. The measurements were taken in a large 500 mm diameter integrating sphere (Instrument Systems ISP 500). Lower light output values may be obtained by using a more sensitive photodetector and/or a smaller integrating sphere.

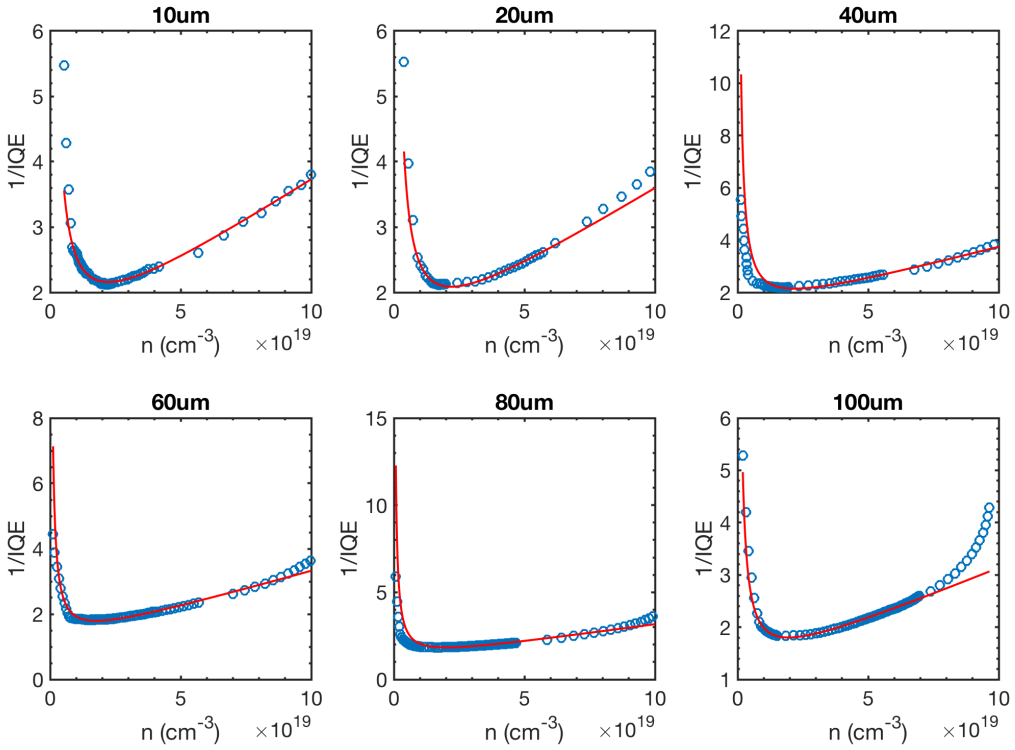


Figure 2.8: Carrier density vs 1/IQE. The open blue circles are experimental data points, and the solid red lines are fits from varying $A$ and $C$ coefficients (assuming a constant value of $B = 10^{-11}$ cm$^3$/s).

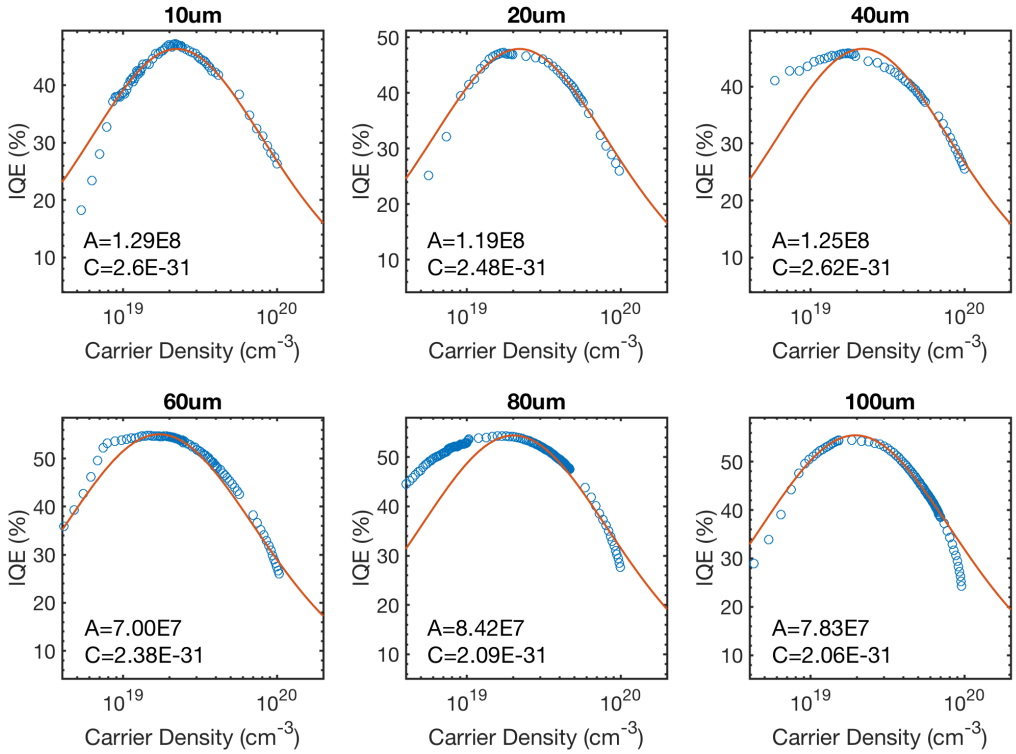


Figure 2.9: Carrier density vs IQE with fitted $A$ and $C$ coefficients. The open blue circles are experimental data points, and the solid red lines are expected IQEs from the ABC model.

The values for $A$ and $C$ coefficients are plotted for the different sizes of µLEDs in Figure 2.10, and the trends were consistent with work reported in the literature [57]. As the µLED size decreased (and the perimeter to area ratio increased), the A coefficient nearly doubled ($7.83 \times 10^7$ to $1.29 \times 10^8$ $s^{-1}$ for the $100 \times 100$ and $10 \times 10$ $\mu m^2$ devices, respectively) and indicated that the $A$ coefficient was dependent on the µLED size. The irregularity in the trend from the $40 \times 40$ and $60 \times 60$ $\mu m^2$ devices stemmed from the error of fitting 1/IQE versus carrier density. This analysis reemphasized the conclusion from Chapter 2.2: the sidewall is a significant area of concern for µLEDs. The dependence of SRH recombination (and surface recombination) hinges on µLED size, so special attention must be paid to those exposed surfaces. On the other hand, the $C$ coefficient exhibited a

lesser dependence of µLED size as it ranged only from $2.06 \times 10^{-31}$ to $2.60 \times 10^{-31}$ cm$^6$/s. One would expect a significant increase in $C$ coefficient as the µLED size increased to the size of conventional broad-area LEDs. With larger LEDs, current spreading becomes a more significant issue, so nonuniform current (or carrier) distributions will incite localized pockets of high current (carrier) density [52]. Consequently, $CN^3$ will dominate the nonradiative recombination as more Auger recombination occurs.

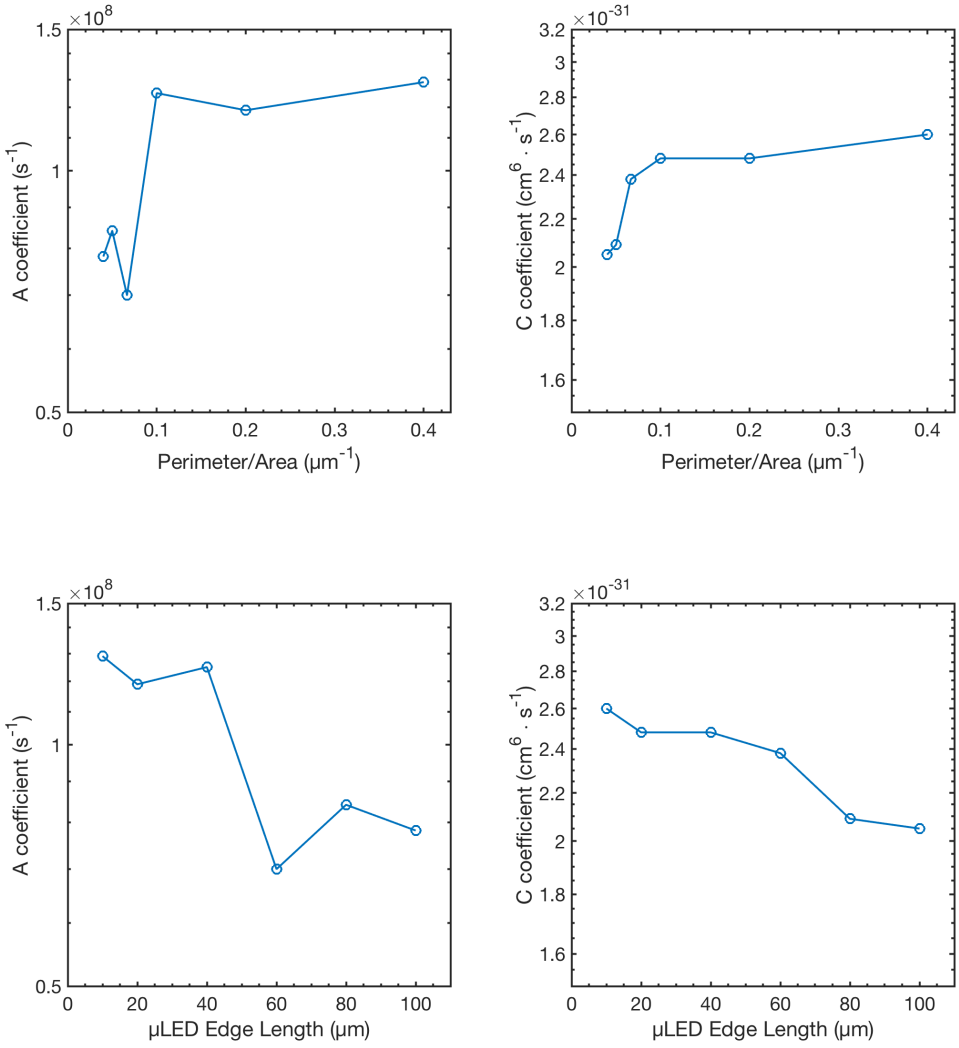


Figure 2.10: Extracted $A$ (a) and $C$ (b) coefficients for the different µLED sizes.

### 2.3.3 Limitations of ABC modeling

The ABC model is used to merge experimental and theoretical works, but may not be totally trustworthy as a predictive tool [55, 56]. There are many shortcomings and limitations of the ABC model that arise from assumptions. The model assumes uniform current and carrier distributions as well as independence of the $A$, $B$, and $C$ coefficients from carrier density (that $A$, $B$, and $C$ are constants). However, materials properties of III-nitrides and imperfections of III-nitride growth invalidate those assumptions.

Uniform current and carrier distributions are unlikely to occur in InGaN LEDs for various reasons. First, current crowding from lateral contact schemes, for example, would cause nonuniform injection. Furthermore, previous work in the literature has shown that current crowding depends on injection current densities [58, 59]. Secondly, carrier localization effects exist from the well-known phenomenon of compositional fluctuations of indium across the epitaxy. Thirdly, injection of quantum wells is likely inhomogeneous. It is widely postulated that holes only make it to the top quantum well (closest to the $p$-GaN), again causing nonuniform carrier distributions. Finally, the $A$, $B$, and $C$ coefficients likely depend on carrier density. In $c$-plane InGaN devices, spontaneous and piezoelectric field screening increases at high carrier density, which would change $A$, $B$, and $C$.

## 2.4 Sidewall passivation in µLEDs

As previously mentioned, the sidewall is a significant source of loss for µLEDs. Dangling bonds, vacancies/point defects, or damage from dry etches may lead to carrier leakage, which would reduce the number of carriers available for radiative recombination and total light output (a reduction of $B$ coefficient). To address this loss, sidewall passivation may

be done with dielectrics. In this section, the effects of dielectric deposition methods on the optical and electrical properties of µLEDs will be discussed [60].

### 2.4.1 Experimental design

The epitaxial structure and processing of µLEDs herein are the same as in Chapter 2.2. 50 nm of $SiO_2$ were deposited by atomic layer deposition (ALD) directly after the mesa etch and before the metal contact deposition. The dielectric was then etched in some areas to open a window of *p*-GaN for metal contacts. This etch was done either by dry etching with inductively coupled plasma (ICP) or wet HF etching. The labels, "ALD-ICP" and "ALD-HF," will be used to distinguish between those two processes. For comparison, µLEDs without sidewall passivation were co-processed and will be referred to as the "Reference" sample.

### 2.4.2 Optical effects of sidewall passivation

The optical effects of the sidewall passivation are shown in Figure 2.11. Electroluminescence (EL) images of the processed µLEDs illustrated the differences between each of the methods. For the µLEDs with ALD deposited $SiO_2$, the light emission across the surface was uniform (see the second and third columns of Figure 2.11(a)). By contrast, the reference µLEDs showed dimmer areas in the center of the mesas (first column). Furthermore, Figure 2.11(b) showed the light output power of the µLEDs with sidewall passivation was higher for the $20 \times 20$ µm$^2$ µLEDs than that of the µLEDs without passivation. This increase translated to higher EQE for the µLEDs with ALD deposited $SiO_2$. Figure 2.12 showed the EQEs for $20 \times 20$ and $100 \times 100$ µm$^2$ µLEDs. The sidewall passivation for larger µLEDs was not critical, as the peak EQEs for the $100 \times 100$ µm$^2$ µLEDs were similar for both the reference and ALD devices (41% for ALD-HF, 38%

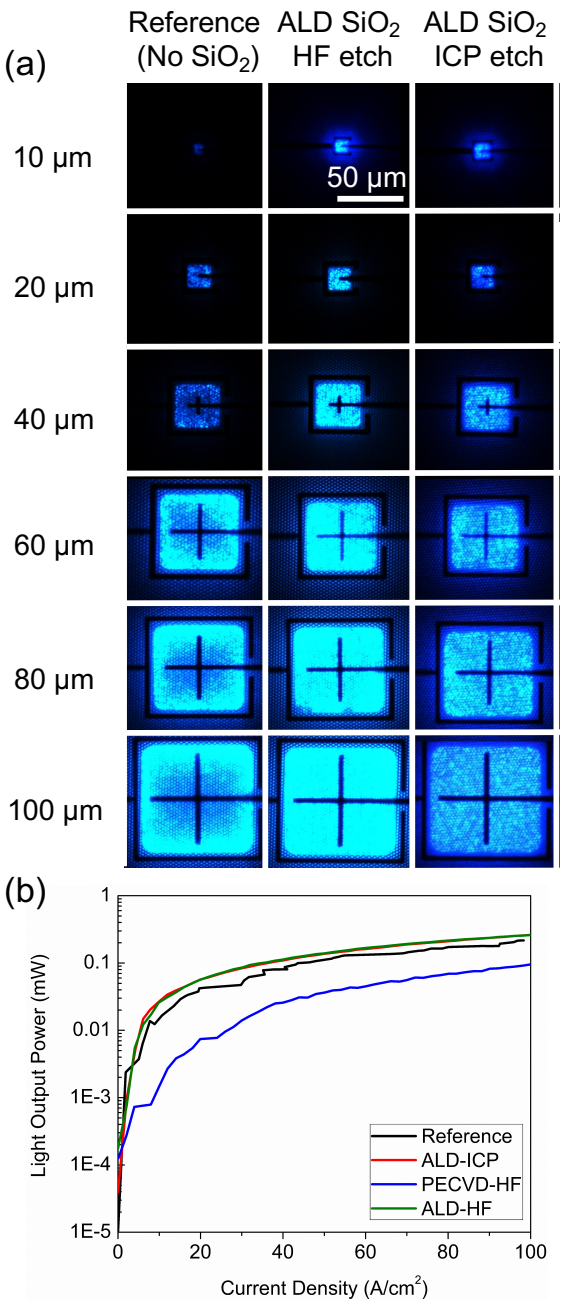


Figure 2.11: Influence of sidewall passivation on optical effects (a) Electroluminescence images of the µLEDs at 1 A/cm$^2$ and (b) light output power measurements for $20 \times 20$ µm$^2$ µLEDs. Figure from Wong *et al.* [60].

for ALD-PECVD, and 40% for Reference). However, the influence of passivation was enhanced for smaller µLEDs, since the peak EQEs for the ALD-HF and ALD-PECVD samples were ∼143% and ∼130% higher than that of the reference device. The loss of carriers to sidewall leakage (instead of radiatively recombining) was reduced with $SiO_2$ deposition, but the passivation did not completely solve the issue. Comparing the two differently sized devices showed that the peak EQE of the $20 \times 20$ µm$^2$ µLEDs was still ∼80% of that of the $100 \times 100$ µm$^2$ µLEDs. This efficiency loss indicated nonradiative recombination occurring at the sidewall was not completely resolved.

### 2.4.3 Electrical effects of sidewall passivation

Passivation also served to reduce sidewall leakage current. The leakage current induced by reverse bias at -4V (normalized by light emission area) is shown in Figure 2.13. Leakage current was suppressed with ALD deposition of $SiO_2$, but the amount of suppression varied with the deposition method. The ALD-HF devices showed a reduction in current of two orders of magnitude compared with the smaller reference devices, while the ALD-ICP devices had a reduction of only about half or one order of magnitude. The

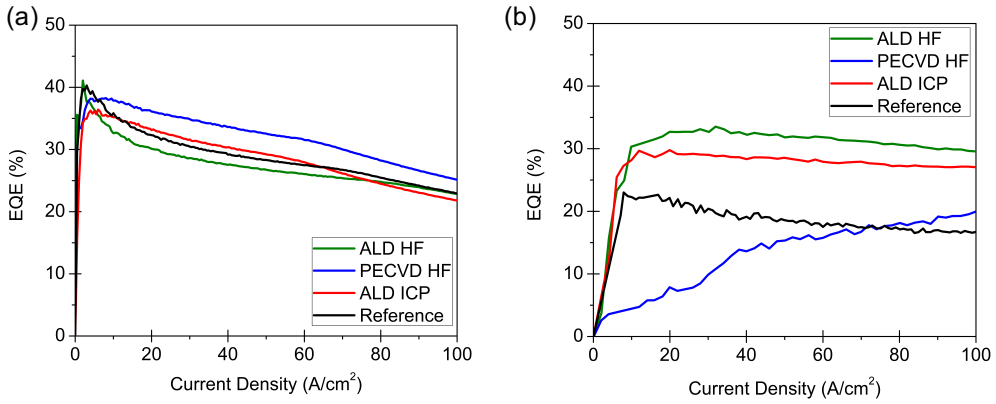


Figure 2.12: Dependence of EQE on current injection for (a) $100 \times 100$ µm$^2$ and (b) $20 \times 20$ µm$^2$ devices with different sidewall passivation methods. Figure from Wong *et al.* [60].

lessened effectiveness of the ALD-ICP passivation technique can be illustrated in the cross-sectional secondary electron microscope (SEM) image in Figure 2.14. The ITO on the µLEDs that had the $SiO_2$ etched by ICP also seemed to be roughened and etched. The exposed ITO (left side of image) was thinner than the covered ITO (right side) and may have reduced the current spreading. In contrast, the ITO on µLEDs was unaffected by the HF wet etch. Although the ALD-HF technique was more effective than the ALD-ICP technique, the trend of decreased leakage current with increasing µLED size showed the passivation still was not enough to completely recover the sidewall damage.

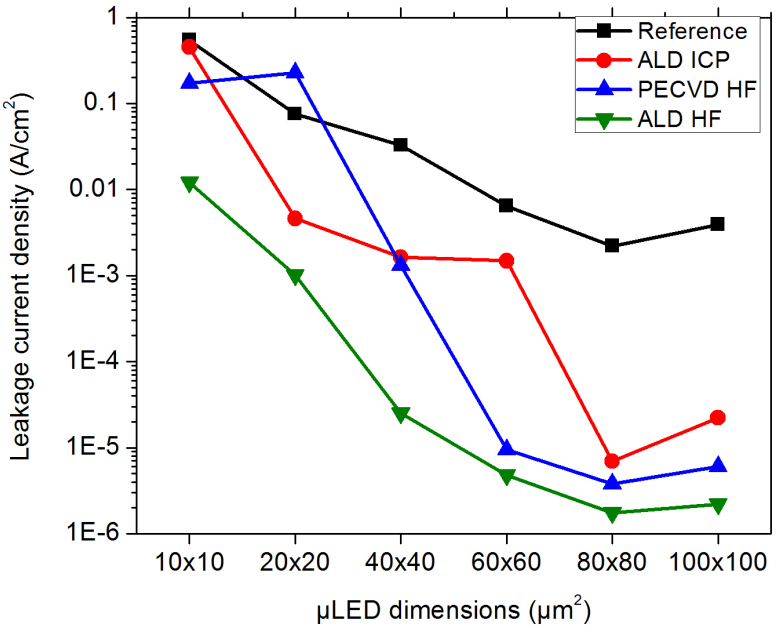


Figure 2.13: Dependence of leakage current at -4 V on the dimensions of µLEDs with different sidewall passivation methods. Figure from Wong *et al.* [60].

### 2.4.4 Summary

To summarize, the optical and electrical performance of µLEDs may be improved with sidewall passivation using ALD to deposit $SiO_2$. Optically, the light emission pattern

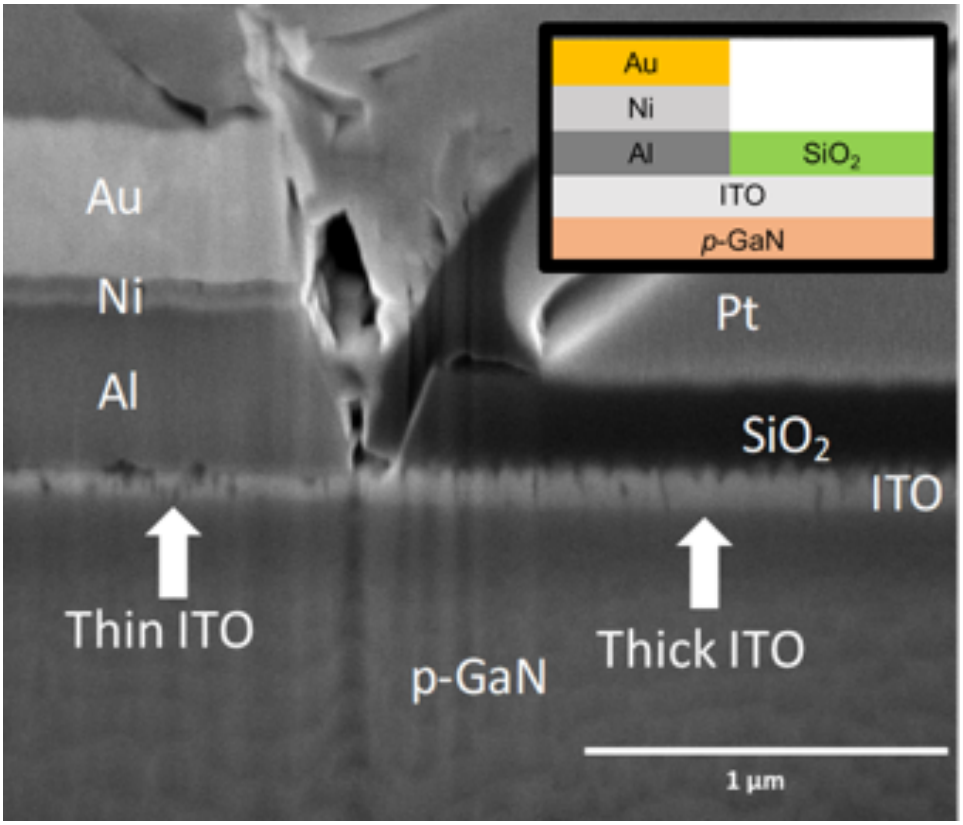


Figure 2.14: Cross sectional scanning electron microscopy image of ITO layer after exposing to ICP etch. The left side was exposed to ICP etch to remove $SiO_2$ and the right side was covered by photoresist during the etch. Figure from Wong *et al.* [60].

across the mesa became more uniform, and the EQEs of smaller µLEDs (below $20 \times 20$ $\mu m^2$) were enhanced compared with those without sidewall passivation (33% and 24% for the ALD-HF and reference samples, respectively). Electrically, the sidewall passivation also reduced the amount of leakage current under reverse bias. The use of HF instead of ICP to etch the $SiO_2$ prevented unintentional etching of exposed ITO and gave the lowest leakage current of all other techniques.

## 2.5 Future directions to improve µLED efficiencies

µLEDs are poised to enter the display market but still require improvements in efficiency, and a deeper understanding of the loss mechanisms is needed. As shown in Chapters 2.2−2.3, the ABC model has limitations in understanding $A$,$B$, and $C$ coefficients and may not be an accurate enough model. The loss of carriers to surface recombination is detrimental to smaller µLEDs, and the extraction of $A$ and $C$ coefficients has limited meaning. A more direct measurement of carrier energy would highlight the transport of carriers in the µLED structure. Recent work at UCSB has focused on the direct observation of Auger-generated hot electrons emitted into vacuum [56,61]. These electroemission studies measure the electron energy, and the energy electron distribution curves (EDCs) can provide some evidence as to where leakage might be occurring. To collect the electrons, the $p$-GaN surface is covered with cesium so there is a negative electron affinity and the conduction band minimum lies above the vacuum level. The electron energies may be accounted for by various processes: high energy electrons created by Auger recombination in the QWs that populate different valleys of the conduction band; carriers that overshoot or overflow the QWs; or low energy electrons from photoemission that were reabsorbed near the surface.

Specialized structures are necessary in order to fit the samples into the measurement

setup and conduct these measurements. $1 \times 1$ cm$^2$ pieces are fabricated with µLEDs in the center as shown in Figure 2.15. To collect electrons, the top or emitting surface of the µLEDs must be $p$-GaN. All other areas must be covered with metal contacts or $SiO_2$ in order to preserve uniform electric fields or to block electron emission in the field. This measurement system may then be done with various sized µLEDs to see how the EDCs change with size. In addition, the effects of dry etches and sidewall treatments may also be measured.

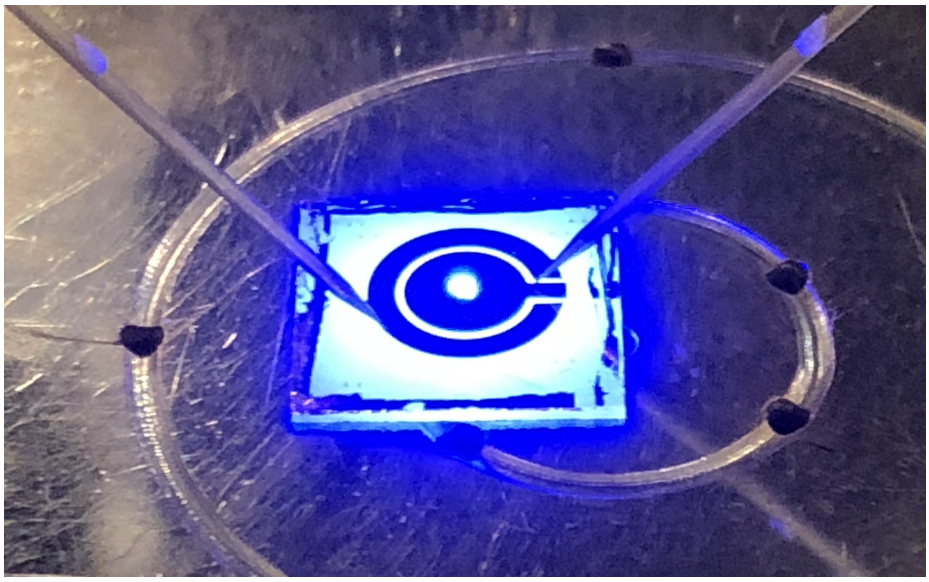

Figure 2.15: Optical photograph of specialized device to emit electrons out of a top $p$-GaN surface for measurement in a customized tool for electroemission spectroscopy.

Various dry etches and sidewall treatments have also been discussed. The µLEDs reported in this chapter had mesas etched with 200W of power in RIE. Lower power damages may be investigated, which would lower the etch rate. Post-etch recovery has been tried using various annealing studies as well [62–64]. Other passivation techniques involve wet etching with KOH or encapsulation with dielectric [65, 66]. Another direction is the passivation of the sidewall. While $SiO_2$ and $SiN_x$ are commonly used, other materials such as AlN, $Al_2O_3$, $Ga_2O_3$ may be used since these materials are native to the

III-nitride family.

Finally, since the sidewall is a source of problems, designs that move the sidewall of the active region far away from any etch damage may minimize any losses. Ideally, a wet etch would remove etch damage from plasma-based dry etches, but wet etching of GaN is extremely difficult (see Chapter 5 for more details). Nevertheless, creating a current aperture is an important direction to consider. Rather than recovering sidewall damage, these quasi-mesaless designs would remove damage at the most important interface of the µLED. To create this current aperture, the $p^+$-GaN outside the light-emitting area would need to be rendered resistive. Options to insulate this layer include damaging $p$-GaN with plasma, ion implanting with Al or other species, or oxidizing the $p$-GaN to create resistive $Ga_2O_3$. This current aperture method will be covered in more detail in Chapter 4.

# Chapter 3

# μLEDs with Tunnel Junction Contacts Grown by MOCVD

## 3.1 Background on III-nitride tunnel junctions

In standard III-nitride LED devices, the lossiest parts are typically on the *p*-side, and the losses arise from poor conductivity and optical absorption loss. *p*-GaN is highly resisitve, and ohmic contacts are difficult to achieve even with degenerate doping of GaN (typically with Mg). Metal stacks of palladium or nickel are typically used, and specific contact resistances on the order of $10^{-5}$ to $10^{-4}$ $\Omega \cdot \mathrm{cm}^2$ may be achieved [67–69]. However, these metals are opaque and have low reflectances. Thus, transparent conducting oxides (TCOs) such as indium tin oxide (ITO) or zinc oxide (ZnO; less commonly used than ITO) are required to spread the current across the entire surface of the LED [70]. However, these layers still yield electrical and optical losses. To reduce those losses, a tunnel junction contact may be used on the *p*-side.

The general working principle of a tunnel junction contact is shown by the band

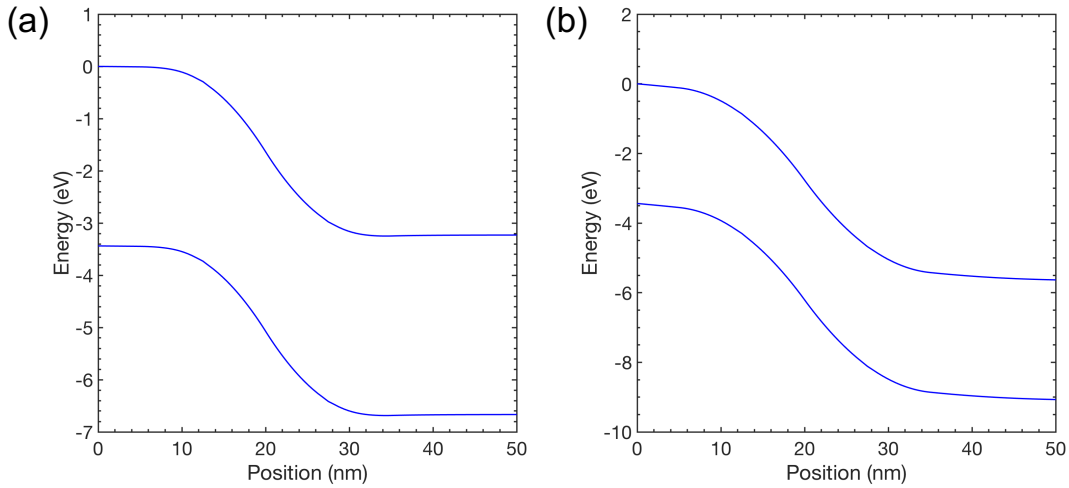


Figure 3.1: Electrical band diagram of a tunnel junction contact to $p$-GaN operated (a) at zero bias and (b) in reverse bias (-3V). When operated in reverse bias, the tunnel junction contact injects holes into $p$-GaN.

diagram in Figure 3.1. The tunnel junction exists at the interface between $n$-GaN and $p$-GaN. At zero bias (Figure 3.1(a)), the depletion width is rather high, but in reverse bias (Figure 3.1(b)), the depletion width decreases, which increases the tunneling probability. Thus, electrons from the valence band maximum of the $p$-GaN tunnel to the conduction band minimum of the $n$-GaN, which is effectively an injection of holes. In order for this tunnel junction contact to be effective in a III-nitride LED, there should be highly doped $p^{++}$- and $n^{++}$-GaN layers in order to get a small depletion width. The dependence of the zero bias depletion width on carrier levels is shown below in Equation 3.1,

$$W = \sqrt{\frac{2 \cdot \epsilon \cdot E_g}{q} \left( \frac{1}{N_A} + \frac{1}{N_D} \right)} \tag{3.1}$$

where $\epsilon$ is the permittivity ($\epsilon = \epsilon_0 \cdot \epsilon_r$; $\epsilon_0$ is the permittivity of free space and $\epsilon_r$ for GaN is 8.9), $E_g$ is the band gap, $q$ is the charge of an electron, $N_A$ is the acceptor concentration, and $N_D$ is the donor concentration. One of the major challenges in the GaN

material system is low $p$-doping and low hole concentrations. Although the magnesium concentration may be doped in the $10^{20}$ to $10^{21}$ cm$^{-3}$ levels, the ionized acceptor levels are typically only a few percent so that $N_A$ is in the $10^{18}$ to $10^{19}$ cm$^{-3}$ range. The typical ionization energy of Mg in GaN is around 250 meV [71, 72]. Considering the fact that the room temperature energy, kT (product of Boltzmann constant and temperature), is approximately 25.8 meV, this Mg ionization energy is quite high. On the other hand, a typical donor dopant in GaN is Si. The typical ionization energy of Si in GaN is between 17 to 23 meV [73,74], and these dopants are almost completely ionized. Figure 3.2 shows the change in depletion widths for varying carrier levels (note: the absolute widths shown are only the ideal case; experimentally, the depletion widths are likely larger). Even at carrier concentrations of $10^{19}$ cm$^{-3}$, the zero bias depletion width is $\sim$ 26 nm.

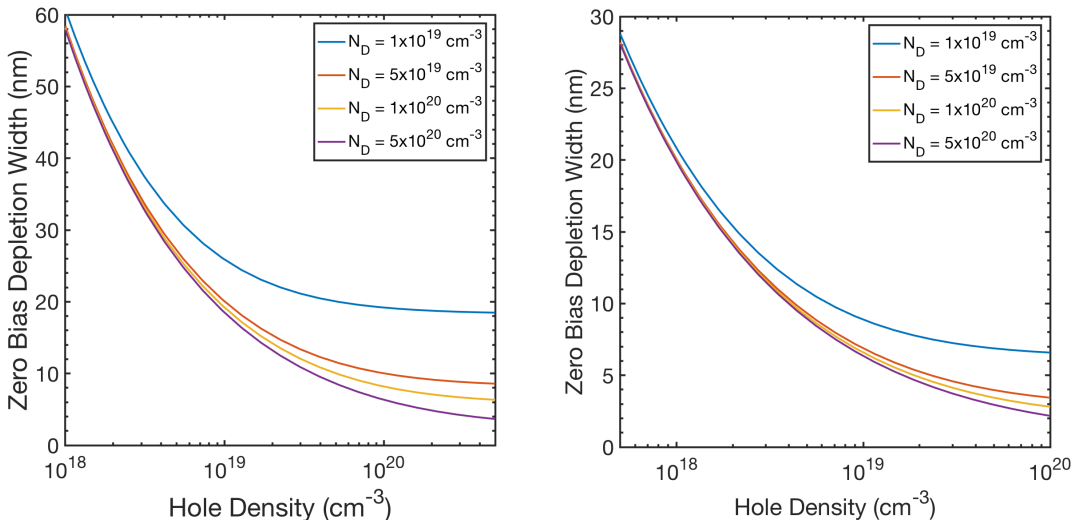


Figure 3.2: Change of depletion width with carrier concentrations at (a) zero bias and (b) reverse bias (-3V).

### 3.1.1 Issues with MOCVD grown tunnel junctions

Despite the large depletion widths (which Simon *et al.* predicted to be too large for substantial tunneling current [75]), III-nitride TJ contacts have been grown by MOCVD since 2001 [75–78]. The main issues have been that the voltage penalty (difference in voltage when using a tunnel junction contact versus a standard $p$-contact to GaN, e.g. ITO, Pd/Au, etc) has been between 1.0 to 3.2V and that the light output power has been very low (early works only reported light output powers in arbitrary units and without any quantum efficiency values). The high voltage penalty was likely due to re-passivation of the $p$-GaN during the tunnel junction growth. As-grown $p$-GaN is resistive because hydrogen from the reactor will form Mg-H complexes that passivate the acceptors. To activate the acceptors, the material must be annealed at 600°C for 15 minutes to drive out the hydrogen [79–81]. For LED structures with $p$-GaN at the surface, the hydrogen is driven out through the surface. However, when growing $n$-GaN on top of $p$-GaN to form a tunnel junction, this activation is prohibited since $n$-GaN is a diffusion barrier to hydrogen [82]. It appears that these early attempts at tunnel junctions suffered from high voltage because of this incomplete activation. Another issue is the magnesium memory effect [83]. Excess magnesium lingering in the reactor may diffuse into $n$-GaN layers and compensate for silicon, reducing the concentration of donors available. Various methods to address the Mg diffusion into $n$-GaN include doing a surface treatment [83], inserting an AlN layer to supress the diffusion of magnesium [84, 85], or using flow modulation epitaxy [86].

More recently, tunnel junction contacts to III-nitride LEDs have demonstrated improved operating voltages by activating via lateral diffusion of hydrogen [87,88]. However, for large area LEDs, lateral diffusion was not the complete solution as areas near the center of the LEDs were still dark (see Figure 3.3). The lower left image was of a reference

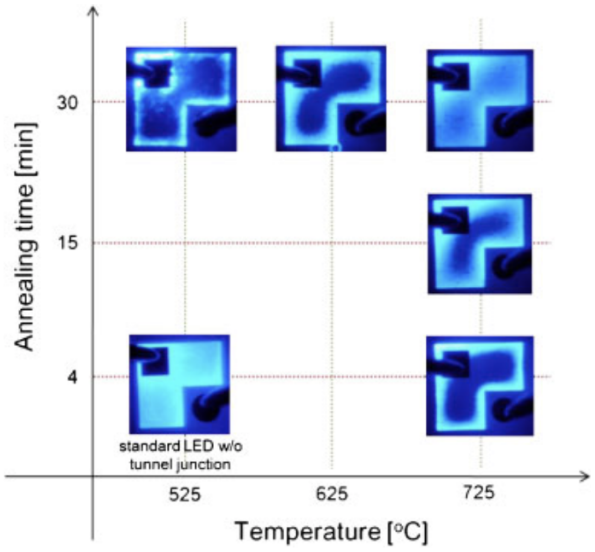


Figure 3.3: Emission regions of the LEDs with the tunnel junctions activated under various thermal annealing conditions and of the standard LED. Copyright 2013 The Japan Society of Applied Physics [87].

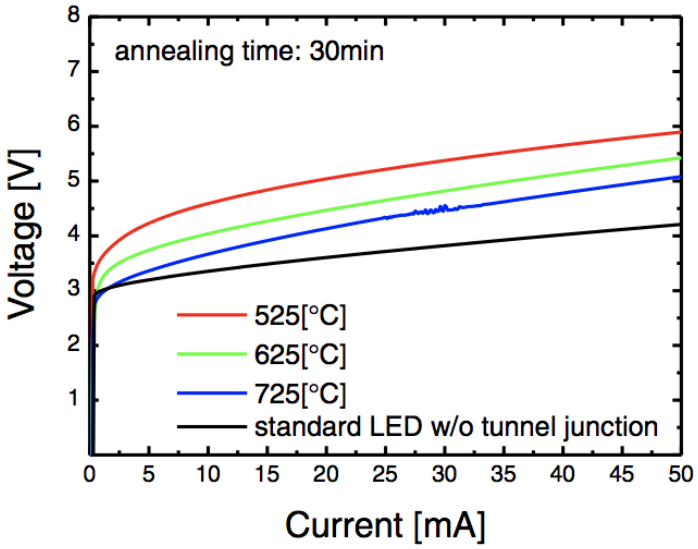


Figure 3.4: Current-voltage characteristics of the LEDs with the tunnel junction annealed under various temperatures for 30 min and for the standard LED. Copyright 2013 The Japan Society of Applied Physics [87].

LED without a tunnel junction, and light was emitted across the surface. The other images were of LEDs with tunnel junction contacts, and a large proportion of the mesa was still dark. Consequently, the voltage was significantly worse, as shown in Figure 3.4. Some groups have also done bandgap engineering to take advantage of the large polarization in *c*-plane GaN. Inserting an InGaN layer [89–91] induced an electric field in the same direction of the built-in and applied fields, increasing the overall field and tunneling probability.

To prevent the re-passivation of *p*-GaN, LEDs with tunnel junctions have also been grown either entirely by molecular beam epitaxy (MBE) [92] or with a hybrid MBE-MOCVD method, where the LED was grown up to the *p*-GaN layer by MOCVD and the *n*-GaN tunnel junction contact was grown by MBE [93–96]. The advantage of using MBE to grow the *n*-GaN tunnel junction contact was that there was no hydrogen present in the chamber, so re-passivation of the *p*-GaN was avoided. These MBE-grown devices still faced issues with increased voltage from the tunnel junction, although Krishnamoorthy *et al.* demonstrated voltages for their tunnel junction LEDs that were comparable with their reference LEDs [93].

### 3.1.2 Motivation for µLEDs with tunnel junction contacts

The use of tunnel junction contacts in µLEDs allows for new design space when trying to build light sources for displays. First, terminating the epitaxial structure with *n*-GaN instead of *p*-GaN allows for the use of *n*-type metal contacts and mirrors. As referenced in Chapter 3.1, ohmic *p*-type metal contacts are limited. For µLEDs that emit out of one side, silver contacts must be used to maintain high reflectance. While LED and solid-state lighting companies have adopted Ag mirrors to create flip-chip LEDs, the creation of ohmic and long-lasting Ag contacts are quite problematic and difficult

because of issues with adhesion and thermal instability. Proper diffusion barriers must be incorporated so that any Ag intermixing with other metals is eliminated or else the reflectance will be drastically reduced. Various Ag-containing metal stacks also include islands (Å) of Ni, Pt, etc to form an ohmic contact to $p$-GaN [97–100]. Such stacks require a very precise deposition of the island contact, a subsequent anneal to form an ohmic contact, and deposition of a diffusion barrier to prevent outdiffusion of Ag. Various reasons for the anneal include the formation of NiO near the surface to create an ohmic contact; outdiffusion of Ga atoms from the $p$-GaN to the Ag layer to leave Ga vacancies (Ga vacancies are shallow acceptors, so the net hole concentration increases [101]). Furthermore, Ag migration is a significant issue that affects the lifetime of devices. By incorporating a tunnel junction contact, Ag is no longer needed as a mirror, since $n$-type metal contacts/mirrors may be used. For instance, Al has been shown by Yonkee *et al.* to reach peak EQE and wall-plug efficiency of 76% and 73%, respectively [95]. Al can reach a reflectance of 85% (or higher if combined with an omnidirectional mirror) and has low contact resistances in the $10^{-6}\ \Omega \cdot \mathrm{cm}^2$ range.

Another benefit of using tunnel junction contacts is that multiple active regions emitting at different wavelengths may be monolithically grown as shown in Figure 3.5. Kowsz *et al.* demonstrated monolithically integrated optically pumped yellow quantum wells on top of electrically injected blue wells on freestanding semipolar GaN [102]. In that case, polarized white light emission was measured by electrically contacting the blue wells to excite yellow emission from the above wells (polarized light is possible on semipolar orientations of GaN due to the separation of valence bands from light and heavy holes; $c$-plane has substantially less optical polarization because the valence bands are closer together). By tailoring the processing, both sets of quantum wells may be separately contacted electrically so there would be more precise control of the wavelength. This epitaxial structure has many major growth challenges to overcome though. In the case

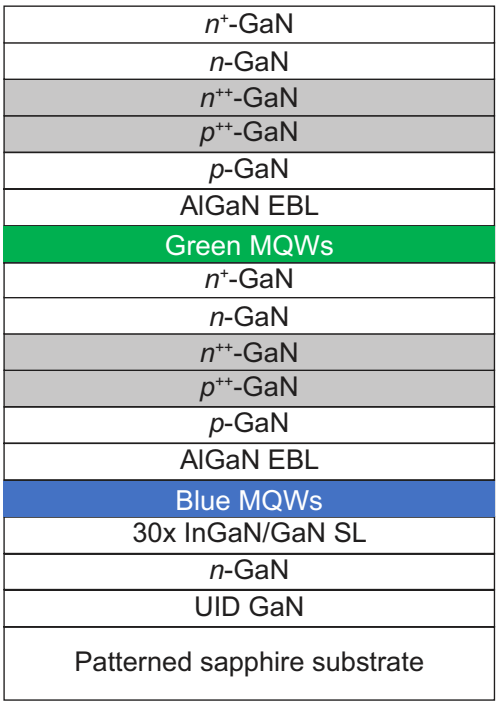


Figure 3.5: Cross-sectional schematic of an epitaxial structure with tunnel junction contacts enabling two active region InGaN growths (blue and green).

of µLED displays, the ideal structure would be to have all red, green, and blue quantum wells grown on the same wafer. As of now, this idea is still very much a research effort. The growth of high quality, efficient green wells is difficult because of the high indium content required. Although there has been much progress by Alhassan *et al.* at UC Santa Barbara [19, 103], the green gap still exists. Going to longer wavelengths beyond green is even more challenging, but the answer may lie in strain engineering (this topic is beyond the scope of this thesis). Despite these challenges, monolithically grown RGB LEDs may be advantageous to solving mass transfer issues.

## 3.2 Application of tunnel junctions to µLEDs

As discussed in Chapter 3.1.1, the lateral diffusion of hydrogen in a large-area LED is prohibitive to activating through the top surface. However, the smaller dimensions of µLEDs seem more suitable for this lateral diffusion. This section will detail the epitaxy, fabrication, and characterization of these tunnel junction µLEDs [104].

### 3.2.1 Design of MOCVD epitaxy

The epitaxial structure of the tunnel junction was split into two growths as shown in Figure 3.6. The first LED growth was the same as the LED structure grown in Chapter 2.2. After the $p^{++}$-GaN growth, the sample was removed from the MOCVD reactor. A first activation was done at 600°C in air for 15 minutes to activate the $p$-GaN through diffusion of hydrogen out of the top surface. Following this activation, a surface treatment was done to prepare for the tunnel junction regrowth. This treatment served to remove excess magnesium at the surface to minimize diffusion of Mg into the neighboring $n^{++}$-GaN, which would compensate the donors. The surface treatment consisted of immersion in ultraviolet-ozone (UVO) in a PR-100 UV-Ozone Photoreactor for 15 minutes followed by a one minute dip in buffered hydrofluoric acid (BHF). This treatment was done two more times for a total of three cycles. UVO treatment is commonly used to remove surface organics prior to regrowth, and the BHF improved the operating voltage of the µLEDs.

Following the treatment, samples were reloaded into the MOCVD reactor to grow the tunnel junction layers. The regrowth consisted of a 10 nm Si-doped $n^{++}$-GaN tunnel junction contact layer where the silicon concentration was varied, a 400 nm Si-doped $n$-GaN current spreading layer ([Si]= $2.0 \times 10^{19}$ cm$^{-3}$), and a 10 nm Si-doped $n^{+}$-GaN

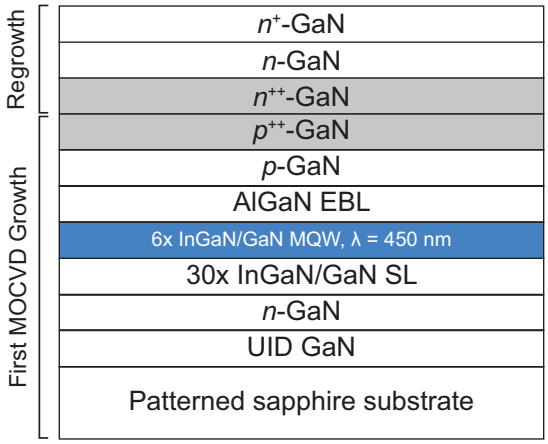


Figure 3.6: Cross-sectional schematic of the epitaxial structure showing the first LED growth and the tunnel junction contact regrowth.

contact layer ([Si]= $5.6 \times 10^{19}$ cm$^{-3}$). The Si source was disilane, and three different flow rates of the disilane (3 sccm, 6 sccm, and 10 sccm) were used to vary the silicon concentration of the n$^{++}$-GaN tunnel junction contact. The doping concentrations were measured by secondary ion mass spectroscopy (SIMS). Figure 3.7(a) shows the concentrations of silicon in the $n^{++}$-GaN tunnel junction layer were $7.0 \times 10^{19}$ cm$^{-3}$ (3 sccm disilane), $1.1 \times 10^{19}$ cm$^{-3}$ (6 sccm), and $1.7 \times 10^{20}$ cm$^{-3}$ (10 sccm). Figure 3.7(b) shows the effect of the surface treatment on the magnesium concentration. When the sample was taken out of the MOCVD reactor and treated with UVO and BHF, the surface concentration of the magnesium dropped by more than one half from $1.2 \times 10^{20}$ cm$^{-3}$ to $5.1 \times 10^{19}$ cm$^{-3}$.

### 3.2.2 Fabrication of tunnel junctions µLEDs

The fabrication of the tunnel junction µLEDs (referred to as "TJ µLEDs") closely followed that of the µLEDs in Chapter 2.2. µLEDs of varying areas (from $2.0 \times 10^{-5}$ to 0.01 mm$^2$) were fabricated into the geometry shown in Figure 3.8. For the TJ µLEDs, the processing was simplified because a transparent $p$-contact was no longer required.

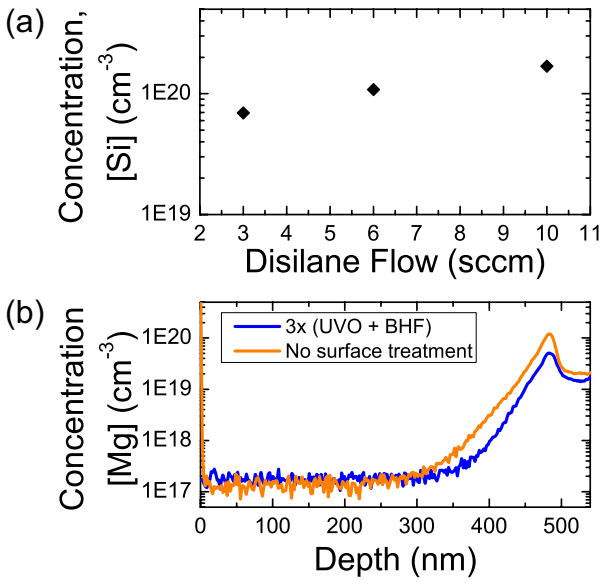


Figure 3.7: Doping concentrations of (a) Si as a function of disilane flow and (b) Mg with and without surface treatment. Figure from Hwang *et al.* [104].

First, square mesas were patterned by etching through to the bottom n-GaN layer using silicon tetrachloride in a reactive ion etch (RIE) chamber. To activate the *p*-GaN and drive out hydrogen, the µLEDs were annealed at 700°C for 30 minutes under 80%/20% $N_2/O_2$ (air) ambient. As discussed in Chapter 3.1.1, *n*-GaN is a barrier to hydrogen diffusion [82], so because the *p*-GaN was covered by the tunnel junction, the activation was done by lateral diffusion of hydrogen through the sidewalls of the mesas (see Figure 3.8(a)). An omnidirectional reflector (ODR) that consisted of alternating layers of silicon dioxide, tantalum pentoxide, and a capping layer of aluminum oxide was deposited by ion beam deposition. Common n-metal contacts and wire-bonding pads using 700/100/700 nm Al/Ni/Au were deposited by electron beam evaporation. The metal covered 10% of the mesa area in all sizes of µLEDs. The ODR was deposited both on the bottom *n*-GaN and the top (tunnel junction) *n*-GaN to isolate the *p*- and *n*-side. The ODR also served to reflect light that might be absorbed by the metal contacts. To compare the TJ µLEDs with standard µLEDs, a parallel process was done with indium tin oxide. This process

had the added steps of depositing 130 nm of ITO and etching the ITO before etching the $n$-GaN. TJ LED-1, -2, and -3 had silicon concentrations of $7.0 \times 10^{19}$ (3 sccm disilane), $1.1 \times 10^{20}$ (6 sccm), and $1.7 \times 10^{20}$ cm$^{-3}$ (10 sccm), respectively.

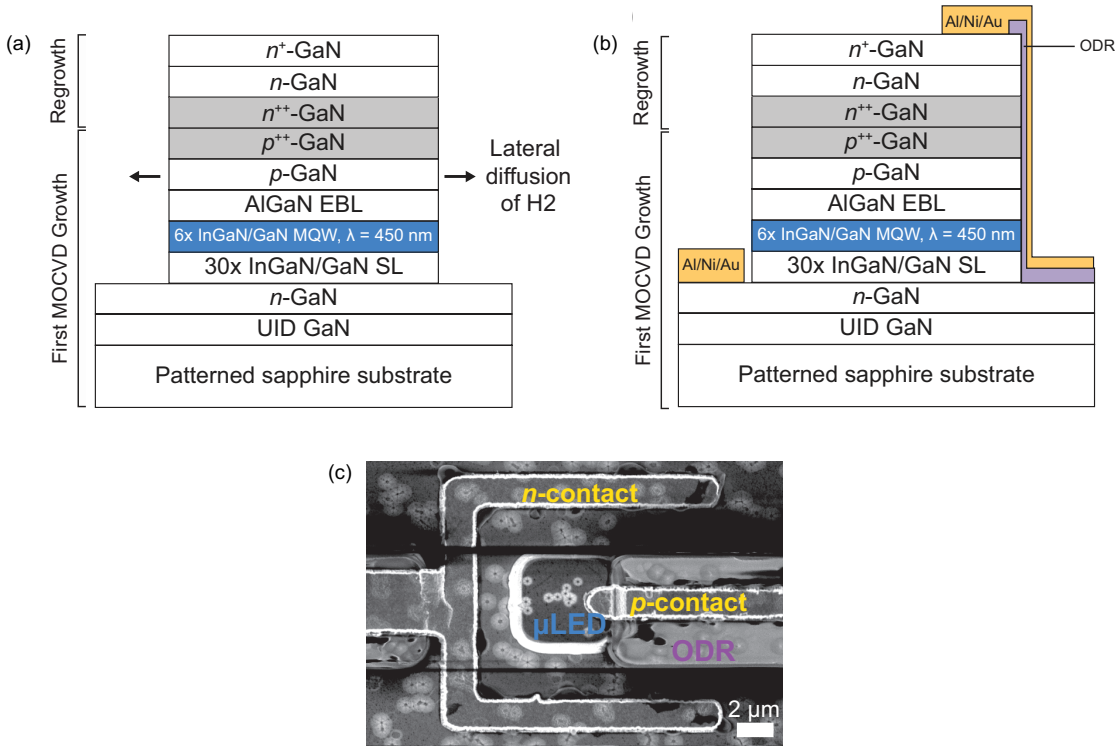


Figure 3.8: (a)-(b) Cross-sectional schematic of the processed LEDs. (c) Secondary electron microscope image of a $5 \times 5$ μm$^2$ μLED.

After fabrication, on-wafer testing was done to collect current density-voltage characteristics. Optical micrographs of the μLED electroluminescence were taken to look at current spreading and to see if the $p$-GaN was activated by lateral diffusion. The μLEDs were then singulated into $0.75 \times 0.75$ mm$^2$ die and packaged by mounting onto silver headers, wire bonding, and encapsulating in silicone (refractive index of 1.41). Testing was done under continuous wave conditions in a calibrated integrating sphere.

### 3.2.3 Electrical results

The electroluminescence emission of the µLEDs are shown in Figure 3.9. Comparing with the standard µLEDs and the work from Kuwano *et al.*, the TJ µLEDs in Figure 3.9 appeared to be activated across the mesa. There were no visible dark spots in the center of the mesa as there were in Figure 3.3. However, because of the much smaller dimensions of these µLEDs, the images may be misleading. The forward voltage characteristics in Figure 3.10 indicated there were areas that were not completely activated. Figure 3.10(a) plots the current density versus operating forward voltage of three different sized µLEDs ($5 \times 5$, $60 \times 60$, and $100 \times 100$ µm$^2$) for the standard µLEDs with ITO and the TJ µLEDs with the highest Si doping, TJ µLED-3. The turn-on voltages were the lowest for the standard µLEDs for all sizes. Furthermore, voltages of the standard µLEDs were similar for all the different sizes and were within 0.15 V. Figure 3.10(b) illustrates another way to analyze the forward voltage at 20 A/cm$^2$ for all samples and plots the average voltage at 20 A/cm$^2$ (with error bars shown; values were averaged over three to four data points). The curves showed the turn-on voltages of all three TJ µLEDs increased with µLED size and were higher than the standard µLEDs. The operating voltage also decreased substantially with increased Si doping, which will be discussed next.

The increase in voltage with µLED area for the TJ µLEDs can be explained by analyzing four sources of resistance within the µLED (see Figure 3.11): (1) contact resistance from Al/Ni/Au to the $n^{++}/n/n^{+}$-GaN layers; (2) the spreading resistance in the $n$-GaN current spreading layer; (3) the barrier at the tunnel junction interface between $n^{++}/p^{++}$-GaN; and (4) the resistance within the $p$-GaN layer. Between the three TJ LEDs, the nominal doping of the top $n^{+}$-GaN contact layer and the $n$-GaN spreading layer was the same, while the doping of the $n^{+}$-GaN tunnel junction contact layer was varied. Based on circular transmission line model (CTLM) measurements, average specific contact re-

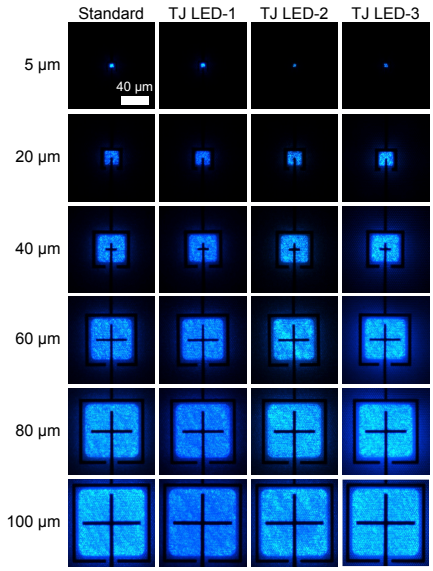


Figure 3.9: Electroluminescence images of µLEDs at 1 A/cm$^2$.

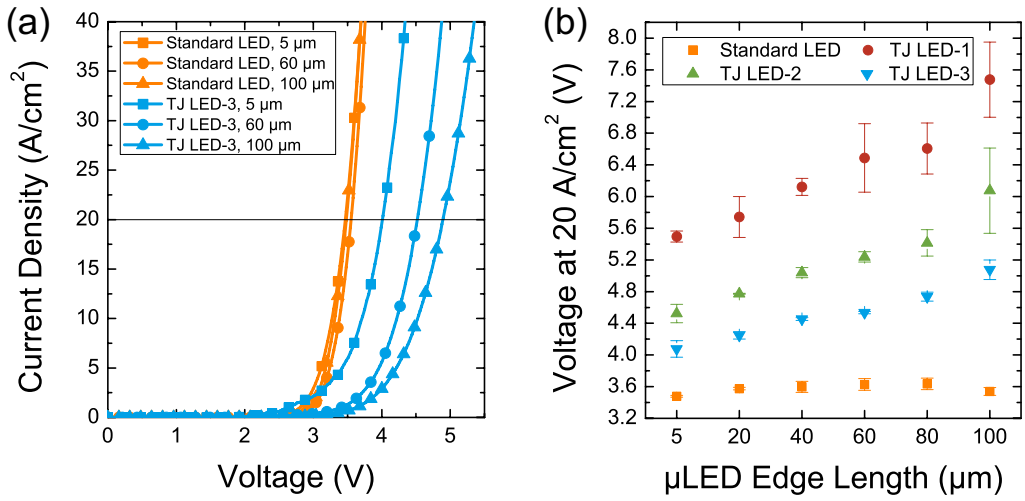


Figure 3.10: (a) Dependence of voltage on injection current density for various sized µLEDs for the standard LED (orange) and TJ LED-3 (blue). (b) Voltage at an injection current density of 20 A/cm$^2$ for the standard LED (orange squares), TJ LED-1 (red circles), TJ LED-2 (green upward triangles), and TJ LED-3 (blue downward triangles). Figure from Hwang *et al.* [104].

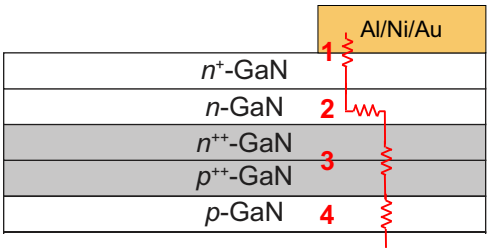


Figure 3.11: Breakdown of the different sources of resistance.

sistances for TJ µLED-1, -2, and -3 were $3.1 \times 10^{-6}$, $2.4 \times 10^{-6}$, and $8.1 \times 10^{-7}$ $\Omega \cdot \text{cm}^2$, respectively. At an injection current density of 20 A/cm$^2$, this difference in specific contact resistance results in a voltage difference of 0.046 mV. Therefore, the voltage contributions from the metal contact resistance and current spreading resistances (sources (1) and (2) of Figure 3.11) were negligible.

The main sources of resistances came from the tunnel junction barrier and the *p*-GaN. Since the activation mechanism was lateral diffusion of hydrogen, the centers of the µLEDs may not have been completely activated. For the smaller µLEDs compared with the larger ones, a larger percentage of the µLED area was activated because the lateral diffusion length for hydrogen was smaller. Areas that were not completely activated (e.g. areas with partial passivation of Mg acceptors by hydrogen) would add resistance due to both sources (3) and (4) of Fig. 3.11. Incompletely activated *p*-GaN would have lower carrier (hole) concentrations, which would increase the depletion width (see Fig. 3.2) and would also have higher resistances within the *p*-GaN layer. The added resistances were reflected in the higher forward voltages as the area increased for a given TJ condition (Fig. 3.10(b)). The voltage penalty of the tunnel junction, which is the difference in voltage between the TJ µLED and the standard µLED additional voltage, also changed between differently doped samples. For a given size at 20 A/cm$^2$ amongst the TJ µLEDs, the voltage penalty decreased with higher doping of the $n^{++}$-GaN TJ layer. This improvement was expected because the depletion width decreases with higher

doping. As the doping increased from $7.0 \times 10^{19}$ to $1.1 \times 10^{20}$ to $1.7 \times 10^{20}$ cm$^{-3}$ (TJ µLED-1, -2, -3, respectively), the additional voltage from the TJ dropped from 2.02 to 1.05 to 0.60 V for the $5 \times 5$ µm$^2$ µLED, from 2.86 to 1.61 to 0.91 V for the $60 \times 60$ µm$^2$ µLED, and from 4.86 to 3.52 to 1.62 V for the $100 \times 100$ µm$^2$ µLED. By increasing the doping 2.4 times, the TJ voltage penalty dropped by at least threefold. In addition to the absolute values of the voltage, the spread of the voltage at 20 A/cm$^2$ was reduced with increasing silicon doping.

The importance of the surface treatment prior to the tunnel junction regrowth is shown in Figure 3.12(a). The forward voltage at 20 A/cm$^2$ for the $5 \times 5$ µm$^2$ µLED was reduced from 5.48 to 4.28 V with the surface treatment, and similar reductions occurred for the larger µLEDs. Prior work by Yonkee *et al.* on hybrid MBE-MOCVD tunnel junction LEDs also showed improvements in voltage with acidic surface treatments and observed drops in both the oxygen and magnesium concentrations [95].

### 3.2.4 Optical results

The EQE behavior as a function of current density for the $40 \times 40$ and $100 \times 100$ µm$^2$ µLEDs is shown in Fig. 3.13. The three TJ µLEDs had higher peak EQEs and lower droop than the standard µLED, which may be attributed to more uniform current spreading on both the *p*- and *n*-sides as well as a more optically transparent layer (*n*-GaN versus ITO) [86, 96]. Furthermore, since the TJ µLEDs went through a surface treatment, the Mg concentration was lower. Because of this reduction, there may be less free carrier absorption from the Mg [105, 106]. As the ionization energy for Mg in *p*-GaN is high, there was a high concentration of non-ionized acceptor atoms, which had holes bound to them. These holes were not available to contribute to conductivity but enabled optical absorption by introducing empty states above the valence band edge. In the same vein,

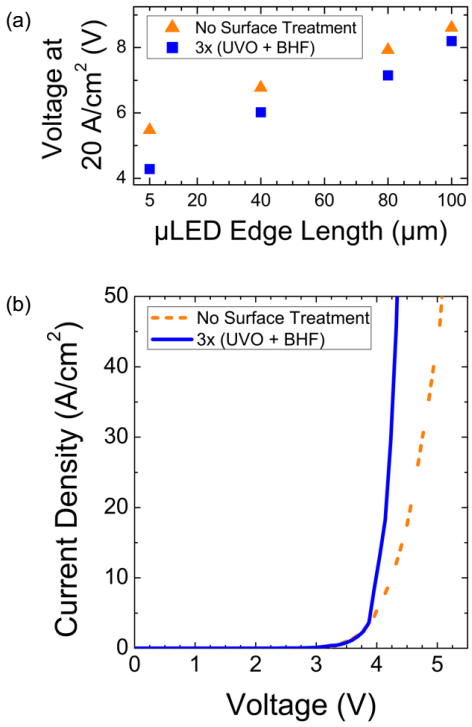


Figure 3.12: Effect of surface treatment on operating voltage and current. (a) Voltage at 20 A/cm$^2$ for the μLEDs without surface treatment (orange triangles) and with treatment (blue squares). (b). Current density versus forward voltage for the $5 \times 5$ μm$^2$ device.

the ITO thickness was not optimized for μLED performance. Thick films of ITO are typically used for higher current spreading but are also more absorbing. For μLEDs of these dimensions, thinner films of ITO may potentially be used without worsening the electrical performance. The peak EQEs of all the TJ μLEDs ranged from 30.6% to 33.7%, as was expected since the activated areas should have been similar. The standard μLED had a peak EQE of 25.3%. The droop of the TJ μLEDs at 50 A/cm$^2$ ranged from 5.6% to 9.5%, which was lower than that of the standard μLED, which varied from 12.4% to 16%. This trend of similar EQEs for the TJ μLEDs held between the $40 \times 40$ and $100 \times 100$ μm$^2$ devices and was also seen with the other sized μLEDs.

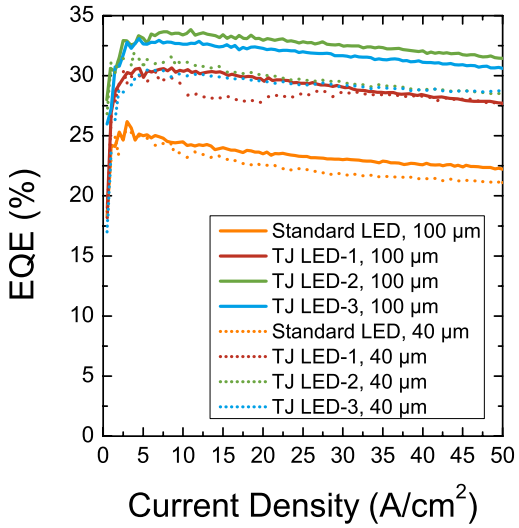


Figure 3.13: EQE as a function of current density for the 40 × 40 (dotted lines) and 100 × 100 µm$^2$ (solid lines) µLED. Figure from Hwang *et al.* [104].

## 3.3 Reduction of tunnel junction voltage penalty

The biggest question remaining from Chapter 3.2 is why there is a dependence of voltage on µLED size. From Kuwano *et al.* [87] and Figure 3.9, it seemed that µLEDs would be the perfect application of the lateral diffusion of hydrogen. The results of Chapter 3.2 reject that hypothesis though. These results suggest there is a barrier to lateral diffusion that traps the hydrogen within the *p*-GaN layer. This section proposes various possibilities and highlights experimental results aimed at removing the barrier.

### 3.3.1 Barrier to lateral activation formed via dry etch

To activate tunnel junction µLEDs, a mesa was first etched with chlorine-based chemistry assisted by Ar plasma with either a RIE or ICP tool. The effects of this dry etch and plasma exposure on *p*-GaN has been studied by Cao *et al.* [107]. First, a comparison between exposure of either Ar or $H_2$ plasma was studied. Two parameters of the ICP

were varied: the source power (or ion flux incident on the sample) or rf chuck power (average ion energy). The main findings were that as the source power or rf chuck power were increased, the forward turn on and breakdown voltages increased. Furthermore, since $Ar^+$ ions are heavier than $H_2^+$ ions, Ar-based plasmas created more damage. A loss of $N_2$ near the surface also introduced nitrogen vacancies, $N_V$, which act as shallow donors. A large concentration of $N_V$ (if comparable to hole concentrations) would then result in type conversion of the *p*-GaN to *n*-GaN up to a depth of about 400 Å. A wet etch in heated NaOH at 100°C removed some of the damaged material and restored the electrical properties of the initial film.

Another comparison was done looking at chlorine-based etches [108]. The study found that $Cl_2$/Ar ICP etches also induced type conversion and damage to a depth of 500 Å. Annealing between 700 to 800°C would partially recover the electrical properties but not completely (breakdown voltage was recovered to 70% of its initial value). Annealing higher than 800°C led to nitrogen vacancies, which was detrimental since it induced type conversion. Furthermore, annealing at these high temperatures may be damaging to InGaN LEDs, as decomposition or diffusion of GaN/InGaN is more probable at these temperatures. Once again, a wet etch in NaOH at 100°C would also remove some damage, but a combination of an anneal between 700-800°C and a follow up wet etch in heated NaOH yielded more complete recovery.

Motivated by the use of annealing and wet chemical etching, Yang 2009 *et al.* studied the use of annealing and wet chemical treatments on InGaN-based LEDs [109]. The wet chemical treatment was done with KOH, which etched away plasma-damaged sidewalls. This treatment suppressed surface leakage currents but also attacked metal contacts and increased the forward turn-on voltage. The best electrical results (recovery of turn on and breakdown voltages) were using both an anneal at 700°C and wet chemical treatment in ammonium sulfide. Sulfide passivation with ammonium sulfide, $(NH_4)_2S$, removed

unstable native oxides and formed GaS [110]. These Ga-S bonds have been shown to reduce surface recombination in GaAs and remove Fermi level pinning at the surface. The treatment has also been shown to be effective for InP passivation.

Referring back to work by Neugebauer *et al.* [82], diffusion of hydrogen in $n$-GaN is prohibited. Thus, the dry etch used in the formation of µLED mesas was creating a barrier to hydrogen diffusion. Physical plasma damage and type conversion need to be treated in order to achieve low voltage tunnel junction µLEDs.

### 3.3.2 Barrier removal methods

To deal with the barrier induced by the dry etch, a combination of annealing and chemical treatment was done. To study the effects of the chemical treatment, three samples were fabricated: standard µLEDs using 40 nm of ITO, tunnel junction µLEDs without a chemical treatment, and tunnel junction µLEDs with a chemical treatment. For the tunnel junction µLEDs with chemical treatment, the samples were first placed in concentrated KOH (approximately 12M) heated at 80°C for 30 minutes before the anneal. Then, both tunnel junction µLEDs underwent an activation anneal (700°C for 30 minutes in air) that also doubled as an anneal to recover electrical properties. The standard µLEDs did not undergo an anneal after the mesa etch.

Figure 3.14 shows the average forward voltages at 20 A/cm$^2$ for all three samples. As expected, the standard µLEDs hovered around 3.1 to 3.2V and did not change with µLED size. The TJ µLEDs without the chemical treatment showed similar behavior as in Figure 3.10, where the voltage increased with size. Furthermore, the voltages for each size spanned a wide range (standard deviation as large as 0.64V), signifying non-uniform hole concentration across the mesa. This inhomogeneity would occur if the sidewall perimeter had different levels of plasma-induced damage or type conversion. In

this case, different levels of hydrogen would diffuse out of the $p$-GaN, leaving a spread of hole concentrations across the mesa. Another explanation for the spread would also be epitaxial non-uniformities that resulted in different dopings across the mesa. However, these epitaxial non-uniformities were present in the standard sample as well, which did not exhibit the spread. Thus, the spread was likely due to the barrier at the perimeter. Finally, the average voltage of the TJ µLEDs with the chemical treatment was in between the other two samples. The voltages were lower than the TJ µLEDs without chemical treatment and were within a tighter range (standard deviation of 0.25V compared with 0.64V). This data showed that the chemical treatment did help with the barrier at the sidewall since the voltage was lowered, but the size dependence was still present and the barrier was not completely eliminated.

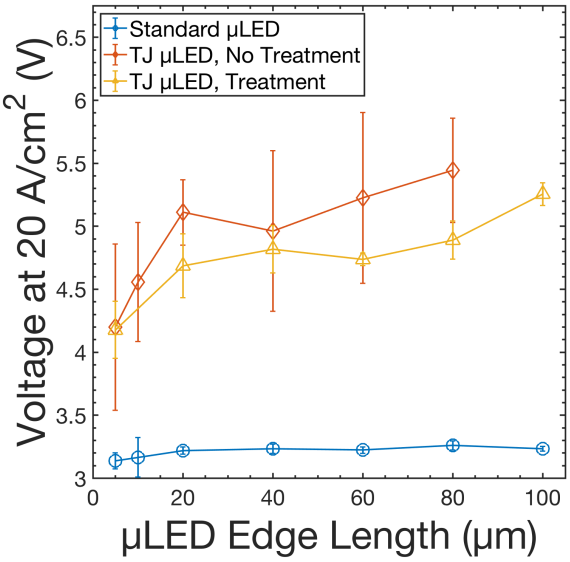


Figure 3.14: Voltage at an injection current density of 20 A/cm$^2$ for standard µLEDs with ITO (blue circles), TJ µLEDs without chemical treatment (red diamonds), and TJ µLEDs with chemical treatment (yellow triangles).

## 3.4 Summary and future work

In summary, we have shown that InGaN µLEDs with tunnel junction contacts may be grown solely by MOCVD. Electroluminescence images showed light emission across the mesa, but the forward voltages indicated incomplete activation. An analysis of the voltages of different Si-doped tunnel junction contacts confirmed that the higher doped tunnel junctions had lower voltage. However, there was still a dependence of the voltage on the µLED size. The voltage penalty of the tunnel junction for the smallest µLED at 20 A/cm$^2$ ranged from 0.60V to 2.02 V for the samples with highest and lowest doping levels, respectively. The peak external quantum efficiencies (EQE) for the tunnel junction LEDs were around 34% and were similar for all the doping levels, while the peak EQE of the standard LED was 25%. The cause of the incomplete activation arose from an activation barrier at the perimeter of mesa due to type conversion from dry etch damage. An anneal and chemical treatment were done to remove the barrier, and this treatment reduced the forward voltage and narrowed the spread of voltages for each size. However, the barrier was not completely removed as the voltage still increased with µLED size.

The use of tunnel junctions for µLEDs is still attractive to create multiple LED stacks on one wafer or to terminate the epitaxial stack with $n$-GaN to use $n$-type mirrors and contacts. However, before widespread adoption, the voltage penalty needs to be addressed. One direction is to increase the silicon doping of the $n^{++}$-GaN tunnel junction layer above $3.0 \times 10^{20}$ cm$^{-3}$. To incorporate more silicon, the disilane flow may be increased as shown in Figure 3.15. Up until 30 sccm disilane, there is a near-linear increase of silicon incorporation. However, past 30 sccm, the concentration saturates and dips. At this point, the solid solubility of Si in GaN has been reached. Figure 3.16 shows optical micrographs of the surface, and silicon precipitates are visible in the case of the films grown with 40 sccm disilane. One way to overcome this limit and increase

the doping concentration is to use delta doping.

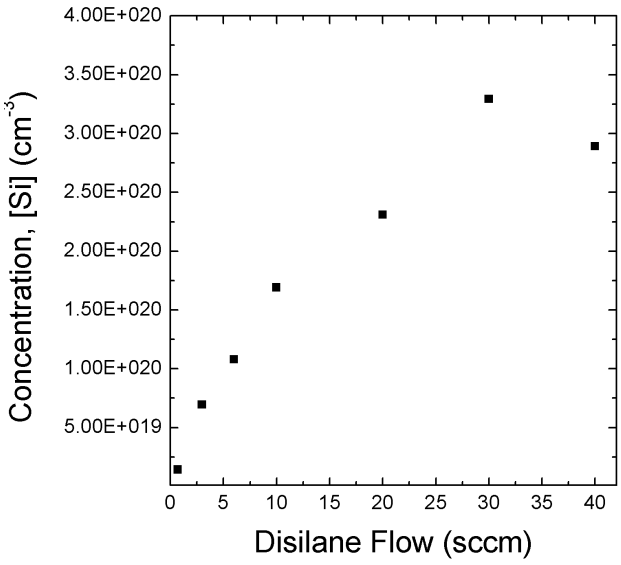


Figure 3.15: Si concentration of $n$-GaN grown by MOCVD as a function of disilane flow.


Figure 3.16: Optical micrographs of the surface of $n$-GaN layers with disilane flows of 20, 30, and 40 sccm.

Another optimization would be the $p$-GaN doping. As shown in Figure 3.2, at a high enough donor concentration, any variation in hole concentration has a more significant effect on depletion width (e.g. tunneling probability). The as-grown magnesium concentration must be increased because the surface treatment that is done before the tunnel

junction regrowth halves the concentration. A balance must be struck, because higher $p$-doping decreases the depletion width but also leads to more free carrier absorption.

In addition to $n$- and $p$-doping, the insertion of an InGaN polarization layer would help with tunneling. As Takasuka *et al.* showed, a graded high indium content $In_{0.4}Ga_{0.6}N$ layer collapsed the voltage of the tunnel junction LED to their standard LED [91]. The growth and characterization of high indium content InGaN is not trivial and must be done precisely. One example growth be to grow the LED with a terminating $p$-InGaN layer, remove the epitaxy from the reactor for a surface treatment, and regrow the $n$-type layer. In this method, the indium content of that terminating $p$-layer is hard to determine as there will be desorption of the indium during the cool down. Nevertheless, this InGaN layer insertion is promising.

Finally, and perhaps most importantly, the activation barrier at the mesa sidewall needs to be addressed. Although anneals at 900°C have shown to be effective in the literature, the temperature is too high for InGaN µLEDs. At high temperatures, decomposition of GaN and diffusion of indium is possible. The $(NH_4)_2S$ treatment seems promising [110], but a wet chemical etch may not solve the entire issue.

# Chapter 4

# µLEDs with Current Apertures

## 4.1 Current aperture options

As discussed in Chapter 2, the efficiency drop with decreasing µLED size stems from the presence of a surface and associated dry etch damage (see Figure 2.4). This sidewall creates defect states or dangling bonds that serve as sinks for carriers and nonradiative recombination. µLED designs that are "mesaless" (those without a sidewall) or that have the sidewall far from the light-emitting region may circumvent this loss. The best way to achieve this design is to use a current aperture and only inject carriers to the desired light-emitting region. In the III-nitride system, one may take advantage of the high resistance of $p$-GaN to create this aperture. The terminating layers of a µLED are typically $p^+$-GaN and $p$-GaN as shown in Figure 4.1. Current may be confined by rendering areas of the $p^+$-GaN resistive. Once that area is resistive, all current will be injected only to the conductive (non-damaged) $p^+$-areas. Furthermore, because of the high resistance of $p$-GaN, there will be very little lateral current spreading. Thus, radiative recombination will only occur where current is injected.

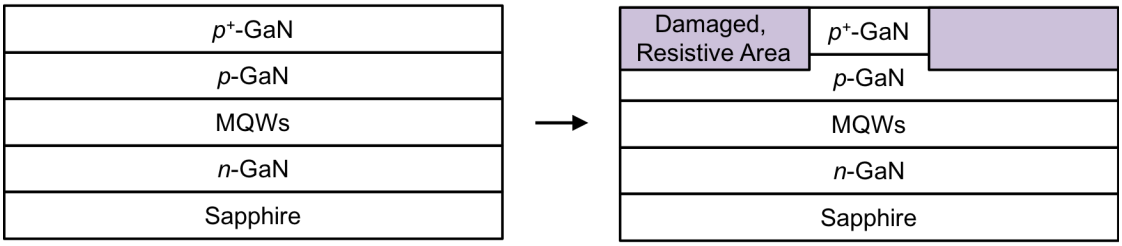


Figure 4.1: Schematic of a current aperture with a selectively damaged $p^+$-GaN region.

To create this aperture, the $p^+$-GaN must be damaged in some way. A few methods of creating this current aperture include plasma damage, oxidation of the $p$-GaN into $p$-$Ga_2O_3$, or ion implantation with various species. Exposure to high density Ar, $H_2$, or $O_2$ plasma introduces shallow donor states in the form of nitrogen vacancies (also discussed in Chapter 3.3) to compensate for holes near the surface of the $p$-GaN [107, 111]. Cao *et al.* showed that the plasma decreased the $p$-GaN conductivity, but the effects may be reversed by annealing or wet chemical etching. Another method is to oxidize the GaN, which has been done by dry oxidation in air [112–114] or by a photoenhanced wet oxidation [115]. Dry oxidation done at low temperatures such as 450°C yielded incredibly slow rates (almost immeasurable) and thus needed to be done at elevated temperatures such as 800 and 900°C. Still, the oxidation rate was still as slow as 20 nm/hour. The photoenhanced wet oxidation method utilized a UV light source (253.7 nm mercury source) and phosphorus acid solution with $p$H between 3 and 4. The oxidation rate was 224 nm/hour, 10 times faster than the dry oxidation rate. A third method is to use ion implantation, which has been studied to introduce dopants or to create electrically insulated layers and current blocking layers [116–123]. Commonly used implant species include silicon, magnesium, hydrogen, oxygen, and aluminum. Huang *et al.* selectively implanted LED films with hydrogen to avoid light being emitted below the $p$-metal contact that would eventually be absorbed by the metal [124]; Kim *et al.* implanted with nitrogen to achieve a similar purpose [125]. When $p$-GaN is implanted with hydrogen,

the insulation may be reversed by annealing (similar to activating as-grown $p$-GaN by driving out hydrogen from Mg-H complexes). Other groups have used silicon to insulate $p$-type regions [126, 127]. Consequently, Meyaard *et al.* created mesaless LEDs [127] by creating an isolation region between $p$- and $n$-GaN. Finally, Leonard *et al.* ion implanted nonpolar vertical-cavity surface-emitting lasers (VCSELs) with aluminum to improve lateral confinement and to decrease the threshold current density [128].

Among these methods, ion implantation may be most suitable to fabricate µLEDs. Plasma treatment may not completely make the $p$-GaN electrically resistive (or else high bias powers are required), and the effects are also reversible. The use of plasma may also damage the quantum wells, since the free radicals may penetrate through to the InGaN layers. Dry oxidation is unsuitable because it requires extensive times at high temperatures. These oxidation temperatures above 800°C may harm the InGaN quantum wells. Photoenhanced wet oxidation seems promising but will require precise masking so that areas with dimensions of tens of micrometers are protected and left as $p$-GaN. In this work, µLEDs were fabricated with current apertures defined by ion implantation of aluminum. Chapter 4.2 will detail the conditions for ion implantation of Al into GaN, Chapter 4.3 will highlight the nanofabrication process and design of experiments, and Chapter 4.4 will show preliminary results. Future work and directions will be discussed in Chapter 4.5.

## 4.2 Modeling of ion implantation conditions

Ion implantation is a method where impurity atoms are ionized and accelerated through an electric field to strike and enter the target. The ion energies and doses typically range from $1 - 100$s of keV and $10^{11} - 10^{16}$ cm$^{-2}$, respectively. When the ion penetrates the semiconductor crystal, it goes through electronic or nuclear stopping. Electronic

stopping occurs when the incident ion interacts with and is scattered by the electron cloud of the host atoms. Although a single Coulombic interaction is fairly weak due to the large mass difference between an ion and electron, several hundred thousands of these interactions may occur. On the other hand, nuclear stopping occurs when the incident ion collides with the target atoms. In this case, a significant amount of kinetic energy may be transferred from the high energy incident ion to the atom's nucleus. Consequently, the nucleus may further distort the crystal lattice by colliding with neighboring nuclei. Thus, one concern with ion implantation is the damage caused, which is exhibited as point defects such as vacancies. This damage may sometimes be repaired by a subsequent anneal, in which the displaced atoms are supplied enough thermal energy to diffuse back to their crystal sites.

When a semiconductor is ion implanted, there is a skewed Gaussian distribution of ions because of the scattering events. The projected range is the depth reached by the maximum concentration. The longitudinal straggle is a measure of the additional distance that ions travel within the stopping material (in the same direction of the incident ion beam), and the lateral range and straggle are along the direction normal to the ion beam. To estimate the implantation depths, Stopping Range of Ions in Matter (SRIM) software was used [129]. SRIM is a Monte Carlo simulation that calculates the electronic and nuclear stopping events to produce the longitudinal/lateral projected ranges and straggles. Figure 4.2 is an example of the data produced by SRIM for an implant of Al into GaN at a dose of $10^{15}$ cm$^{-2}$ and an energy of 20 keV. The depth of the implant may be varied by changing the implant energy, which also changes the shape of the profile. Figure 4.3(a) plots the Al concentration versus depth into GaN while varying the implant energy, and Figure 4.3(b) shows the projected range and straggles versus implant energy. For the smallest implant energy modeled (10 keV), the majority of the Al ions only penetrated a few tens of nm of GaN, whereas the highest energy (150 keV) dose reached

a depth of a few hundred nm.

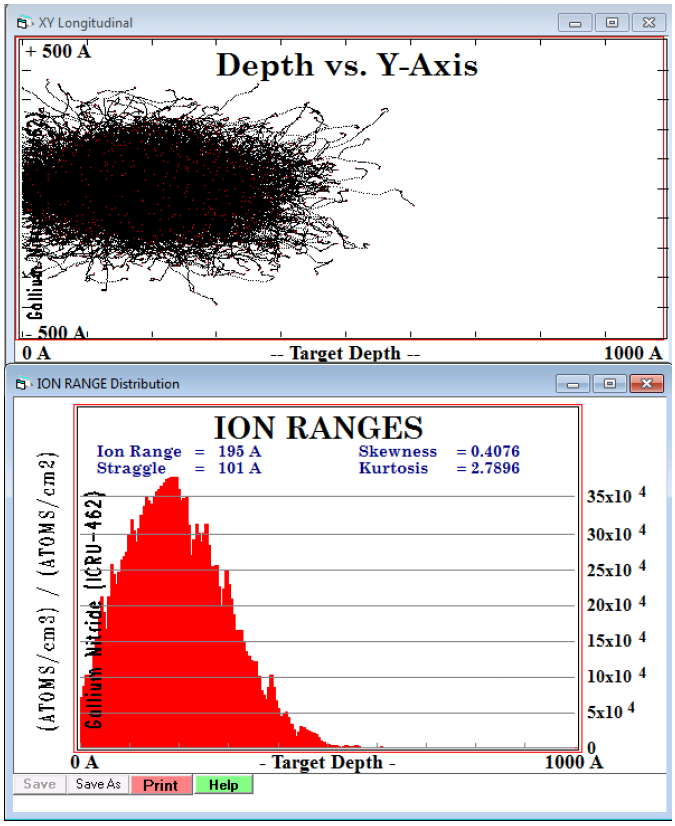


Figure 4.2: Example data output from SRIM.

To verify the SRIM modeling, freestanding $c$-plane GaN substrates were implanted with Al at a dose of $10^{15}$ cm$^{-2}$ at an incident angle of 7°. Al concentrations were then measured by secondary ion mass spectroscopy (SIMS). Figure 4.4 and Table 4.1 show the calculated and experimental Al profiles were in good agreement. The calculated and experimental projected ranges were within 0.7 nm of each other for all implant energies, although the experimental data showed a larger straggle (tail) of Al into the semiconductor. These tails were likely due to channeling of the ions. Channeling occurs when ions travel through paths that have fewer scattering events. To avoid the implantation of ions into channels, the crystal may be rotated a few degrees (typically 7°).

To see the effects of the anneal on the Al profile, implanted samples were annealed and

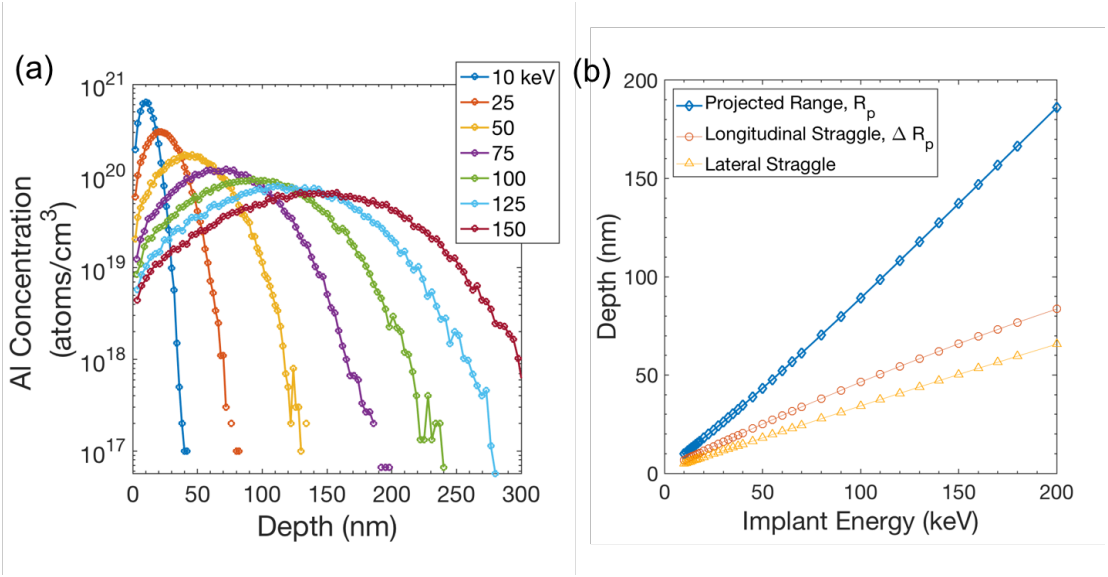


Figure 4.3: SRIM models of Al implanted into GaN with a dose of $10^{15}$. (a) Al concentration profiles and (b) projected range, longitudinal straggle, and lateral straggle versus implant energy.

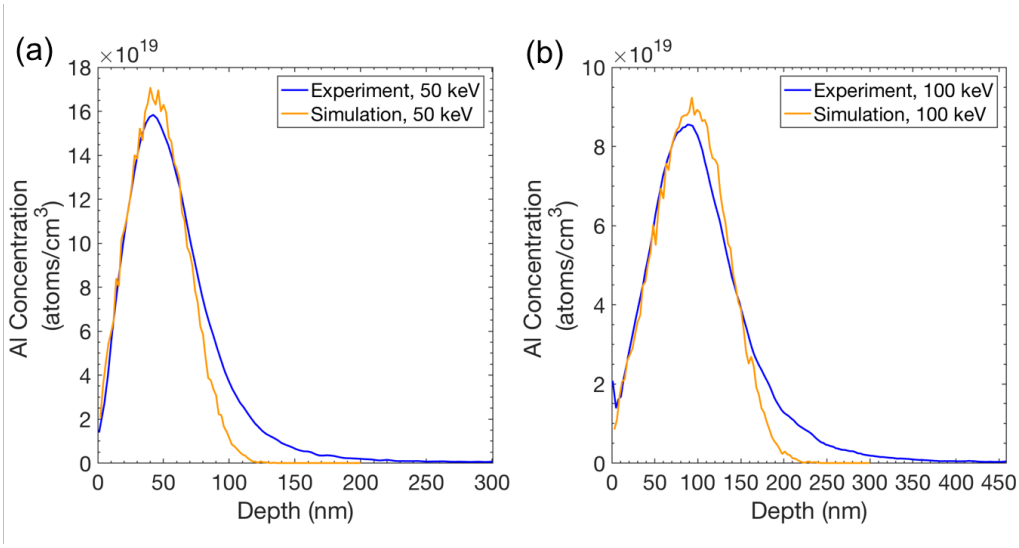


Figure 4.4: Comparison of Al profiles between calculated and experimental data for Al implanted at energies of (a) 50 keV and (b) 100 keV.

Table 4.1: Calculated (SRIM) versus Experimental (SIMS) Projected Ranges

| Implant Energy (keV) | Calculated $R_p$ (nm) | Measured $R_p$ (nm) |
|---|---|---|
| 20 | 19.3 | 10.2 |
| 50 | 40.0 | 39.3 |
| 100 | 93.0 | 93.8 |

measured in SIMS. After ion implantation, the GaN substrates were annealed at 700°C for 30 minutes in air. Figure 4.5 shows the anneal does not cause the Al to move around. However, the samples became more transparent, so the anneal allowed for defects to be repaired. This increase in transparency can be seen from Figure 4.6(a)-(b).

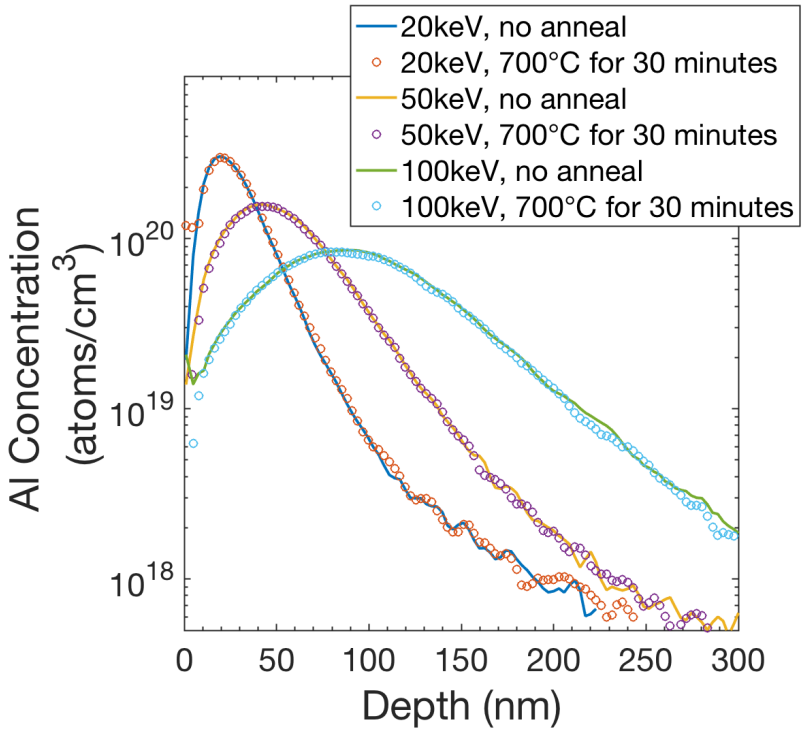


Figure 4.5: Comparison of Al profiles between calculated and experimental data.

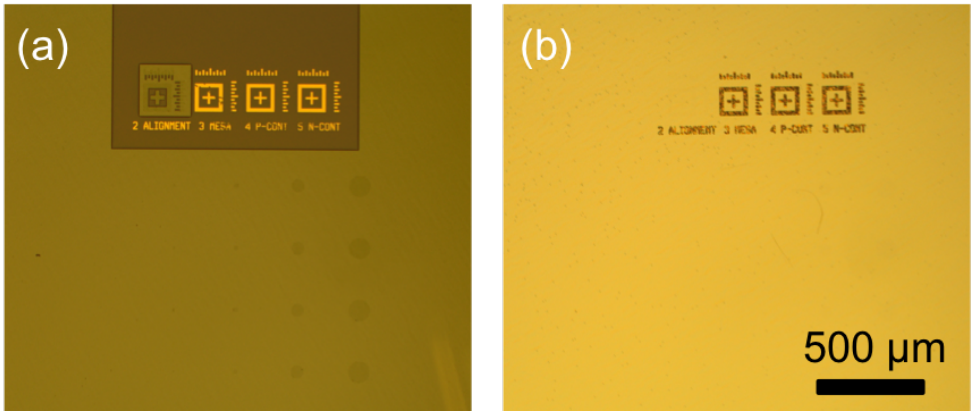


Figure 4.6: Optical micrographs showing samples after (a) ion implantation and (b) annealing. The anneal increases the transparency of the implanted regions.

## 4.3 Nanofabrication of µLEDs with ion implanted current apertures

To process µLEDs with ion implanted current apertures, standard µLED processing was followed but with a few additional steps at the beginning. The epitaxial structure was the same as those in Chapter 2. The first step was to implant the films with Al only in areas outside of the mesa, leaving an area that defined the µLED. To contact the $n$-GaN, a mesa was subsequently etched. To understand the effect of the current aperture, the distance from the light-emitting area (the µLED) to the edge of the mesa, X, was varied from 2, 5, 10 and 20 µm as shown in Figure 4.7. For larger values of X, there should be less nonradiative recombination at the sidewall surface; however, this additional volume meant more light may be absorbed or trapped. After the mesa etch, the dielectric was deposited to cover the sidewall and some of the mesa surface as well. The dielectric needed to cover the mesa surface because the subsequent $p$-metal deposition surrounded the mesa and sidewalls. Without the dielectric, the $p$- and $n$-GaN would be shorted.

µLED structures of six varying areas were processed (circles with diameters of 2, 5,

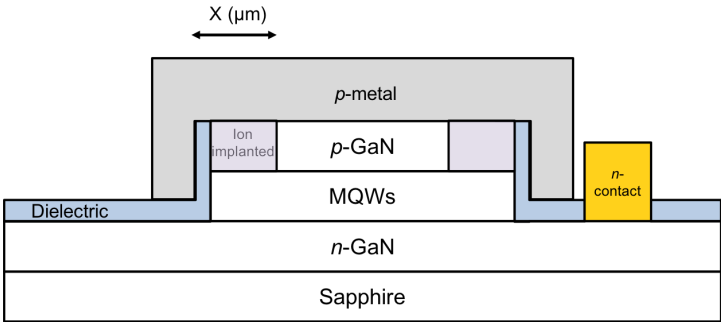


Figure 4.7: Cross-sectional schematic of μLED with ion implanted current aperture.

10, 20, 60, and 100 μm). First, a hardmask was deposited for the ion implantation. The hardmask metal and thickness were determined by SRIM. Up to energies of 200 keV, the Al penetrated to a depth of 300 nm, so a metal stack of 20 nm Ti and 500 nm of Au was deposited. Samples were sent to Leonard Kroko, Inc. for implantation with Al at a dose of $10^{15}$ cm$^{-2}$ at 20 keV with an incident angle of 7°. At this energy, Al should only penetrate past the $p^+$-GaN and only a few tens of nm into the $p$-GaN. After the implant, the hardmask was removed with Transene Gold Etchant TFA and Titanium Etchant TFTN. However, since the alignment marks were made of the same metal, they had to be covered with photoresist. After the hardmask removal, the samples were annealed at 700°C for five minutes in air to recover the damage from the implantation.

The mesa was etched by RIE using $Cl_2$. Figure 4.8(a) shows light emission from the inner circles, which defined the μLED area. The outer, concentric circle was the mesa ($p$-GaN), and the yellow area was the field ($n$-GaN). The dielectric deposition was defined by a self-aligned process rather than a separate lithographically defined process so that the mesa coverage was minimized. If the dielectric deposition were lithographically defined, then the dielectric may have covered too much area, and the $p$-contact area would have been significantly limited. For example, the best alignment would cause the SiN to come in 0.5 - 1 μm over the mesa surface. For a 10 μm diameter μLED, that would leave a circular area with a diameter of 9−9.5 μm for the $p$-metal. Since there is very little

lateral current spreading in $p$-GaN, light would only be emitted where the $p$-metal sat. Thus, only 81%−90% of the entire µLED area would emit light (81% is a result of taking the area of a 9 µm circle divided by the area of a 10 µm circle). To avoid this loss of area, a bi-layer resist (LOL2000 and SPR220-3.0) was used for the mesa etch. The first layer (LOL2000) was a thermal resist, which allowed for undercut. To get conformal coverage, SiN was deposited by sputter with the gun tilted. With this method, silicon nitride would be deposited on top of the mesa wherever the LOL2000 was undercut. A SEM image of the SiN coverage is shown in Figure 4.8(b). The $p$-contact, 20 nm Pd and 300 nm Au, was deposited via electron beam with a planetary stage. The planetary stage

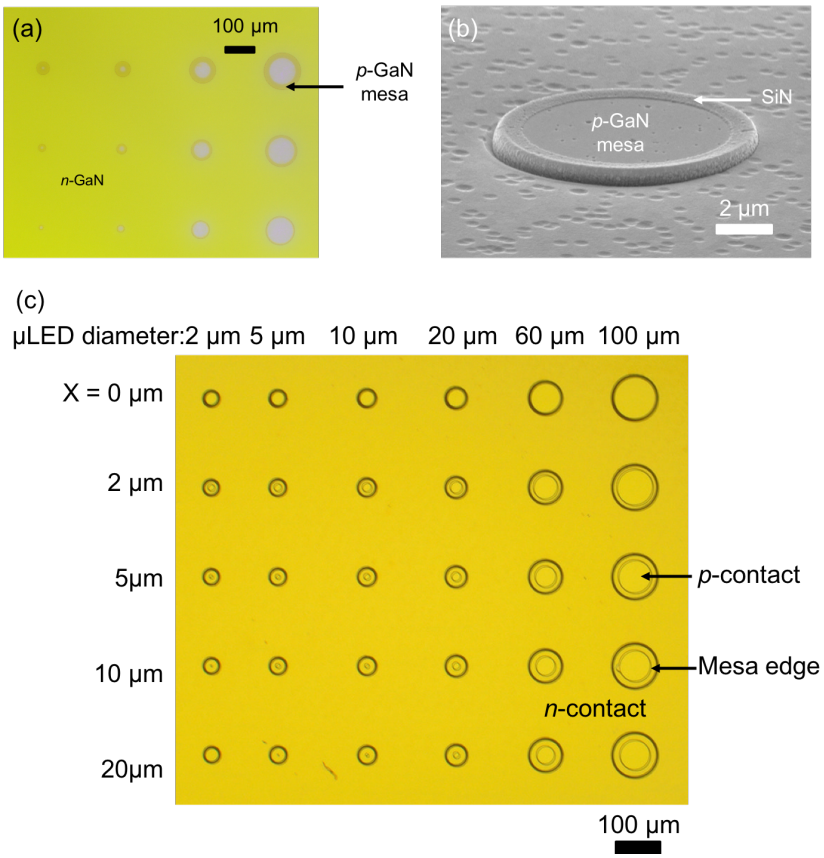


Figure 4.8: (a) Fluorescence micrograph showing light emission from the active region, (b) SEM image of dielectric coverage over the sidewall and atop the mesa surface, and (c) Optical micrograph of µLEDs with ion implanted current apertures.

was essential to get sidewall coverage. Finally, 20 nm Ti and 300 nm Au were deposited as the $n$-contact. Figure 4.8(c) shows a top-down view of the final device.

## 4.4 Preliminary results

After fabrication, on-wafer measurements were taken by probing the metal contacts on top of the µLEDs. Backside light emission was measured through the sapphire substrate with a large-area photodetector. Figure 4.9 shows the current density versus voltage characteristics for the 10 µm, 20 µm, 60 µm, and 100 µm diameter µLED. The legend indicates the distance between the mesa sidewall and the edge of the implanted region (the X = 0 case had no ion implantation and served as a standard). For the electrical characteristics, there was no apparent trend for the different distances (X values) as was expected. The current should be confined to the non-ion implanted region, so the extra volume of material outside of the µLED should not matter.

For the optical effects of the ion implanted current aperture, there were a few competing effects. For smaller values of X (the µLED sidewall was closer to the dry etched mesa sidewall), the distance a carrier needed to diffuse to the sidewall was smaller (and increased the amount of non-radiative recombination). For larger X values though, there was more volume of material surrounding the µLED that absorbed the light. Figure 4.10 shows the effects of the X values on light output. For the smaller sized µLEDs (10 and 20 µm), the standard processing (no ion implantation) yielded the most light emission. Light output power was the lowest for the case of X = 2 µm and increased for higher values of X. This trend showed that more non-radiative recombination occurred when the mesa sidewall was closer to the µLED. For the 20 µm diameter µLED, the light output for the X = 20 µm case almost recovered to the µLED without ion implantation, and the light output for the µLEDs with X = 2, 5, and 10 µm were the same. However, the

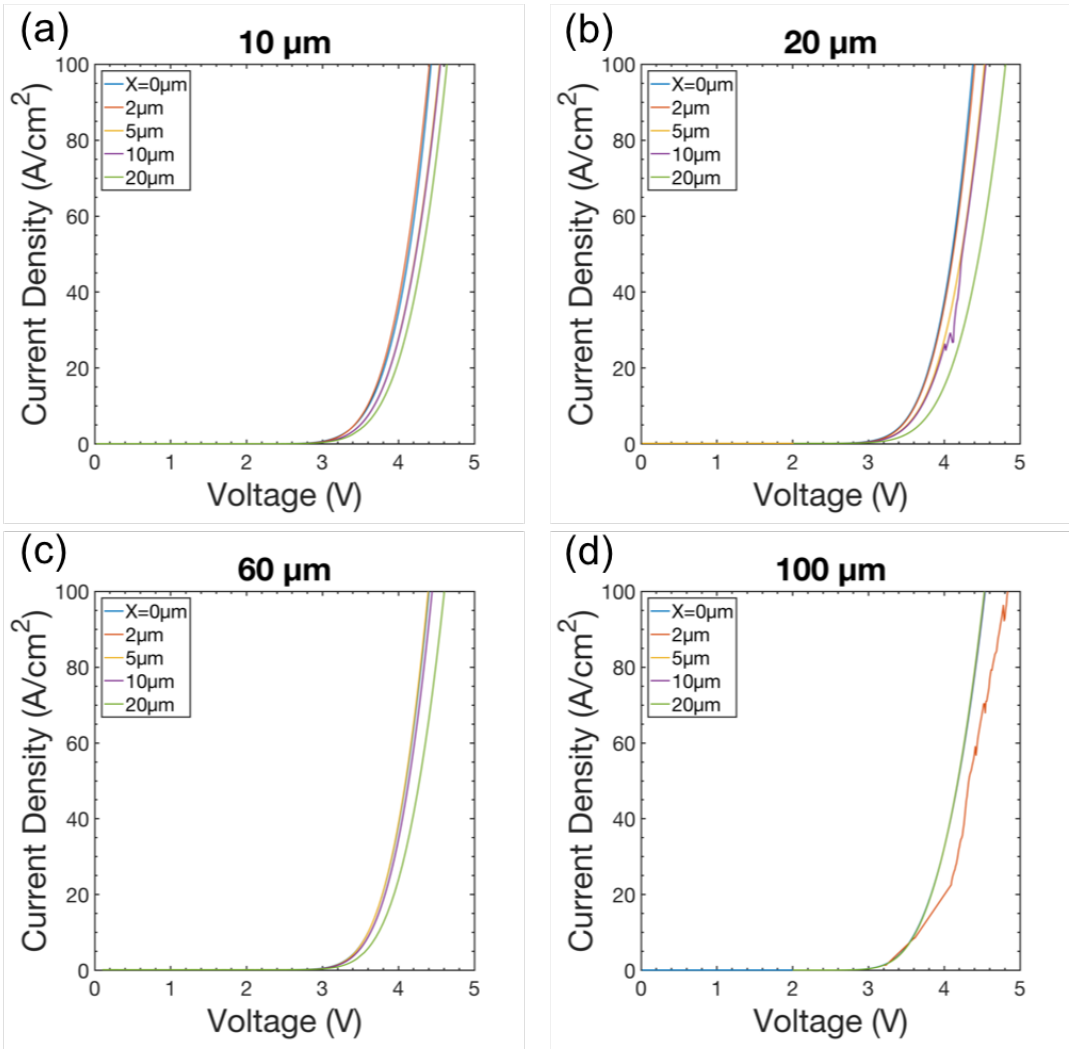


Figure 4.9: Current density versus voltage characteristics for ion implanted µLEDs, where X is the distance between the mesa sidewall and the active region. µLED diameters include (a) 10, (b) 20, (c) 60, and (d) 100 µm.

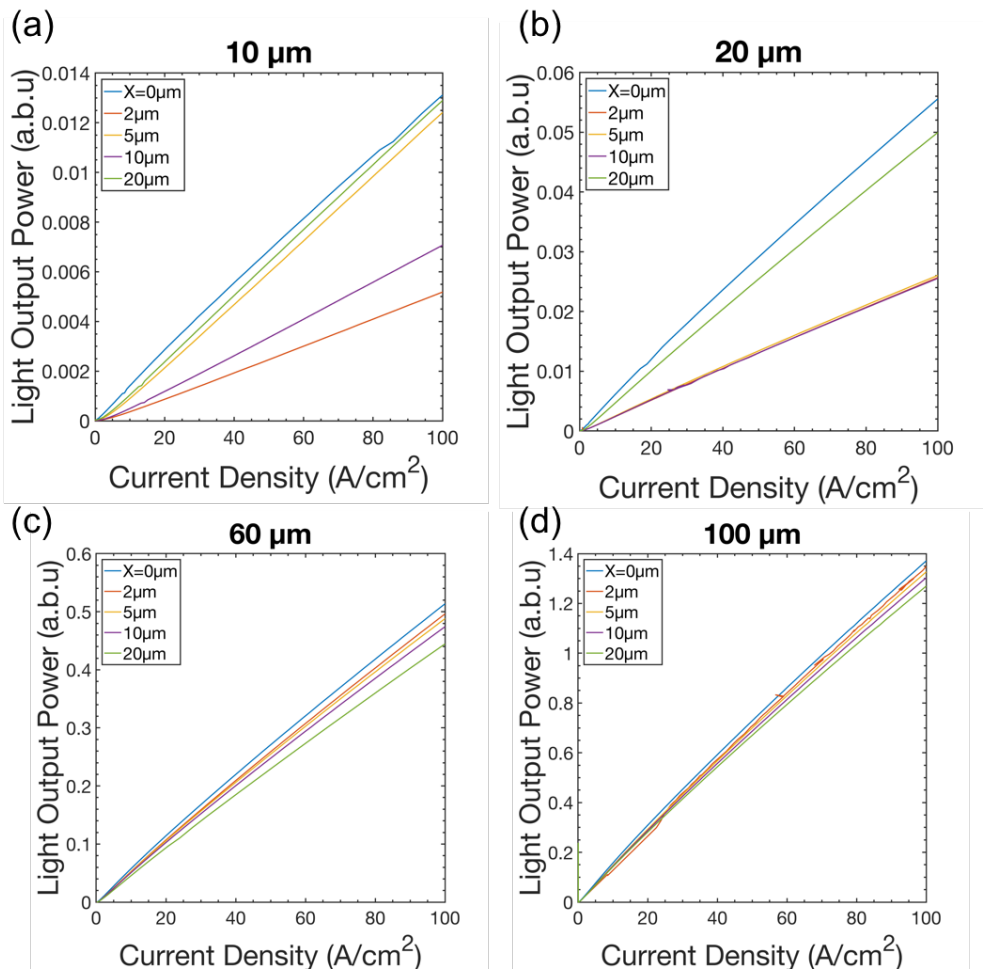


Figure 4.10: Light output power versus current density characteristics for ion implanted µLEDs, where X is the distance between the mesa sidewall and the active region. µLED diameters include (a) 10, (b) 20, (c) 60, and (d) 100 µm.

effect of larger absorbing volume dominated for larger sized µLEDs, and the light output power decreased with increasing X values. Since the perimeter was a lot less significant in larger µLEDs (as shown in Chapter 2), the amount of non-radiative recombination at the peripheral surface was less significant.

## 4.5 Summary and future work

µLEDs with an ion implanted current aperture were fabricated and measured. The initial hypothesis was that the current aperture would remove the sidewall of the dry etched mesa from the µLED and increase the light output power. However, the µLEDs without ion implantation showed the highest light output power (and thus, efficiency) for each size. This loss of efficiency may have come from the damage created by the ion implantation. During ion implantation, ions traveled in all directions, so the lateral straggle of the ion would cause damage closer to the µLED by creating vacancies and other point defects (non-radiative recombination sites). This lateral straggle was difficult to measure and control, so other methods may be needed to improve the efficiencies of small µLEDs.

As discussed in Chapter 4.1, other methods to create a current aperture involve damaging the $p^+$-GaN. Instead of inducing plasma damage or oxidation to define current flow, $p$-metal may be selectively deposited on the $p^+$-GaN to define the µLED area. For instance, if the $p$-metal is deposited in a 20 µm diameter circle, then light would only be emitted from this circle because of the limited lateral current spreading. With this method, the optical guiding effects must be considered. Dry etched mesas may be formed in a similar fashion as done in Chapter 4.4.

# Chapter 5

# Mass Transfer of III-Nitride µLEDs Enabled by PEC Liftoff

## 5.1 Introduction

### 5.1.1 Definition of mass transfer

Self-emissive, full-color (red, green, and blue, or RGB) displays are made of pixels. Each pixel is composed of individual red, green, and blue sub-pixels. For organic LED (OLED) displays, the different colors may be selectively placed or deposited by inkjet printing or thermal evaporation using a shadow mask [130]. These fabrication methods allow for roll-to-roll processing and high throughput. On the other hand, µLED-based displays face difficulties in manufacturing. An essential part of assembling such a full-color µLED display is mass transfer. As of now, there is no simple way to monolithically grow all three colors on the same wafer or with the same material system (e.g. InGaN or AlGaInP). Therefore, the individual colored µLEDs must first be processed from separate red, green,

and blue epitaxial wafers and then assembled. The process of arranging RGB sub-pixels is referred to as mass transfer. For the purpose of this discussion, mass transfer may be broken into two components (see Figure 5.1): (1) release of µLEDs from its growth substrate and (2) the transfer and assembly of those µLEDs. For conventional, large-area LEDs (0.1 to 1 $mm^2$) that comprise LED lightbulbs today, mass transfer is done by pick-and-place technology where a machine picks up an LED die using a vacuum hole and moves it to its necessary position. The size of the µLEDs that would be used in a display ($10^{-5}$ to $10^{-4}$ $mm^2$) is much too small for pick-and-place as the vacuum holes are too large.

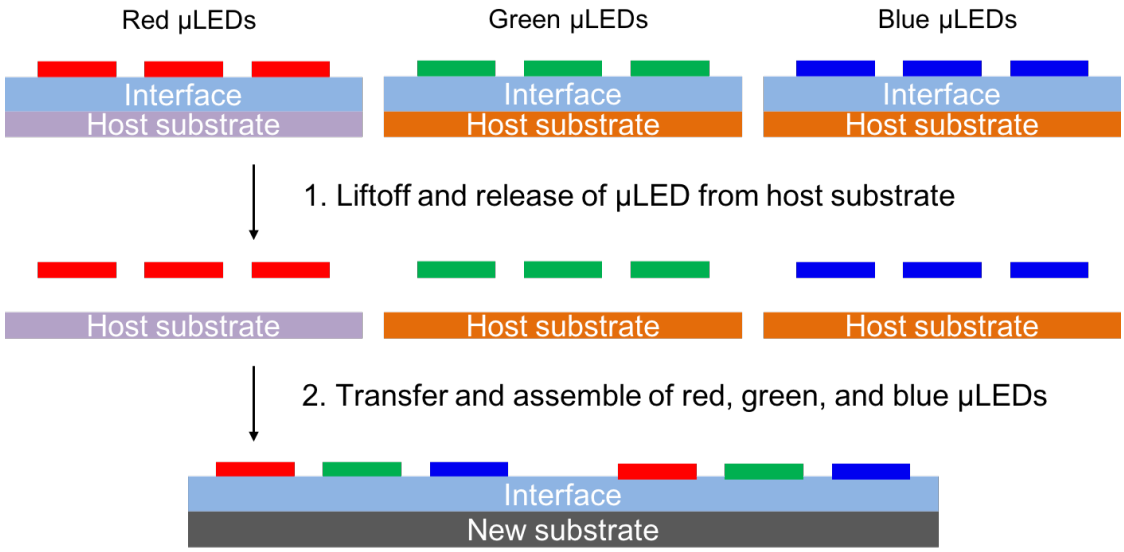


Figure 5.1: Schematic of generalized mass transfer process.

### 5.1.2 Review and limitations of mass transfer methods

To understand the curent state of industrial mass transfer processes, a basic review of the materials systems and growth methods used to create µLEDs is necessary. The emissive layer in red µLEDs is usually quarternary $(Al_xGa_{1-x})_{1-y}In_yP$ heteroepitaxially grown

on GaAs substrates by MOCVD. AlGaInP is lattice matched to GaAs, which reduces the dislocation density. In the red regime, AlGaInP is a direct bandgap material (the conduction band minimum is from the Γ valley) but undergoes a crossover and becomes indirect around 550 nm (CB minimum is of the X valley). Nevertheless, AlGaInP is a good material candidate for the deep red regime (see Chapter 1 for a more detailed discussion on AlGaInP).

As has been described throughout this thesis, the emissive layers of blue and green μLEDs are made from the III-nitride family. The range of the bandgap of InN alloyed with GaN spans the entire visible spectrum, so the wavelength of the emitted light may be changed with the indium composition of $In_xGa_{1-x}N$. The epitaxial growth of these films by MOCVD may be done as heteroepitaxy (on sapphire, silicon, silicon carbide) or as homoepitaxy (on freestanding GaN). The most commonly available commercial InGaN LEDs today are grown on sapphire.

The liftoff and release of μLEDs from their host substrate (part 1 of Figure 5.1) depends on the material system and growth substrate. The III-phosphides/III-arsenides family is relatively chemically reactive, so many wet etches are available [131]. On the other hand, GaN is much more chemically robust, and wet chemical etches are significantly limited [132, 133]. Liftoff techniques include laser lift-off (LLO) or incorporating a sacrificial layer (via hydrogen implantation or growth of ZnO).

LLO has been used to remove thin GaN films from sapphire since the 1990s (pioneering work was done by Wong [134] and Kelly [135]). Delmdahl *et al.* proposed the use of LLO to lift off GaN LEDs from sapphire substrates and have developed line beam processing for large area LLO [136,137]. LLO takes advantage of the difference in absorption coefficient between dissimilar materials by using a light source to irradiate a a selected layer. For lifting off GaN from sapphire, a light source with energy larger than the bandgap of GaN but smaller than the bandgap of sapphire (≈10 eV) is chosen. Three common sources

include a KrF excimer laser ($\lambda = 248$ nm), a XeCl excimer laser ($\lambda = 308$ nm), and a third-harmonic neodymium-doped yttrium aluminum garnet (Nd:YAG) laser ($\lambda = 355$ nm). The sapphire substrate is transparent (non-absorbing) to these wavelengths, and the lasers are above the absorption edge of GaN. The liftoff occurs by thermal decomposition of GaN when the laser irradiates the film (illustrated in Figure 5.2(a)-(b)). Ueda *et al.* calculated that the local temperature needs to be greater than 850°C for GaN to decompose into Ga and N according to the following reaction:

$$2\mathrm{GaN(s)} \rightarrow 2\mathrm{Ga(l)} + \mathrm{N_2(g)} \tag{5.1}$$

Once the laser irradiation is done, residual Ga droplets are removed by heating the sample above the melting temperature of Ga (30°C), and the lift-off is complete (Figure 5.2(c)).

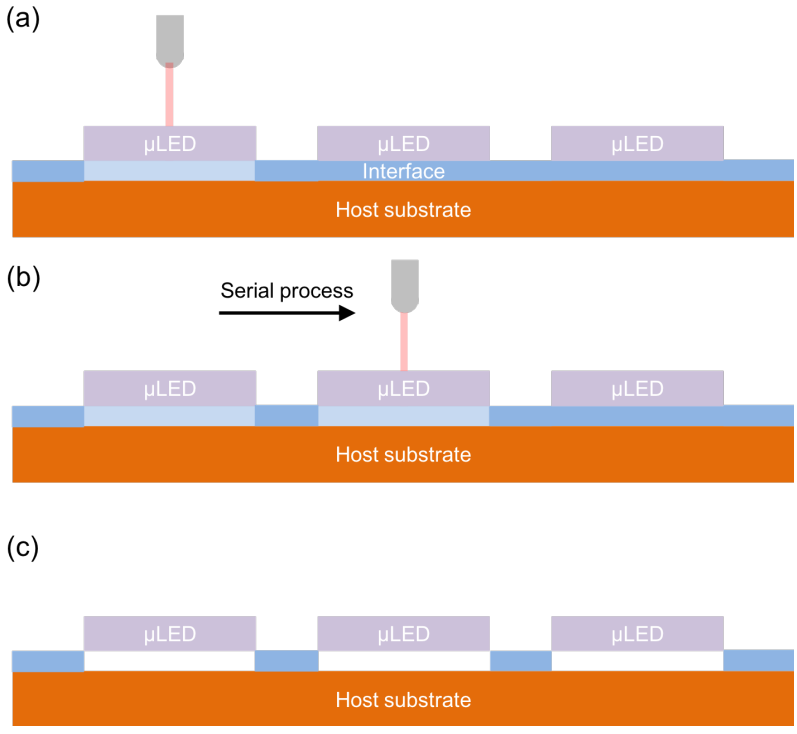


Figure 5.2: Schematic of laser-liftoff process.

LLO has traditionally only been possible for heteroepitaxially grown GaN; for GaN on GaN LEDs, there is no interface to absorb the laser energy. Iida *et al.* demonstrated the use of LLO of GaN UV-LEDs grown on freestanding GaN by creating In droplets instead of Ga [138]. After the sacrificial InGaN layer is grown, $n$-GaN and $n$-AlGaN layers are grown at elevated temperature (1040°C), which thermally decomposes the sacrificial InGaN to metallic In droplets. After the droplets are formed, the sample is irradiated with visible light using a second-harmonic Nd:YAG laser ($\lambda = 532nm$), and the substrate is removed.

Other methods to liftoff InGaN µLEDs include the formation of sacrificial layers. SmartCut™ is a commercial technology by Soitec and Sumitomo that uses ion implantation of hydrogen [139]. The method follows what was developed by Bruel in 1995 for making silicon on insulator (SOI) wafers [140] and relies on surface blistering and layer splitting induced by hydrogen implantation. This method has also been adapted to GaN [141, 142], and buckling on GaN has been studied intensively in the literature [121, 143]. Another method includes the growth of ZnO as a sacrificial layer because it can be etched away with HCl. ZnO films are either deposited by RF magnetron sputtering [144, 145] or pulsed laser deposition [146], and GaN/InGaN layers are grown by MOCVD. To liftoff the LED films, a HCl dip will etch away the ZnO.

The actual transfer and assembly mechanisms (part 2 of Figure 5.1) have received much more attention commercially. The leading methods include a MEMS-based pick and place system (developed by Luxvue and acquired by Apple in Silicon Valley) [147]; transfer printing with a PDMS stamp (demonstrated on III-V devices by Professor John Rogers' group in Illinois and commercialized by X-Celeprint) [148–150]; and a "Solid Printing" technique invented by VueReal in Waterloo, Canada that revealed a 6000 ppi display at the Society for Information Display's (SID) Display Week 2017 [151, 152].

As discussed in Chapter 1, µLEDs grown on freestanding GaN substrates offer many

advantages for µLEDs. They have narrower emission linewidths, smaller blue-shifts with increasing current (more stable colors), and the potential to reach longer wavelengths. Thus far, no technique has proven itself to be compatible for such µLEDs grown on freestanding GaN. The most widely used technique for liftoff of µLEDs has been LLO for GaN on sapphire (likely adopted by Apple, X-Celeprint, VueReal, etc), and while LLO has been shown to work for freestanding GaN, it has not been proven in a commercial setting. This chapter will detail the development on lateral PEC undercut and transfer printing. We also demonstrate for the first time red, green, and blue InGaN µLEDs transferred onto a single flexible and transparent acrylic substrate.

## 5.2 Background of PEC liftoff process

### 5.2.1 Overview of PEC liftoff enabled mass transfer process

This chapter is predominantly concerned with developing a liftoff and release technique compatible with freestanding GaN substrates and will detail the front-end of creating light sources for a RGB µLED display (the back-end of integration with CMOS technology and driving architecture will not be discussed). The process includes MOCVD growth (Section 5.3.1), nanofabrication (Section 5.3.2), liftoff and release from the substrate via lateral PEC etching (Section 5.3.3), and transfer printing µLEDs onto a new substrate (Section 5.3.4). Customized growths are necessary in order to grow a sacrificial layer of violet InGaN multi-quantum wells (MQWs) below the µLEDs. Nanofabrication processes must be tailored to be compatible with the PEC etch conditions, which include prolonged exposure to UV light and potassium hydroxide, KOH. This method has been shown to work for all freestanding GaN substrates (e.g. *c*-plane [153], semipolar [154, 155], and nonpolar [156, 157]) and other substrates such as sapphire [158]. The remainder of

Section 5.2 will describe the background of PEC etching and an application of PEC liftoff to large-area LEDs (while not related to µLEDs, this work served as the backbone to developing the µLED mass transfer technique).

### 5.2.2 History and principle of PEC etching

In the LED industry, PEC etching is typically used as a top-down roughening mechanism. Roughening of the nitrogen face (N-face) of GaN drastically improves the light extraction of *c*-plane GaN LEDs by increasing the escape cone through which light may escape a medium [159–162]. Cones in the shape of a hexagonal pyramid are formed on N-face when GaN is immersed in KOH, as shown in Figure 5.3. A higher magnification image of a single cone is shown in Figure 5.4. The $\{10\bar{1}\bar{1}\}$ planes are preferentially etched by KOH compared to the $\{000\bar{1}\}$ planes. Theoretically, the angle between the two planes is 58.4°, and Ng *et al.* measured the angle to be between $58 - 60°$. This preferential etch implies that the $\{000\bar{1}\}$ surfaces have the lowest surface energy.

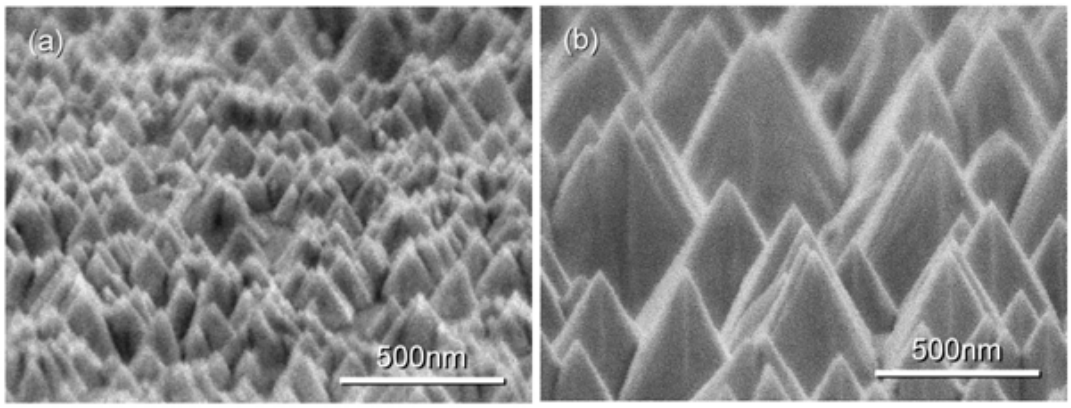


Figure 5.3: SEM micrographs of an *N*-face GaN surface etched by a KOH-based PEC method. (a) 2-min etching and (b) 10-min etching. Copyright 2004 The Japan Society of Applied Physics [159].

While the N-face is readily roughened in KOH, the Ga-face remains chemically inert

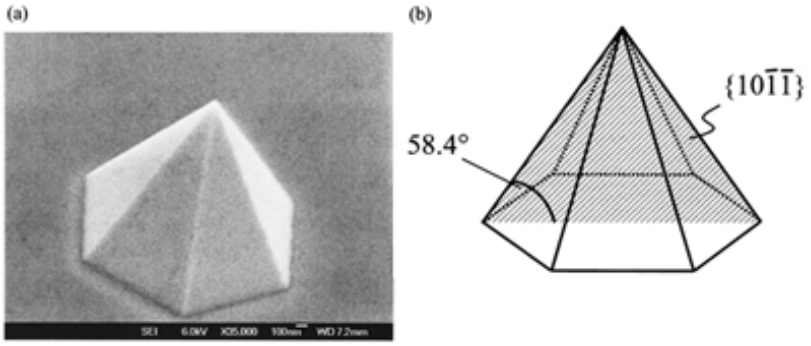


Figure 5.4: (a) A high magnification SEM image of a single hexagonal pyramid on top of the sapphire substrate. (b) Schematic drawing of the pyramid shown with the six $\{10\bar{1}\bar{1}\}$ facets and the angle between the edge and base of the pyramid. Reprinted from [H. M. Ng, N. G. Weimann, A. Chowdhury, *J. Appl. Phys.*, **94**, 650 (2003)] with the permission of AIP Publishing [160].

and is not etched. The chemical reaction that occurs is [163]:

$$2\mathrm{GaN} + 3\mathrm{H_2O} \xrightarrow{\mathrm{KOH}} \mathrm{Ga_2O_3} + 2\mathrm{NH_3} \tag{5.2}$$

Before this reaction can occur, hydroxide ions need to attack a Ga atom and be adsorbed on the $-c$ surface (Figure 5.5a-b). Gallium oxide is formed and dissolved in KOH, so etching occurs (Figure 5.5c-d). This process repeats itself on N-face. For Ga-face, the first atomic Ga layer can be removed by the oxidation and dissociation step. However, once that layer is removed, the resulting N-terminated surface has multiple dangling bonds. There is a large repulsion between $OH^-$ and the dangling bonds, so the adsorption of $OH^-$ onto Ga does not occur. However, for N-face GaN, there is only one dangling bond, so the $OH^-$ attack is possible.

Top-down PEC etching of GaN was first demonstrated by Minsky *et al.* who used a He-Cd laser emitting at 325 nm in both HCl and KOH solutions [164]. Khare *et al.* detailed work on both the dopant- [165] and bandgap-selective [166] nature of PEC etching of GaAs. PEC etching combines the use of a light source to generate carriers

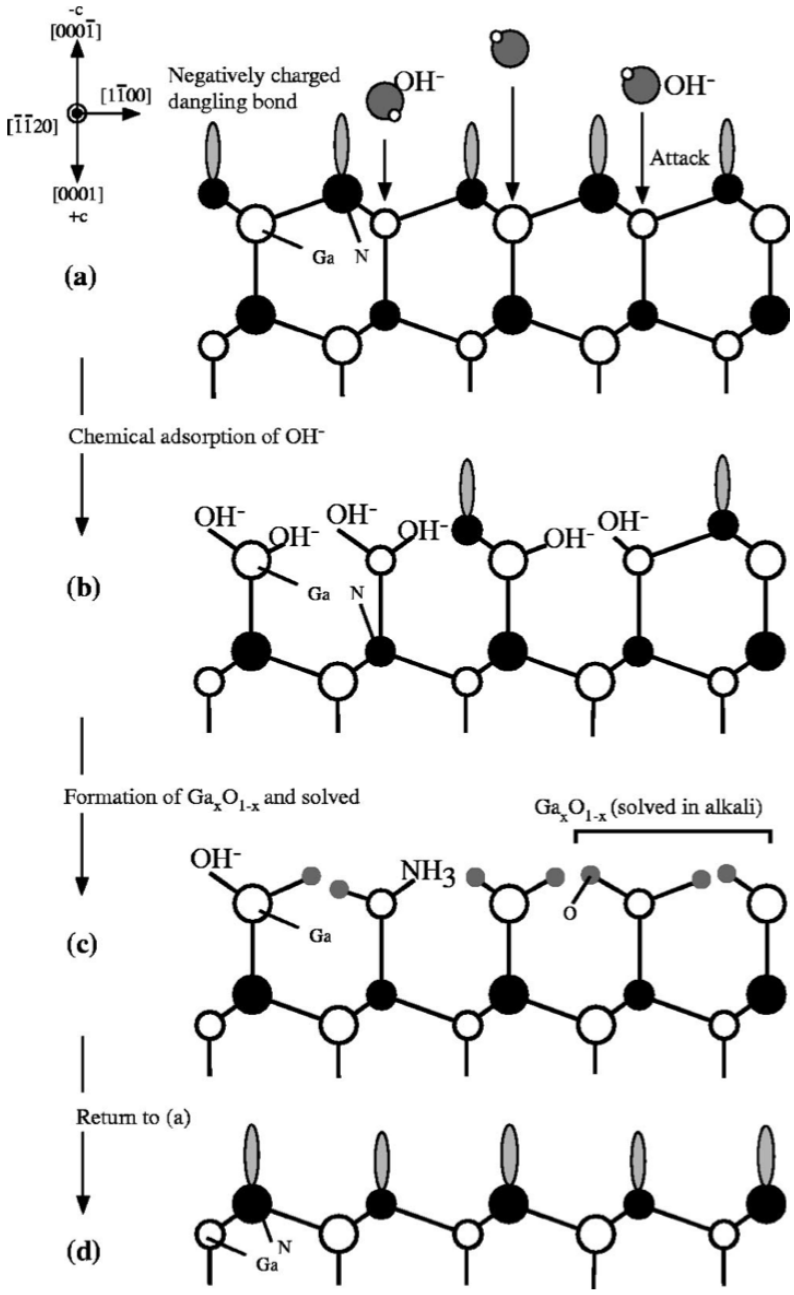


Figure 5.5: "Schematic diagrams of the cross sectional GaN film viewed along the [$\bar{1}\bar{1}$20] direction for $-c$ GaN to explain the mechanism of the selective etching." Reprinted from [D. Li, M. Sumiya, and S. Fuke, *J. Appl. Phys.*, **90**, 4219 (2001)] with the permission of AIP Publishing [163].

within a material that then reacts chemically with the material to be etched. For III-V semiconductors, the chemical reactions proceed as follows according to Van de Ven and Nabben's studies [167]:

$$h\nu \rightarrow e_{cb}^{-} + h_{vb}^{+} \tag{5.3}$$

$$\mathrm{AB} + 6h_{vb}^{+} \rightarrow \mathrm{A}^{3+} + \mathrm{B}^{3+} \tag{5.4}$$

$$\mathrm{Ox} + ne_{cb}^{-} \rightarrow \mathrm{Red} \tag{5.5}$$

In reaction 5.3, carriers are generated by a light source. The generated holes then oxidize III-V semiconductor (represented by AB) to form A and B in the 3+ oxidation state (dissociative reaction 5.4). The generated electrons reduce the oxidizing agent in the electrolytic solution (represented by Ox and Red). For PEC etching of GaN, the sample is immersed in an oxidizing electrolyte solution such as KOH. Metal deposited on the sample serves as the cathode where electrons will be extracted and reduction occurs. Holes oxidize the material to a soluble form in the electrolyte, and then the electrolyte dissociates the formed oxide. The actual chemical reactions proceed as follows [168]:

$$h\nu \rightarrow e_{cb}^{-} + h_{vb}^{+} \tag{5.6}$$

$$2\mathrm{GaN} + 6h_{vb}^{+} + 6\mathrm{OH}^{-} \rightarrow \mathrm{Ga_2O_3} + 3\mathrm{H_2}O + \mathrm{N_2}\uparrow \tag{5.7}$$

$$\mathrm{Ga_2O_3} + 6\mathrm{OH}^{-} \rightarrow 2\mathrm{GaO_3^{3-}} + 3\mathrm{H_2}O \tag{5.8}$$

The oxidized Ga metal reacts with the hydroxide group to form gallium oxide, and the oxidized nitrogen becomes $N_2$ gas, as shown in reaction 5.7. The formed oxide is then dissolved in KOH (reaction 5.8). The reactions of GaN in HCl are unpublished, but it is hypothesized that gallium trichloride ($GaCl_3$) is formed and then dissolved.

According to the above chemical reactions, the actual etching catalyst is a hole.

For complete etching to occur, holes must be confined in the appropriate area of the material. This condition makes PEC etching a dopant-selective technique [169,170]. The band structures of an $n$-type and $p$-type semiconductor immersed in oxidizing solution are shown in Figure 5.6. The bands bend up or down because there is a surface state that pins the Fermi level. Unoccupied dangling bonds of gallium pin the Fermi level between 0.5 eV below the conduction band and around mid-gap (the position is based on the Ga/N ratio) [171]. Therefore, in $n$-type material, the bands bend upwards towards the interface, so holes are confined at the surface. The formation of gallium oxide occurs at the semiconductor/electrolyte interface, and etching proceeds there. In $p$-type material, the bands bend downwards, so holes are swept away from the interface and etching is greatly reduced. Efforts have been made to etch $p$-GaN utilizing the internal electric fields of GaN [172], but PEC etching has been mostly applied to $n$-GaN.

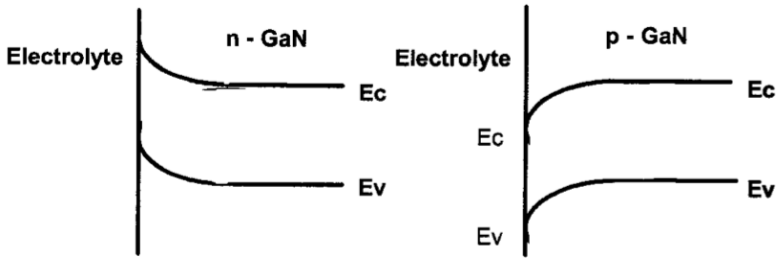


Figure 5.6: Band bending of $n$-GaN/electrolyte vs. $p$-GaN/electrolyte [170].

Youtsey *et al.* studied the surface morpologies of etched GaN samples (smooth vs rough) and concluded that the smoothness of the resulting surface depends on the regime in which the etch operates - either a generation-limited regime or a diffusion-limited regime [173]. Photocurrent was measured with an ammeter, and Figure 5.7 plots the photocurrent as a function of KOH concentration. In situations with low light intensity (in this figure, roughly below 10 mW/cm$^2$), a linear dependence of photocurrent on illumination can be seen. This linear portion is the generation-limited regime, where

the etch rate is proportional to the carrier generation rate. At higher intensities, the photocurrent saturates, and the diffusion-limited regime is entered, where the etch rate depends on the rate at which carriers diffuse to the surface.

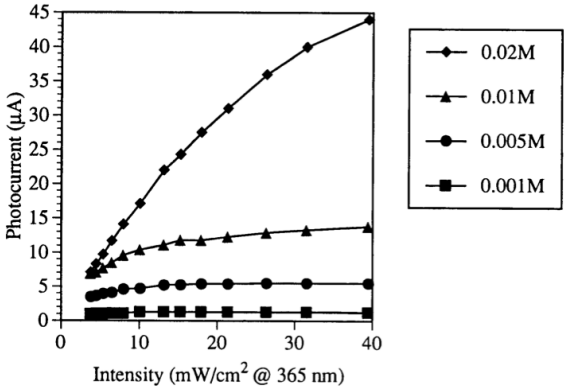


Figure 5.7: Variation of photocurrent with light intensity for different KOH solution concentrations. Reprinted from [C. Youtsey, I. Adesida, L. T. Romano, and G. Bulman, *Appl. Phys. Lett.*, **72**, 560 (1998)] with the permission of AIP Publishing [173].

Smooth etching (rms roughness of 1.5 nm) was observed in the diffusion-limited regime, where this is a saturation of photocurrent (high light intensities and low KOH concentration). In this regime, local variations in intensity do not significantly change the photocurrent or etch rate, so a smooth surface is obtained. When etching in the generation-limited regime (low light intensities or high KOH concentration), very rough morphologies were observed. These trends were seen for vertical (top-down) etching but may not be applicable to lateral etching in small dimensions.

The undercut etch rates and profiles of different InGaN layers were investigated by Haberer *et al.* [174]. Three different sacrificial layers were grown by MOCVD: a 300 nm $In_{0.04}Ga_{0.96}N$ post, a 3 period $In_{0.04}Ga_{0.96}N$/GaN (100 nm/20 nm) superlattice, and a 5.5 period $In_{0.04}Ga_{0.96}N/In_{0.09}Ga_{0.91}N$ (20 nm/20nm) superlattice. The samples were etched in a 0.23 M HCl solution with constant stirring. The etch profiles and corresponding band digrams are shown in Figure 5.8. The etching of the 300 nm thick InGaN layer was slow

and nonuniform, since there was little hole confinement (Figure 5.8a and d). In this layer, holes are likely to recombine without etching. In the InGaN/GaN superlattice (Figure 5.8b and e), the undercut is more visible, but the etch is still nonuniform. Finally, in the InGaN/InGaN superlattice (Figure 5.8c and f), etching was faster and more uniform. The InGaN/InGaN superlattice had the greatest hole confinement due to large piezoelectric fields.

### 5.2.3 Application of PEC liftoff to large-area flip-chip LEDs

An example of using PEC liftoff on *c*-plane InGaN LEDs was demonstrated to create large-area flip-chip LEDs and remove the freestanding GaN substrate [153]. The LED structures were grown by metalorganic chemical vapor deposition (MOCVD) on freestanding *c*-plane GaN substrates from Sciocs Company Limited with a threading dislocation density of approximately $4 \times 10^6$ cm$^{-2}$. The epitaxial structure for the flip-chip LEDs, shown in Figure 5.9(a), consisted of 1.5 µm *n*-GaN; a sacrificial layer with 6 multiple quantum wells (MQWs) with 2.5 nm InGaN wells and 7 nm GaN barriers with emission at 430 nm; a 3 µm *n*-GaN interlayer; an active region with 6 MQWs of 2.5 nm InGaN wells and 7 nm GaN barriers with emission at 440 nm; a 10 nm Mg-doped AlGaN electron blocking layer (EBL); a 110 nm Mg-doped $p^+$-GaN layer; and a 20 nm $p^{++}$-GaN contact layer. Test samples for characterizing the PEC undercut etch were also grown by MOCVD on freestanding *c*-plane GaN substrates. The epitaxial structure consisted of 1.5 µm *n*-GaN; a sacrificial layer with 6 MQWs with 2.5 nm InGaN wells and 7 nm GaN barriers with emission at 430 nm; a 110 nm Mg-doped $p^+$-GaN layer; and a 20 nm $p^{++}$-GaN contact layer.

The LED samples were processed into mesas that were defined using an inductively coupled plasma (ICP) dry etch. The total LED area was 0.1 mm$^2$. The etch went

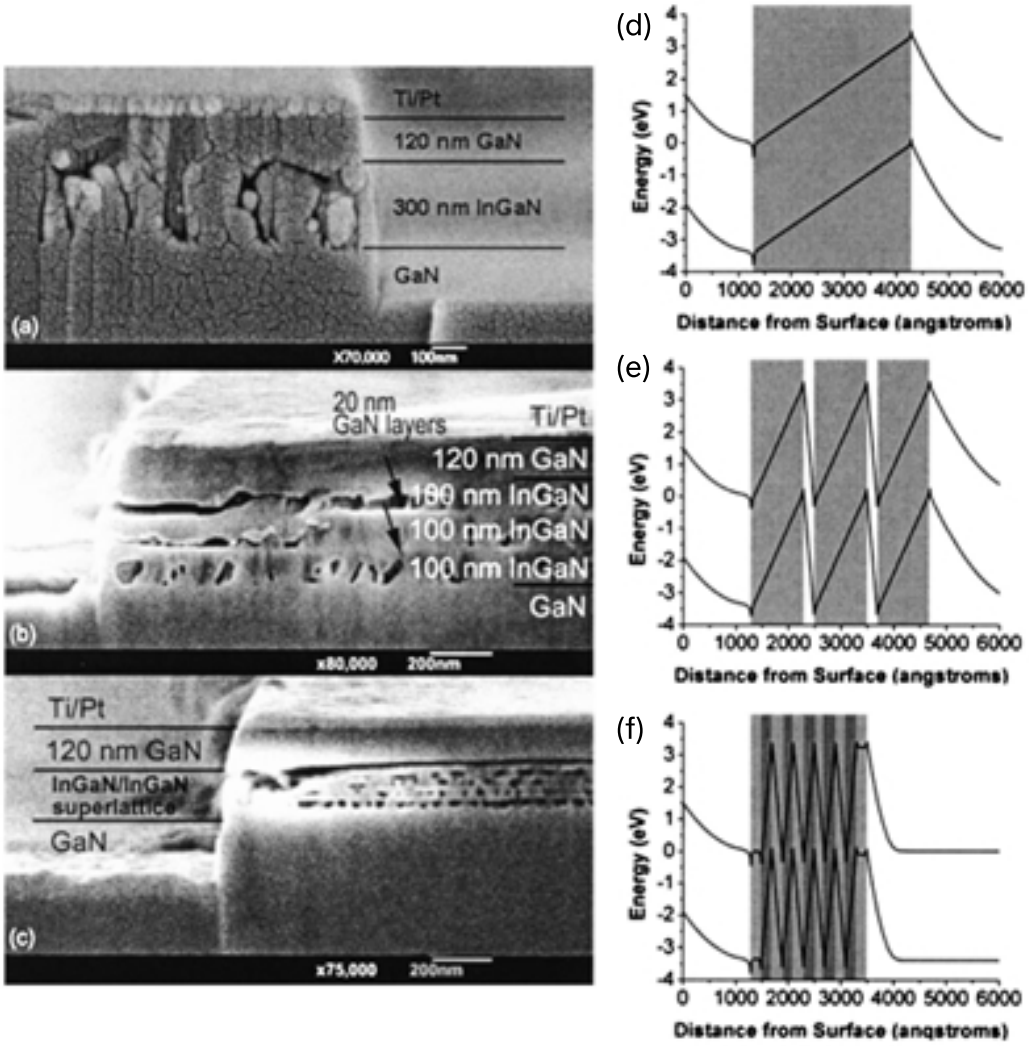


Figure 5.8: SEM cross section of (a) a 300 nm $In_{0.04}Ga_{0.96}N$ post (b) a 3 period $In_{0.04}Ga_{0.96}N$/GaN (100 nm/20 nm) superlattice, (c) and a 5.5 period $In_{0.04}Ga_{0.96}N/In_{0.09}Ga_{0.91}N$ (20 nm/20nm) superlattice. Band structures (d) of the structure in (a), (e) of the structure in (b), and (f) of the structure in (c). Reprinted from [E. D. Haberer, R. Sharma, A. R. Stonas, S. Nakamura, S. P. DenBaars, and E. L. Hu, *Appl. Phys. Lett.*, **85**, 762 (2004)] with the permission of AIP Publishing [174].

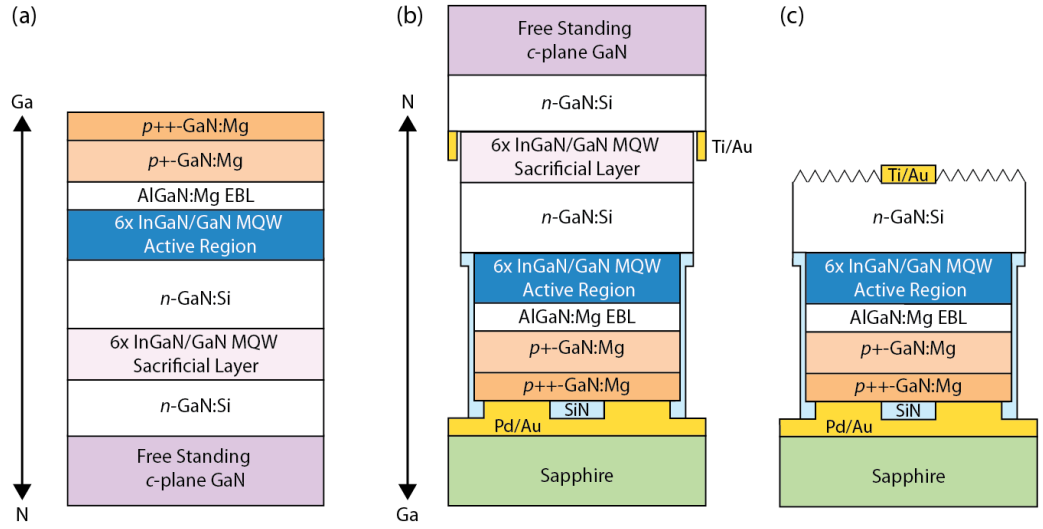


Figure 5.9: Cross-sectional schematic of (a) the as-grown epitaxial structure, (b) a partially processed sample after wafer-bonding and before PEC etching, and (c) a completely processed sample with $p$-GaN down and the N-face of $n$-GaN up. Figure from Hwang *et al.* [153].

through the active region MQWs and stopped in the $n$-GaN interlayer. 100 nm of $SiN_x$ were deposited using plasma-enhanced chemical vapor deposition (PECVD) to cover the sidewalls of the active region. A $p$-contact consisting of 50/500 nm Pd/Au was deposited by electron beam evaporation. This top Au layer also served as a bonding pad for subsequent flip-chip bonding. The sidewalls of the sacrificial MQWs were then exposed by a second dry etch right outside the first mesa. Finally, a cathode of 20/100 nm Ti/Au was deposited in the field outside the mesas to facilitate PEC etching. During PEC etching, this cathode served to extract electrons into solution. As illustrated in Figure 5.9, the sidewalls of the active region were protected by $SiN_x$, while the sidewalls of the sacrificial layer were exposed for PEC undercut etching.

A flip-chip submount was prepared by depositing 20/1000 nm of Ti/Au onto a sapphire wafer. This submount and the sample were etched in $O_2$ plasma at 300 torr and 100 W for 3 minutes to remove organic residue and prepare for flip-chip bonding. The

submount and sample were bonded using a flip-chip die bonder at a force of 300 N at 330°C for 1 minute, resulting in a bonded sample configuration shown in Figure 5.9(b). The bonded sample was placed in 1 M KOH with backside illumination for 5 hours for PEC undercut etching. The light source was an LED array emitting at 405 nm. This process resulted in the removal of the freestanding GaN substrate and the transfer of the LEDs to the submount. A final $n$-contact consisting of 20/1000 nm Ti/Au was deposited, resulting in the structure shown in Figure 5.9(c).

After $n$-contact deposition, LED 1 was examined by optical microscopy and scanning electron microscopy (SEM) and packaged without further roughening of the surface. LED 2 was intentionally roughened to improve light extraction. LED 2 was etched in heated KOH at 75°C with no illumination for 10 minutes, examined by optical microscopy and SEM, etched for another 15 minutes, examined again, and packaged. Packaging included dicing, mounting onto silver headers, wire-bonding, and encapsulating in silicone with a refractive index of 1.4.

The key components of the structure for PEC liftoff were the sacrificial MQWs and $n$-GaN interlayer. The undercut etch was carried out by electron-hole pairs that were photogenerated in the sacrificial MQWs by an above band-gap light source. Holes were confined in this $n$-$i$-$n$ structure and reacted with KOH to oxidize the sacrificial layer, which was then dissociated (and effectively etched) in KOH. Figure 5.10 illustrates the etch behavior of the sacrificial region. Bright-field optical and fluorescence images of the $n$-$i$-$n$-$p$ test samples described above were taken to show the time progression of the etch. Mesas were patterned on the test samples to expose the sacrificial layer. At the onset of the etch, the bright-field image showed an unetched mesa (Figure 5.10(a)), and the fluorescence image showed emission from the sacrificial layer (Figure 5.10(d)). As time progressed, the etch front proceeded to undercut the mesa, as shown in the bright-field images (Figure 5.10(b)-(c)). At corresponding areas in the fluorescence images (Figure

5.10(e)-(f)), the sacrificial region was black, indicating the MQWs had been etched.

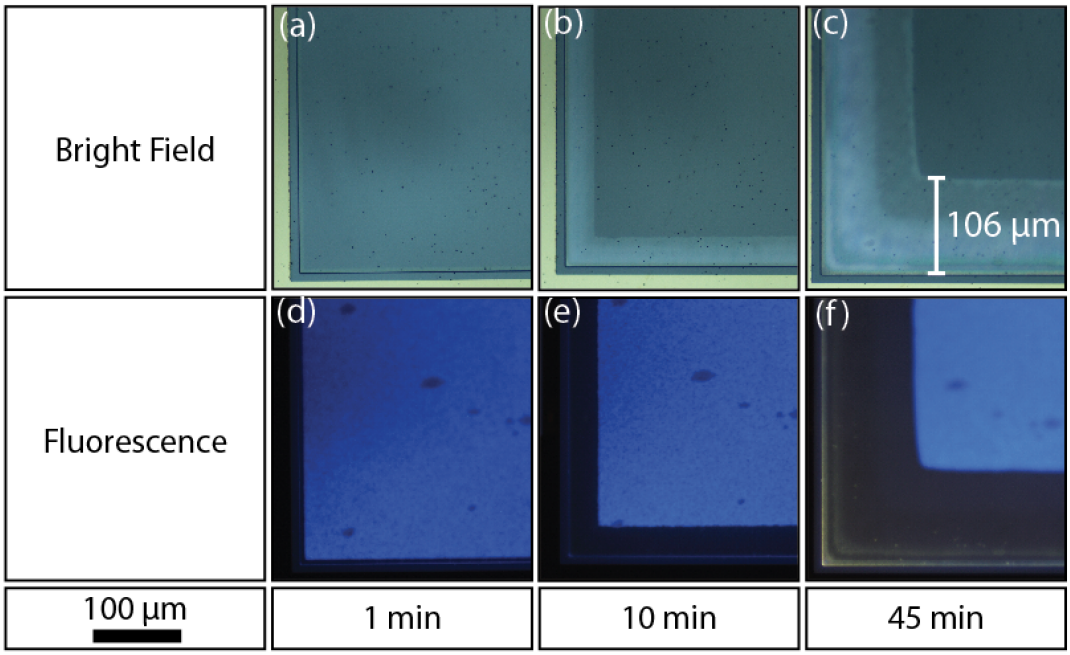


Figure 5.10: (a-c) Bright-field optical and (d-f) fluorescence images of mesa structures after 1 minute (a, d), 10 minutes (b, e), and 45 minutes (c, f) of PEC undercut etching in 1 M KOH with a 405 nm LED array. Figure from Hwang *et al.* [153].

As the lateral undercut proceeded, the N-face of the $n$-GaN interlayer was exposed to KOH and unintentional roughening occurred. The $n$-GaN interlayer was grown relatively thick (3 µm) to allow for this concurrent roughening. If the sample was left in solution for too long, the vertical roughening would have reached the active region and etched the MQWs.

The surfaces of the fabricated flip-chip LEDs were studied by SEM and optical microscopy. Figure 5.11(a) shows the effect of unintentional roughening on LED 1, which was not etched in heated KOH. The surface had sparsely distributed hexagonal pyramids with most feature sizes smaller than 200 nm. Figures 5.11(b) and 5.11(c) show the surfaces of LED 2 after 10 and 25 minutes of roughening in heated KOH, respectively. Compared with LED 1, LED 2 had more densely packed pyramids with most feature sizes

between 400 and 650 nm after 25 minutes. The percentage of flat area also decreased with longer immersion in KOH. For LED 1, about 70% of the area was flat. For LED 2, the percentage decreased from 30% with 10 minutes of roughening to 10% with 25 minutes of roughening. The effects of roughening can be seen in the optical micrographs in Figure 5.11(d)-(f), where the roughest sample appeared black because it effectively scattered the visible light from the microscope objective.

Previous studies [175] reported that the density of the pyramids was correlated with the TDD. Since the density of the pyramids for GaN grown on sapphire was on the same order as the threading dislocation densities (TDD), it was postulated that pyramids formed around dislocations. For this study, the TDD of the bulk GaN substrate was $10^6$ $cm^{-2}$, while the densities were $5.4 \times 10^8$ $cm^{-2}$, $3.6 \times 10^9$ $cm^{-2}$, and $1.0 \times 10^9$ $cm^{-2}$ for LED 1, LED 2 with 10 minutes of roughening, and LED 2 with 25 minutes of roughening, respectively. These densities indicate that the formation of the pyramids is not initiated

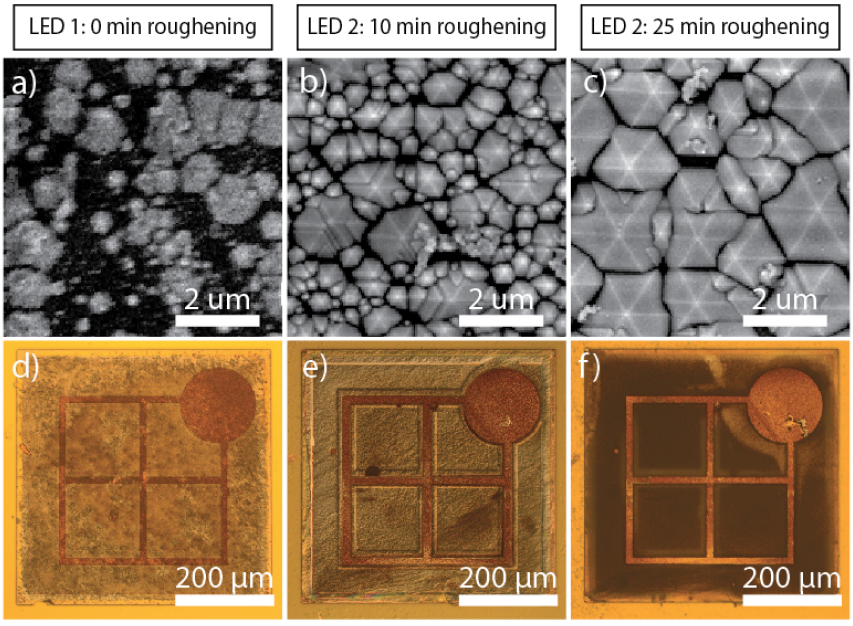


Figure 5.11: (a-c) SEM and (d-f) optical micrographs of the surfaces of LED 1 after 0 minutes of thermal roughening (a, d), LED 2 after 10 minutes of roughening (b, e), and LED 2 after 25 minutes of roughening (c, f). Figure from Hwang *et al.* [153].

solely by threading dislocations. This non-dislocation related etch behavior has also been reported previously [176].

Figure 5.12(a) shows the I-V curves for LEDs 1 and 2 after flip-chip processing. LED 1 had a turn-on voltage below 3.5 V. LED 2 had a higher turn-on voltage due to variations across the wafer from growth. The I-V curve of LED 2 was comparable before and after processing. The peak emission wavelength of both LEDs was around 432 nm with a full-width half max (FWHM) of 15 nm (Figure 5.12(b)). The effects of roughening on LED performance are shown in Figure 5.12(c)-(d). The LEDs had areas of 0.1 $mm^2$, so 1 mA corresponded to a current density of 1 $A/cm^2$. At the peak EQE (at a current density of 36 $A/cm^2$), the output power and EQE were 10.3 mW and 9.9%, respectively, for LED 1 and 14.6 mW and 14.1%, respectively for LED 2. Roughening resulted in a 42% improvement in output power and EQE.

Although this work proved the feasibility of using PEC liftoff for creating TFFC LEDs from epitaxial layers grown on freestanding c-plane GaN substrates, there are several changes that could be made to improve device performance. Incorporating a Ag-based *p*-contact would significantly improve the extraction efficiency, as the Pd/Au *p*-contact that was used above had a relatively low reflectivity. Ray tracing simulations show at least a 3x improvement in the extraction efficiency when using a Ag-based *p*-contact instead of a Pd/Au *p*-contact. Using a SiC submount instead of sapphire would improve heat extraction due to its higher thermal conductivity.

## 5.3 PEC liftoff enabled mass transfer

PEC liftoff was applied as the release method to RGB µLEDs grown on different substrates, and transfer was achieved by transfer printing with a PDMS stamp. RGB µLEDs were grown, fabricated, and transfer printed onto a single substrate. Blue epitaxy was

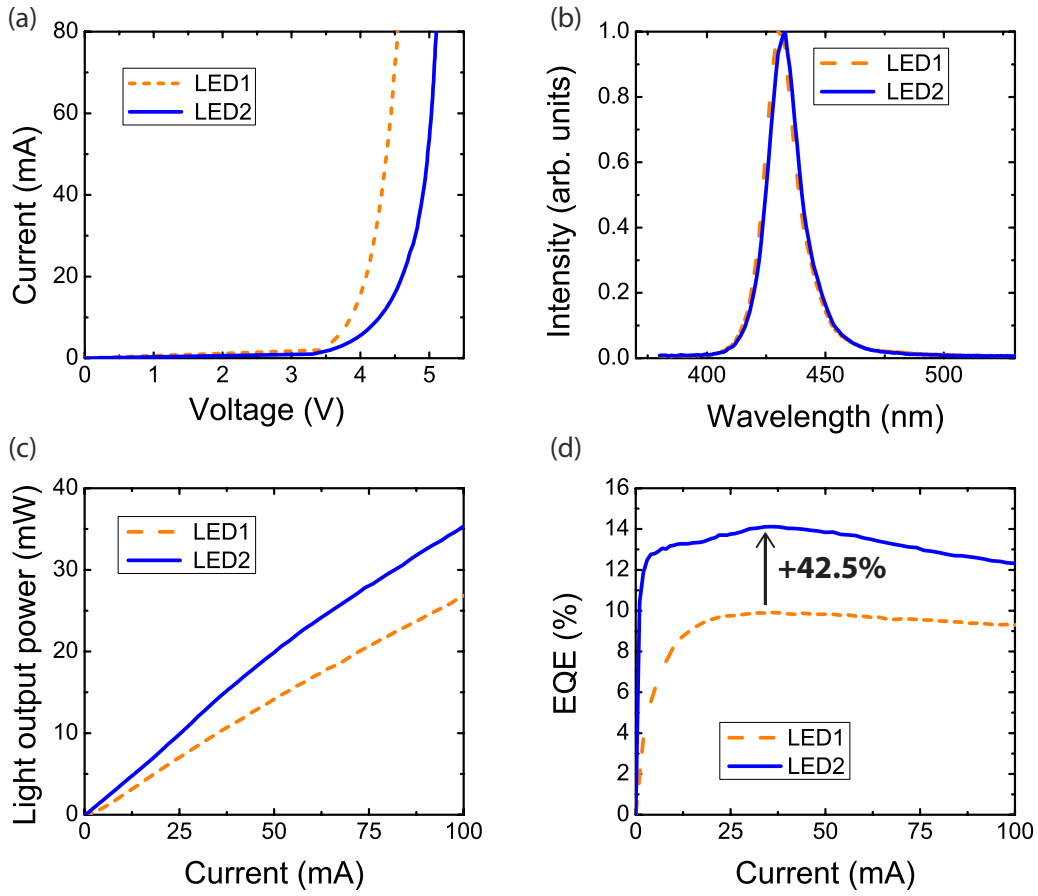


Figure 5.12: (a) I-V curve for LEDs 1 and 2 after flip-chip processing. 1 mA of current corresponds to a current density of 1 A/cm$^2$. (b) Electroluminescence spectra showing a peak wavelength around 432 nm with a FWHM of 15 nm. (c) Dependence of light output power on current. (d) Dependence of EQE on current. An improvement of 42.5% is seen in output power and EQE with roughening. Figure from Hwang *et al.* [153].

grown on $c$-plane, green on freestanding $(20\bar{2}1)$ semipolar GaN (15° inclined from $m$-plane), and red on freestanding $(11\bar{2}2)$ semipolar GaN (32° inclined from $m$-plane). As mentioned in Section 5.2, PEC undercut requires a sacrificial layer that has a bandgap below that of the light source. In this work, InGaN/GaN MQWs that emit between 405 and 420 nm are used.

### 5.3.1 MOCVD growth

For $c$-plane GaN (blue epitaxy), while the lateral PEC etch is proceeding, the KOH will also vertically roughen the N-face of $n$-GaN. Thus, a thick (2-3 µm) interlayer of $n$-GaN must be grown, or else the vertical roughening may etch away the active region MQWs. Such a thick structure requires precise control of the morphology, or the LED epitaxy will be dotted with V-defects. Figure 5.13 shows examples of unoptimized epitaxy that leads to undesired surfaces. If these V-defects originate from the sacrificial MQWs and propagate to the $p$-GaN, shorting becomes an issue. When the $p$-metal is deposited on the $p$-GaN surface, the metal could follow the V-defect down to the $n$-GaN and cause a short path that bypasses the MQWs (e.g. no light is emitted). To smoothen out the morphology, the V-defects must be closed as soon as they appear, or they will continue to grow.

V-defects on $c$-plane GaN arise from different growth conditions when growing InGaN versus GaN [177]. A cross-section of a V-defect is shown in Figure 5.14. InGaN is grown at a lower temperature than GaN (700 to 900°C compared with 1000 to 1200°C), so the surface diffusion of indium is limited, and the defect morphology is kinetically governed. The dark gray layers of Figure 5.14 are InGaN quantum wells, and the thicker white layers are the GaN barriers. During the growth, the growth rate of the GaN was different in the V-defect than outside of the defect (the GaN layer is much thinner

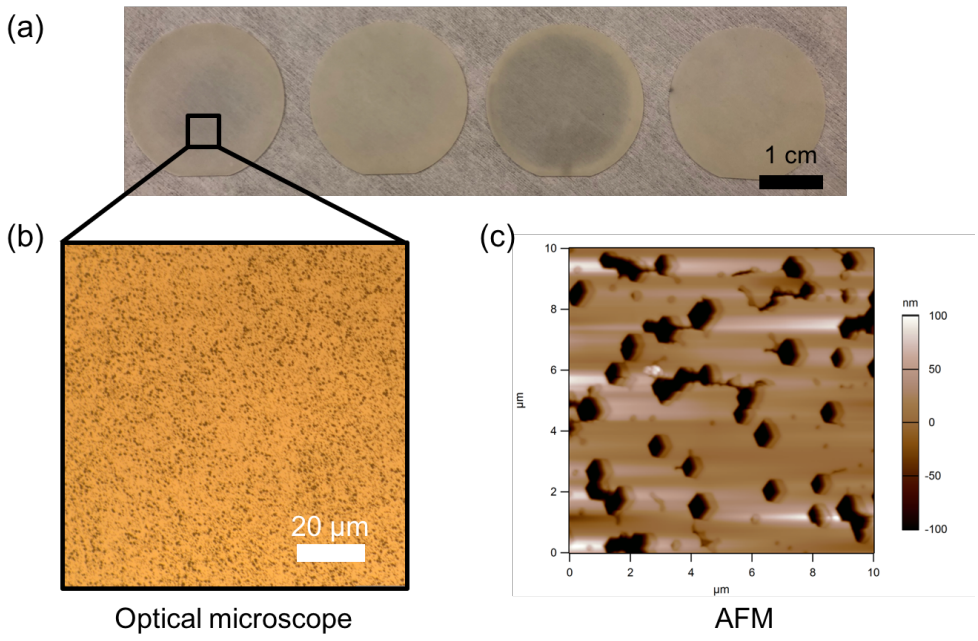


Figure 5.13: Undesired morphologies of *c*-plane InGaN/GaN growth shown by (a) optical photograph, (b) optical micrograph, and (c) atomic force microscope.

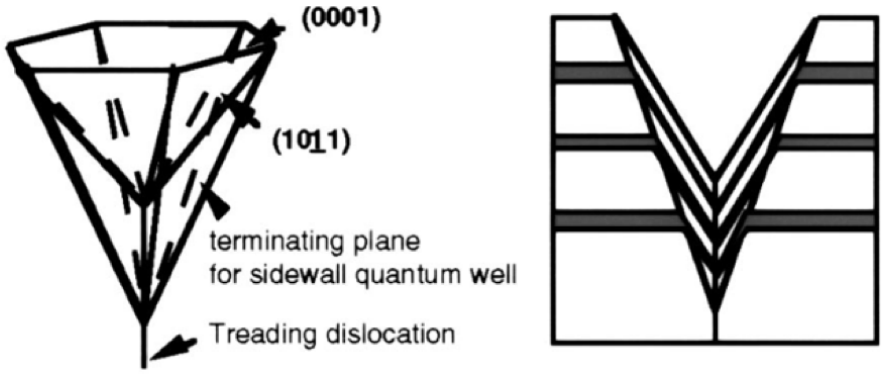


Figure 5.14: Cross-sectional schematic of a V-defect. Reprinted from [X. H. Wu, C. R. Elsass, A. Abare, M. Mack, S. Keller, P. M. Petroff, S. P. DenBaars, and J. S. Speck, *Appl. Phys. Lett.*, **72**, 692 (1998)] with the permission of AIP Publishing [177]

inside the V-defect) and caused pit-like morphology. To close the pits and smooth out the morphology, the surface mobility of Ga adatoms must be increased while growing the quantum barrier. Changes to the growth conditions that will increase the surface mobility include increasing the growth temperature (giving the atoms more energy to diffuse), decreasing the V/III ratio (the ratio of N atoms to Ga atoms), decreasing the growth rate (giving the atoms more time to diffuse and fill in the defect), and/or changing the carrier gas to hydrogen. When increasing the growth temperature, care must be taken to protect the quantum wells. If the temperature is ramped directly after growing the quantum well, indium may desorb from the surface or diffuse through other layers, lowering the final emission wavelength and intensity. To protect the wells, a thin (2-5 nm) GaN barrier/cap should be grown at the same temperature before ramping the temperature. For the high temperature barrier, the carrier gas may also be switched to hydrogen to help planarize the surface (the quantum wells should be grown in nitrogen or else the indium will be etched away). Figure 5.15 shows the structure, smooth morphologies are of the growth, and evidence of the intact quantum wells provided by photoluminescence.

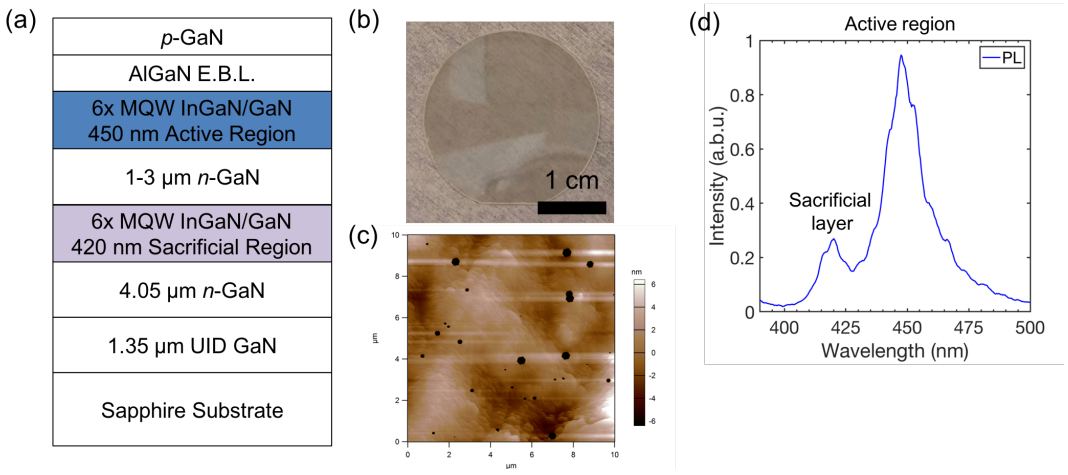


Figure 5.15: PEC LED growth (for *c*-plane on sapphire): (a) Cross-sectional schematic of the epitaxy, (b) optical photograph image of the smooth surface, (c) $10 \times 10$ µm$^2$ AFM scan of the surface, and (d) photoluminescence of the two MQWs.

Above the sacrificial quantum wells were the active regions. For the blue ($\sim$ 441 nm) $c$-plane µLEDs grown on sapphire, 6-period MQWs were grown at a temperature between 850-900°C (the same epitaxy as that detailed in Chapter 2). For green ($\sim$ 529 nm) and red ($\sim$ 641 nm) epitaxy, freestanding semipolar GaN substrates were used ($(20\bar{2}1)$ and $(11\bar{2}2)$, respectively). The active regions were both 2-3 nm thick single quantum wells grown at temperatures between 750-800°C. Although the wavelength of the red epitaxy was over 100 nm greater than that of the green epitaxy, the growth temperature of the InGaN quantum well was similar. In general, planes that have greater inclination angles from $m$-plane exhibit longer wavelength emission (although many other growth issues come into play) [39, 40]. Thus, epitaxy grown on $(11\bar{2}2)$ displayed higher electroluminescence wavelengths than that grown on $(20\bar{2}1)$ even though the growth temperatures were similar.

### 5.3.2 Nanofabrication design: requirements and design rules

The end result of the fabrication is to have patterned µLEDs that are ready to be undercut but still anchored to the wafer through some breakable features. The µLEDs will emit light down through the substrate with $n$- and $p$-metals on the top surface. The areas to be undercut should have the full LED epitaxy ($n$-GaN, active region MQWs, EBL, and $p$-GaN). In order to PEC etch and transfer print, the final processed device needs to have the following features: exposed sacrificial wells to allow for KOH to contact the wells for PEC etching; anchors to hold the µLEDs onto the sample during PEC liftoff so they do not float away in solution; thin structures that can be snapped off mechanically; dielectric to protect the active region wells from being etched and to cover sacrificial wells in areas that are not supposed to be etched; a PEC metal contact to faciliate PEC etching; and $p$- and $n$-contacts. Furthermore, all the materials need to be chemically

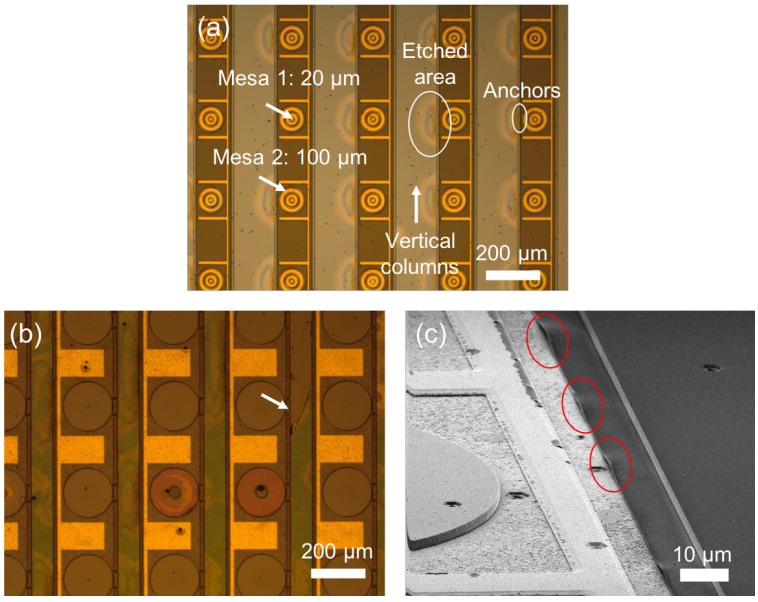


Figure 5.16: (a) Optical micrograph of PEC etched devices showing the 20 µm wide µLED, the 100 µm mesa, and PEC etching of the vertical columns through the thin anchors. (b) Optical micrograph of broken dielectric (highlighted with the white arrow) and (c) SEM image of areas with lifted dielectric through which KOH may seep (circled in red).

resistant to KOH and compatible with prolonged exposure to UV light.

The processing of this epitaxy is similar to the µLED processing of Chapter 2 but with the added steps described above and more stringent design rules. The first three lithographies are to: (1) etch the first mesa to expose the active region MQWs and define the µLED area; (2) etch the second mesa to expose the sacrificial MQWs and pattern the anchors to hold the µLEDs to substrate; and (3) deposit a dielectric to protect the active region MQWs and the sacrificial MQWs at the anchors. The first lithography and mesa etch are straightforward, but careful attention should be paid to the design of the second mesa etch. Figure 5.16(a) shows that the width of the first mesa is 20 µm (for a 20 µm diameter µLED), but the *n*-GaN circle on which the µLED sits is 100 µm (this extra area is for metal contacts and testing purposes; in a final manufacturing design, this circle may be much smaller). The total PEC undercut width is thus 100 µm (or 50

µm, since the etch will proceed from all directions). Although the dielectric will cover the columns (shown vertically in Figure 5.16(a)), the KOH will seep through the two thin anchors connecting the µLEDs to the columns (see the cloud-like patterns in Figure 5.16(a)). Therefore, the width of the columns should be at least 1.5x the width of the *n*-GaN mesa to ensure the column is not fully etched. In addition to the geometry of the patterns, the deposition of the dielectric must be characterized properly. If the stress of the dielectric is tensile, there may be areas where the dielectric lifts up or even breaks off as shown in Figure 5.16(b)-(c). Consequently, KOH will also etch these exposed areas, and the µLEDs will no longer be anchored.

After the third lithography and dielectric deposition, a number of routes are available to complete the processing with varying degrees of practicality and feasibility (shown in Figure 5.17). Each route has its own limitations regarding compatibility with PEC etching and are described herein. The first method is to deposit all the metals (PEC, *p*-, *n*-contacts) before PEC etching. With this method, any lithography and processing post-PEC etch and post-transfer printing is minimized. Processing prior to the undercut and transfer relaxes any tight alignment tolerances that are required. However, this exposes the metal contacts to KOH, so the metal must be chemically resistant. Aluminum was used in the standard µLED processing of Chapter 2, but Al is easily etched away in KOH so alternative contacts must be used. A second method is similar to the first but with an additional step of protecting the metal from KOH exposure with a dielectric like silicon nitride. In this case, the tight restriction of metals is relaxed and Al may be used again. A drawback of this method is the removal of the dielectric. In addition to the dielectric that protects the metal from KOH, there are also dielectrics already on the µLED (for instance, the dielectric that passivates the sidewall and electrically insulates the *p*- and *n*-GaN). Removing the dielectric that protects the metal would also strip the other dielectrics that are necessary for the µLED.

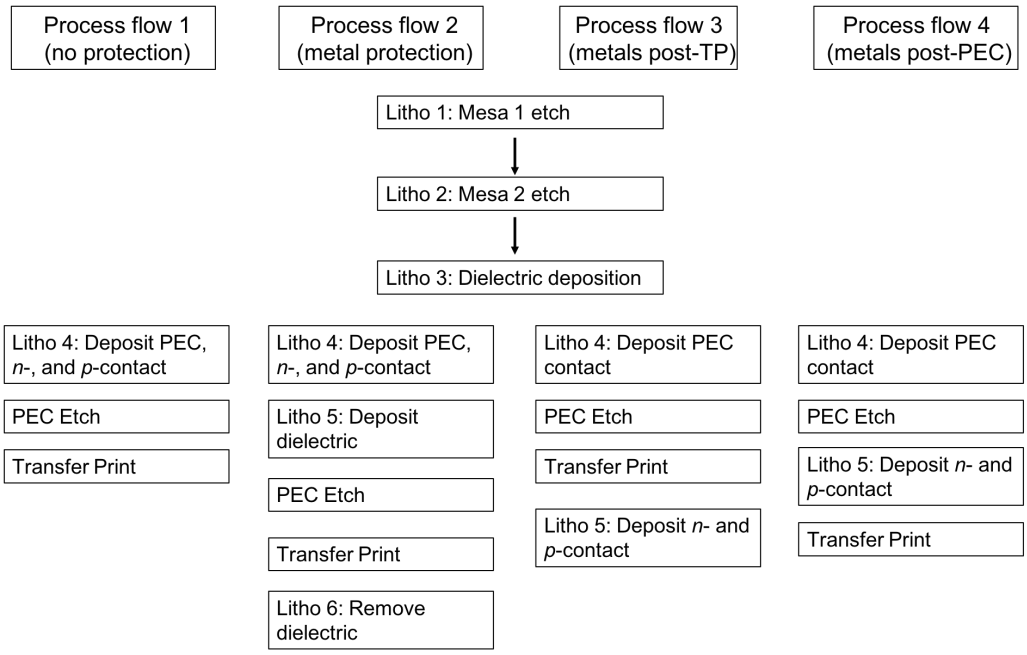


Figure 5.17: Process flow options for the PEC liftoff enabled mass transfer.

A third method is to deposit the $p$- and $n$- metals after transfer printing. Any metals may be used (e.g. silver, if a mirror wanted to be incorporated), but there are a few potential problems. The biggest issue is that once the µLEDs have been transferred, their alignment and periodicity may be perturbed. In this case, it would be difficult or impossible to accurately deposit the metals. In addition, although PEC etching does not significantly etch GaN, the top surface of the $p$-GaN may be roughened. This roughness may affect adhesion or contact resistance of the $p$-contact. Instead of depositing metals after transferring, a fourth method would be to deposit the $p$- and $n$- metals after PEC etching but before transfer printing. With the µLEDs still on the sample, the periodicity of the patterns remains. However, the µLEDs are now a lot more physically fragile as they are only held by two thin anchors. Any mechanical disturbance to the µLEDs (e.g. sonication of the samples in solvent (which is done during solvent cleaning), depositing photoresist and spinning the sample, or metal liftoff) may cause the anchors to break off

and the µLEDs to float away in solution.

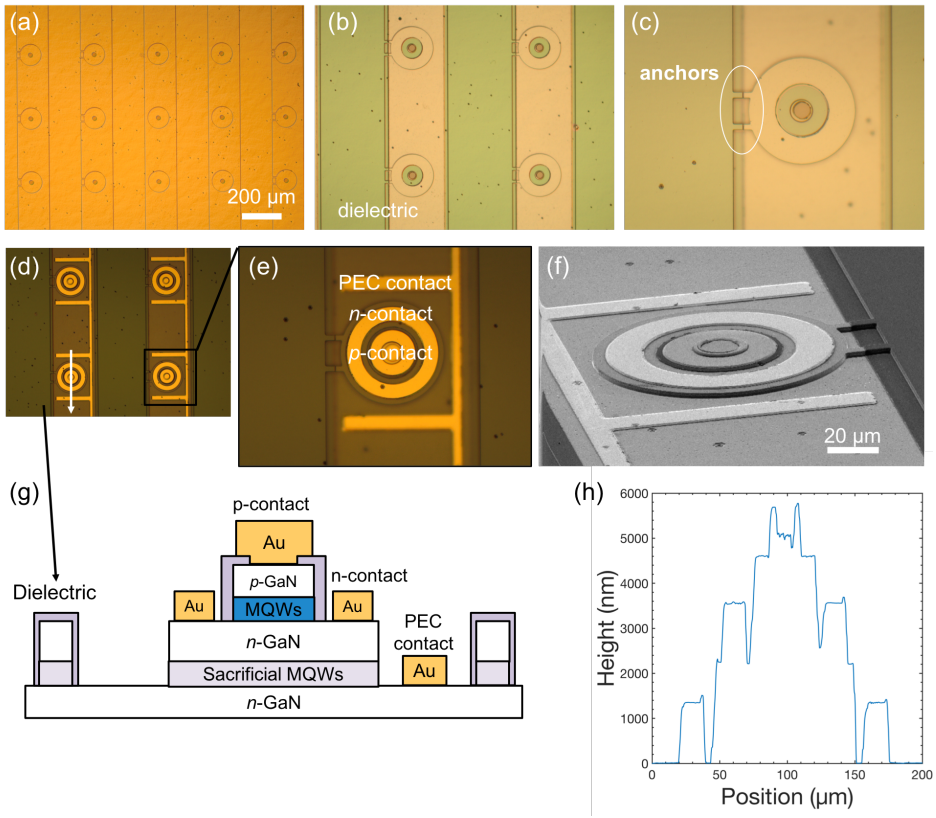


Figure 5.18: Process overview: Optical micrograph of (a) mesa 1 and 2 etches, (b) dielectric deposition on the vertical columns (appears green in the image), (c) magnified image of µLED with dielectric, (d) final device structure of µLEDs that are ready to be released from the substrate, and (e) magnified optical micrograph. (f) SEM image of the µLED, (g) cross-sectional schematic of the processed device, and (h) Depth profile of the µLED taken across the white arrow in (d).

Considering the advantages and disadvantage of each route, the first option made most sense to test the PEC etch and transfer print process. Although the contact metals may be affected by KOH, the limitations of the other methods (loss of periodicity, physical instability, etc) would have added unnecessary troubleshooting when trying to make a proof of concept. Figure 5.18 details the process flow. 40 nm of heated indium tin oxide was blanket deposited. Then, circular mesas were patterned by etching through the ITO with a reactive ion etch (RIE) chemistry of methane, hydrogen, and argon (4/20/10 sccm

of MHA at 75 mTorr with a bias of 370V) and through to the $n$-GaN with a RIE etch using $Cl_2$. The total etch depth was about 1.1 µm. A second mesa etch was done with a 2.2 µm RIE etch. The first etch stopped at the $n$-GaN interlayer, and the second etch went down to the bottom $n$-GaN layer to expose the sidewalls of the sacrificial MQWs (Figure 5.18(a)). Next, dielectric was deposited by ion beam deposition (IBD) to cover the columns and to passivate the sidewalls of the µLEDs. Either 500 nm of SiN or the omnidirectional reflector detailed in Chapter 2 (a seven layer alternating stack of $SiO_2$ and $Ta_2O_5$ capped with $Al_2O_3$) may be used as the dielectric (Figure 5.18(b)-(c)). Finally, a common PEC, $n$-, and $p$-contact of 20 nm Ti/1000 nm Au was deposited. Figure 5.18(d)-(f) shows the 20 µm diameter µLED covered with Ti/Au and an annular $n$-contact atop the $n$-GaN. Figure 5.18(g)-(h) shows the cross-section and height profile of a µLED.

### 5.3.3 PEC liftoff

Figure 5.19(a) shows the PEC etch station. A 405 nm LED array (spectrum in Figure 5.19(b)) emitted light, which was focused through a magnifying lens, onto the µLEDs in 0.5M KOH at room temperature. The power density of the LED array was 8.68 mW/cm$^2$. Other sources may be used, such as a 405 nm laser diode. Considerations

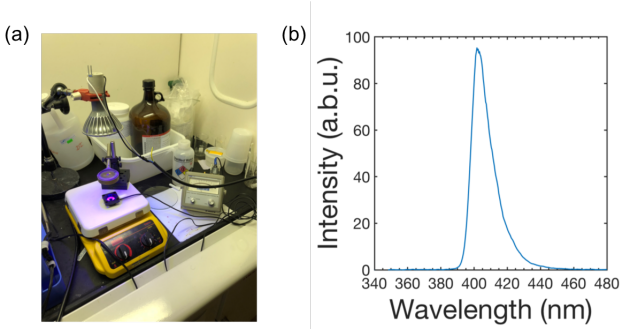


Figure 5.19: (a) Optical photograph of the PEC setup and (b) photoluminescence spectrum of 405 nm LED array.

in choosing a source include the power density and the emission profile. High power densities increase the generation rate of electrons and holes in the sacrificial layer, but the etch rate saturates above a certain power density [173]. The emission profile, or spot size, also affects the uniformity of the etch as the intensity (and carrier generation) will vary across the sample. Laser diodes have much smaller spot sizes than LED arrays but have higher power densities. Optimization of the etch rate may be done to balance the two competing effects.

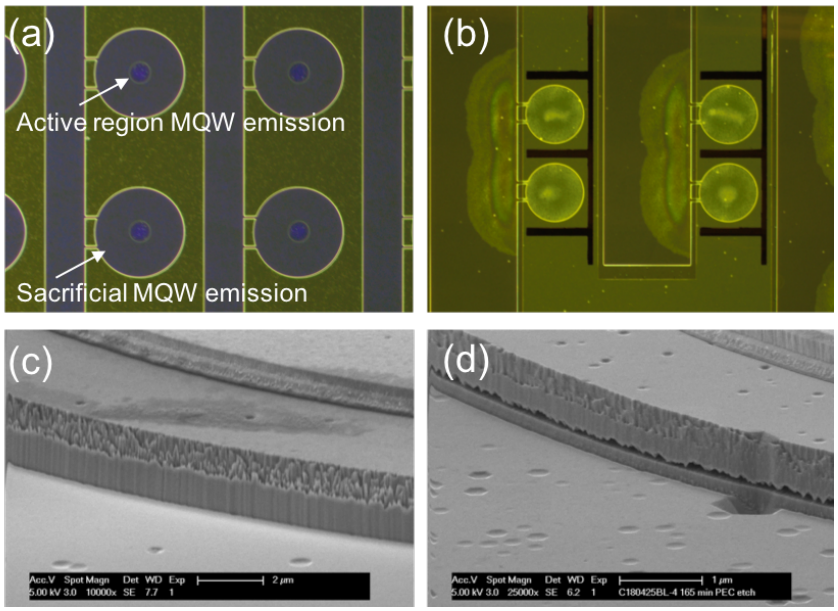


Figure 5.20: Fluorescence images of (a) the *c*-plane µLEDs before PEC etching in 0.5M KOH and (b) test structures on the same sample after 165 minutes of PEC etching. SEM images of the mesa sidewall (c) before and (d) after the etch showing the sacrificial layer.

After 165 minutes of PEC etching, the sacrificial MQWs were etched through. Before the etch, fluorescence from the sacrificial MQWs may be seen in Figure 5.20(a). After the etch was completed, those sacrificial MQWs were etched through and only the yellow fluorescence of the GaN remained in the test structures shown in Figure 5.20(b). SEM images before and after the PEC etch in Figure 5.20(c)-(d) show the formation of hexagonal pyramids on the N-face of the *n*-GaN as a result of exposure to KOH. For the

semipolar samples, the interface was much flatter as there was little to no roughening. Once the PEC etch was done, there was an air gap between the $n$-GaN of the LED and the $n$-GaN below the sacrificial MQWs except at the vertical columns. The µLEDs were released from the substrate and ready to be transfer printed.

### 5.3.4 Transfer printing of µLEDs

To transfer the µLEDs, an elastomeric stamp was used. This stamp was made out of PDMS and could be used as a temporary substrate for the µLEDs. To make the stamp, the PDMS base was mixed with a curing agent (10:1 ratio of base to curing agent) and poured onto a flat surface (such as a silicon wafer or a plastic petri dish). The PDMS was cured at room temperature for 16 hours and then at 65°C for one hour. To make a handle for the PDMS, glass slides were cleaned in acetone, isopropyl alcohol, and deionized water. The glass slide surface was treated in a UV ozone photoreactor for 10 minutes to increase the hydrophilicity of the glass surface and promote adhesion to the PDMS. The PDMS was then cut into a trapezoidal prism as shown in Figure 5.21. The

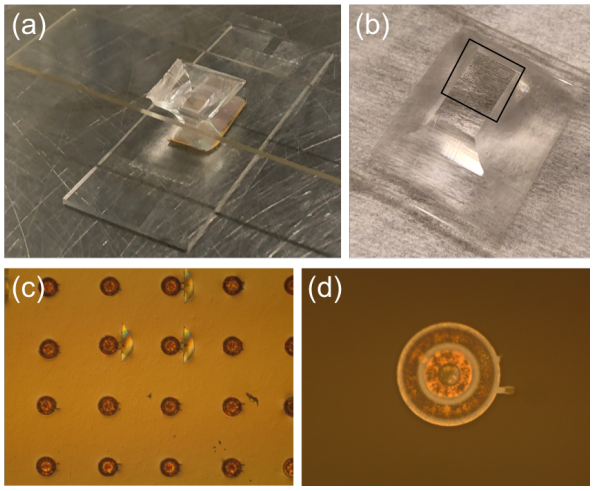


Figure 5.21: Images of (a) µLEDs sandwiched between the growth substrate and PDMS, (b) µLEDs transferred to PDMS. (c)-(d) Optical micrographs of µLEDs transferred to PDMS.

PDMS stamp was slowly lowered onto the µLED surface and left on the sample for five to ten minutes to allow the surface of the PDMS to wet the µLEDs. One end of the glass slide was quickly pushed down to mechanically break off the anchors of the µLEDs and transfer them to the PDMS. Figure 5.21(b)-(d) shows the µLEDs on the surface of the PDMS.

Once the µLEDs were on the PDMS, they must be transferred to a final substrate. In this case, the µLEDs were transferred to a glass slide. The glass slide was also cleaned in solvent and treated in with UV ozone. In order to transfer the µLEDs, an adhesion layer, Norland NOA61, was deposited on the glass slide. NOA61 is a clear, polyurethane based photopolymer that cures (and crosslinks) under UV light and has a refractive index of 1.56. NOA61 was spin-coated onto a glass slide at 2000 rpm for one minute. The PDMS stamp (with the µLEDs) was slowly lowered onto the NOA61-coated glass slide as shown in Figure 5.22(a) until the NOA61 wetted the µLEDs. Once stable, a UV-A lamp was used to cure the NOA61 for 1.5 hours. Once the cure was done, the NOA61 was hardened and bonded to the µLED. This bond was stronger than the bond between the µLEDs and the PDMS stamp, so the PDMS stamp could be slowly peeled off the µLEDs until the µLEDs were transferred to the glass substrate (Figure 5.22(b)-(c)).

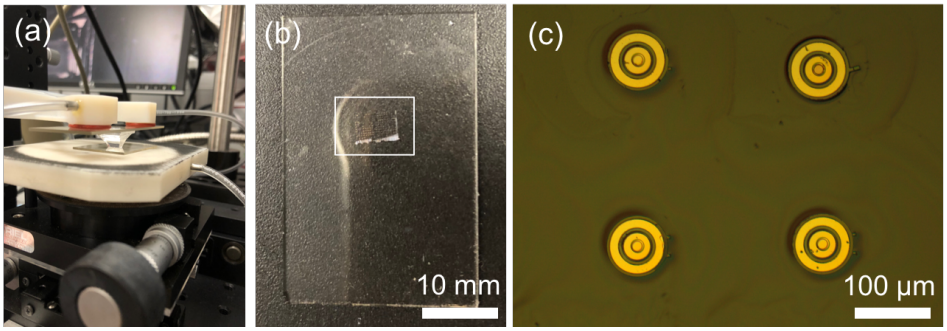


Figure 5.22: Images of (a) µLEDs sandwiched between PDMS and a glass substrate, (b) µLEDs transferred to a glass substrate. (c) Optical micrographs of µLEDs transferred to a glass substrate.

### 5.3.5 Optoelectronic results

After processing (before PEC etching and transfer printing), on-wafer measurements were taken to collect current density versus voltage characteristics as well as wavelength spectra. Figure 5.23(a)-(c) displays the red, green, and blue µLEDs on their native growth substrate. The J-V characteristics in Figure 5.23(d) indicated optimization of the semipolar growths were needed. Low voltage ($<$ 3 V at 20 A/cm$^2$) green devices on (20$\bar{2}$1) without the sacrificial layer below had been fabricated previously, but the *p*-GaN contact growth conditions needed to be optimized. The growths of these semipolar

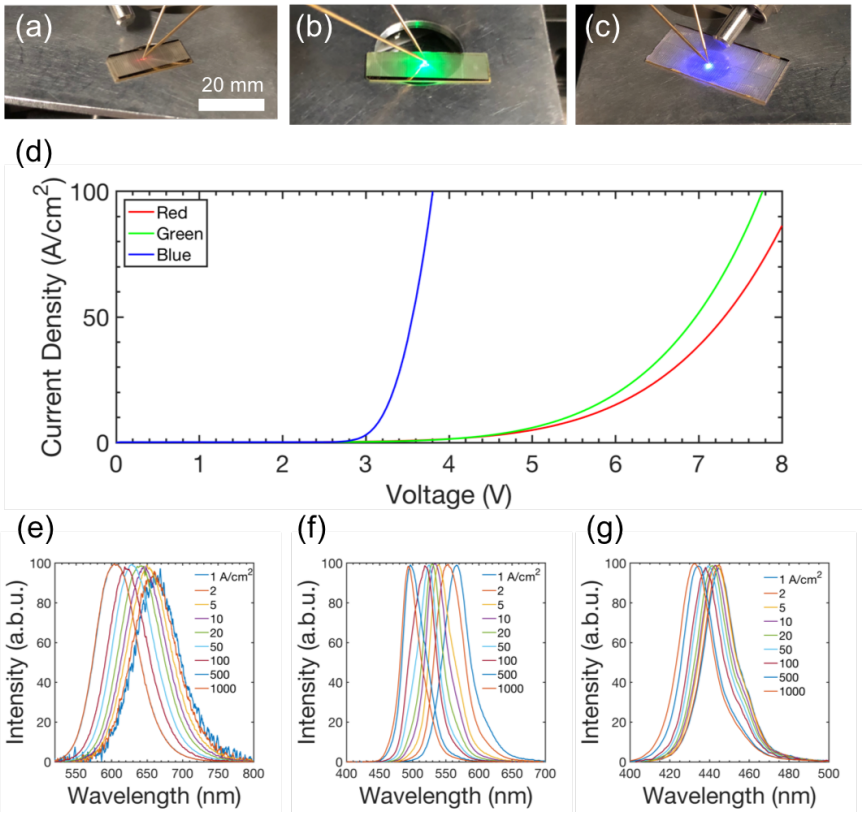


Figure 5.23: µLED characteristics on-wafer (before PEC etching): Optical photographs of the (a) red, (b) green, and (c) blue µLEDs; (d) current density versus voltage characteristics; and wavelength spectrum at various current densities for the (e) red, (f) green, and (g) blue µLEDs.

devices is outside the scope of this thesis. The wavelength shift of these µLEDs due to the quantum-confined Stark effect (QCSE) is illustrated in Figure 5.23(e)-(f). The peak wavelength of the blue µLED had the least shift of 22 nm from 1 A/cm$^2$ to 1000 A/cm$^2$. Both the green and red µLEDs had significant shifts of 74 nm and 59 nm, respectively, over the same current density range. The semipolar $(20\bar{2}\bar{1})$ plane has a much more stable wavelength (compared with $(20\bar{2}1)$ and $(11\bar{2}2)$), but there are growth issues associated with growing higher indium compositions, such as black triangular defects [178].

Throughout the PEC etch and transfer process, the µLEDs were tested to measure current versus voltage and voltage versus light output power characteristics. Measurements were taken after fabrication and before PEC etching; after PEC etching; and after transferring to glass. Figure 5.24 shows the blue µLEDs were transferred intactly from sapphire to a PDMS temporary substrate to a final glass substrate. The J-V characteristics indicated that the voltage and series resistance remained low throughout the

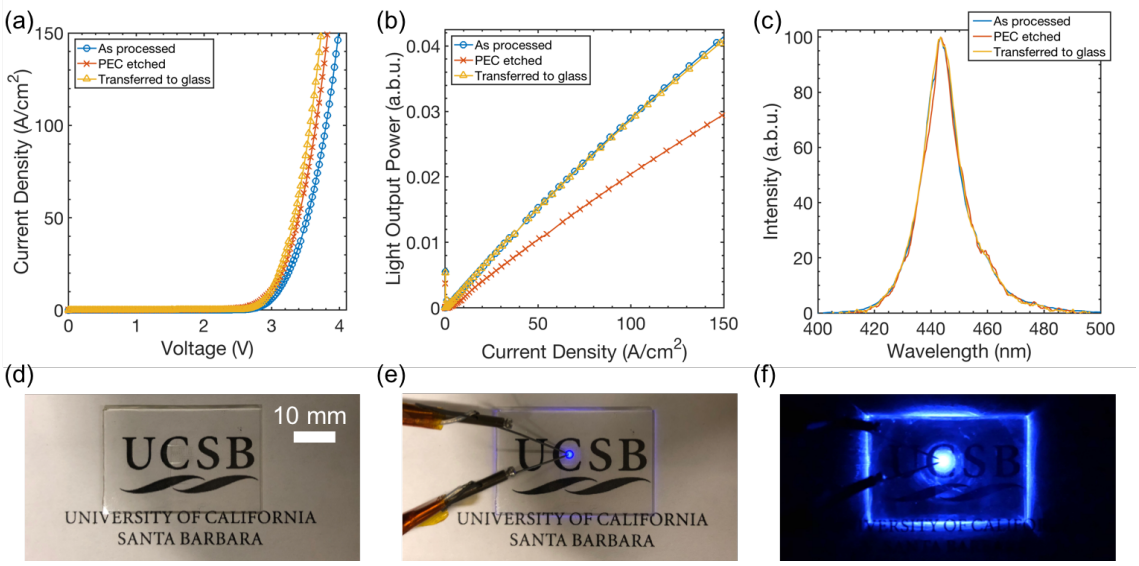


Figure 5.24: Blue µLED characteristics on-wafer, after PEC etching, and after transfer printing to glass: (a) Current density versus voltage characteristics, (b) light output power versus current density, (c) wavelength spectrum, and (d)-(f) optical photographs of µLED on glass displaying the transparency (scale bar is the same in (d)-(f)).

process. One of the earlier concerns with this process was that the exposure of the $p$- and $n$-metals to KOH would affect the conductivity of the metals, but the J-V curves suggested the contacts were still robust. The quality of the quantum wells and light emission was retained throughout this process as shown in Figure 5.24(b)-(c). The light output power behavior was the same before and after transferring the µLEDs. The drop in power after PEC etching (orange curve marked with 'x's) was due to the air gap that was introduced between the quantum wells and the sapphire substrate. This air gap induced reflection at the $n$-GaN/air interface and the air/sapphire interface. However, the light output power was recovered when that air gap was removed and the µLEDs were transferred to the NOA61-coated glass substrate. The peak wavelength and full-width at half-max (FWHM) also remained the same at 443 nm and 14 nm, respectively.

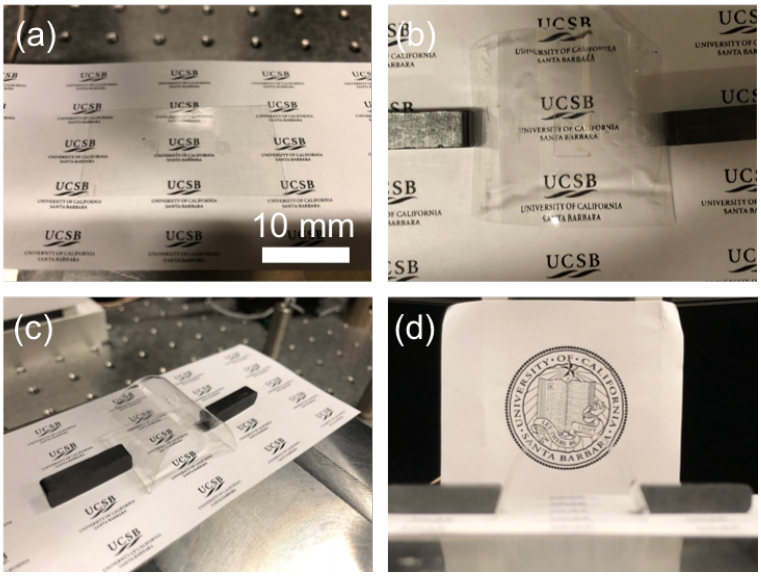


Figure 5.25: Optical photographs of µLEDs on acrylic (not turned on) demonstrating the (a) transparency and (b)-(d) flexibility. The acrylic substrate is 46.5mm × 23.5mm.

With this method, µLEDs may be transferred to a wide range of substrates, such as acrylic (Figure 5.25). The limitation lies in the adhesion between the desired substrate and the adhesion layer (NOA61 in this case). The adhesive is spin-coated and needs to

create a uniform layer across the substrate so that the μLEDs will be seated properly on the substrate. If there are adhesion issues, surface cleaning of the substrate (such as solvent cleaning, UV ozone treatment, and/or annealing) or even choosing different NOA products may improve the adhesive properties.

Figure 5.26 demonstrates the versatility of the method and its applicability to different growth substrates. Red, green, and blue μLEDs were transferred onto the acrylic from $(11\bar{2}2)$ GaN, $(20\bar{2}1)$ GaN, and $c$-plane sapphire, respectively. The μLEDs may be electrically turned on while the substrate was flat (Figure 5.26(a)-(f)) and when bent (Figure 5.26(g)-(i)) without degradation. The optoelectronic characteristics remained similar to those in Figure 5.23. Furthermore, Figure 5.27(a)-(c) demonstrates that μLEDs of all three colors were on the same substrate, while the wavelengths of the μLEDs at 20 A/cm$^2$ are shown in Figure 5.27(d). This ability to transfer onto the same substrate is vital for making full-color displays. Monolithic displays do not require mass transfer and are thus much simpler to fabricate. This PEC liftoff method allows for release of μLEDs from both sapphire and freestanding GaN substrates. Sapphire is the main workhorse of the LED industry and will still dominate the InGaN market for the foreseeable future. However, given its unique advantages of reduced polarization and longer wavelength emission, freestanding GaN may emerge as the substrate of choice for green (and even red) μLEDs. As there is currently no proven technology for release of μLEDs from freestanding GaN, the process invented in this chapter may prove to be significant for future display technologies.

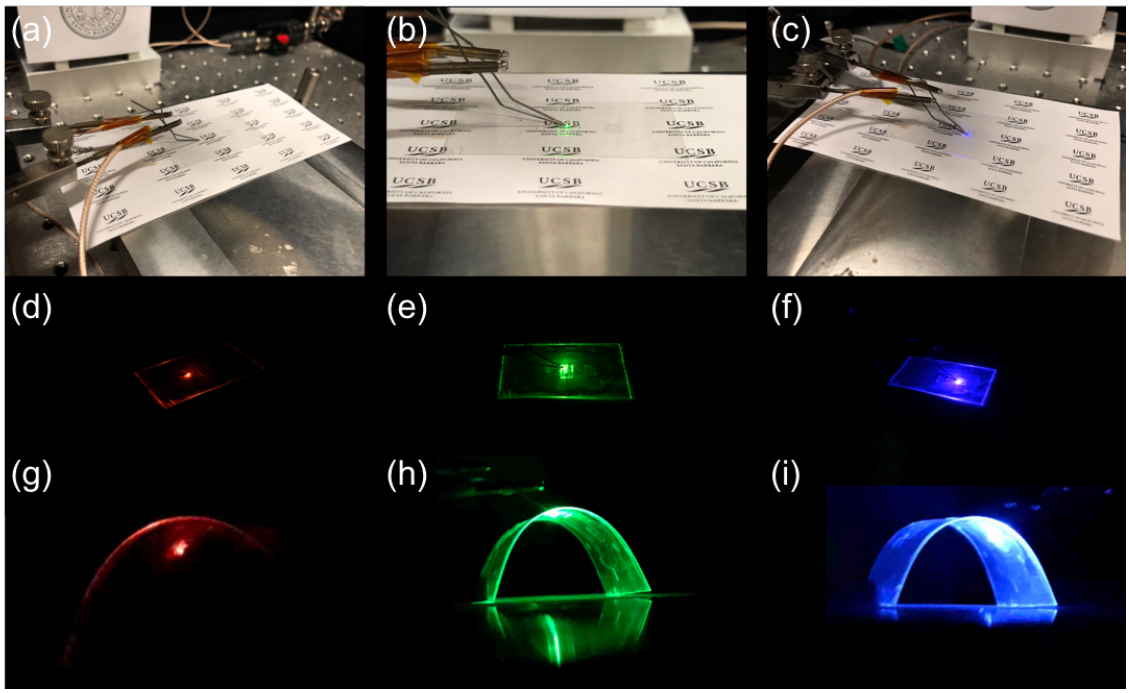


Figure 5.26: Optical photographs of RGB µLEDs on acrylic. The acrylic substrate is 46.5mm × 23.5mm.

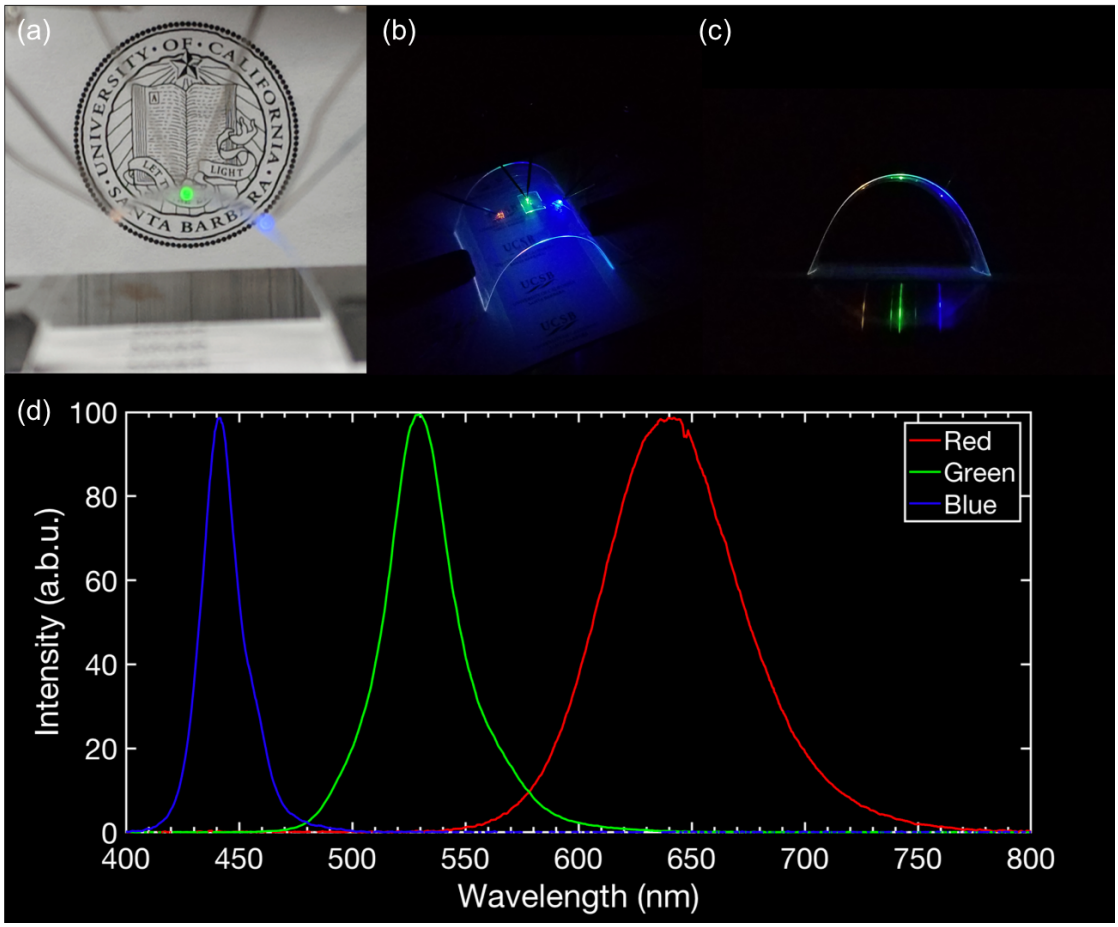


Figure 5.27: (a)-(c) Optical photographs of µLEDs turned on and (d) Wavelength spectra of RGB µLEDs at 20 A/cm$^2$.

# Chapter 6

# Looking Forward

## 6.1 Summary of thesis

This dissertation has covered the µLED ideas and research efforts undertaken at the University of California, Santa Barbara. The motivation behind Chapter 2 came from a simple question: "What happens to the efficiency of InGaN µLEDs as the size shrinks?" The question arose from discussions about the drastic drop of efficiency of red AlGaInP µLEDs. At the time, there had not been much in the research literature to back up this claim about AlGaInP, but it seemed common knowledge to those in the LED industry. This question prompted the experiment laid out in Chapter 2.2 and a large majority of the µLED work throughout the dissertation. Although other research groups had done similar studies, their work was inconclusive as their measurements showed poor EQEs below 10%. The main findings of Chapter 2.2 showed that high efficiencies ($40 - 50\%$) may be sustained (with some loss) as the µLED dimension decreased from 100 µm to 10 µm [53]. The loss of efficiency was attributed to surface recombination at the sidewall, which prompted an experiment on sidewall passivation. Sidewalls passivated with $SiO_2$

deposited by ALD improved the EQE and suppressed reverse leakage current [60].

Around the same time, other researchers at UCSB (mainly Drs. Erin Young, John Leonard, and Benjamin Yonkee) *et al.* demonstrated tunnel junctions grown by a hybrid MOCVD/MBE method [94–96,179]. These projects prompted a review of tunnel junction work grown by MOCVD [87]. Tunnel junction contacts for µLEDs are desirable to allow for $n$-type metal contacts and multiple active region growths on the same wafer. The issue with MOCVD grown tunnel junctions had primarily been the activation mechanism of the buried $p$-GaN (lateral diffusion of hydrogen was not able to completely activate large area LEDs). The dimensions of µLEDs seemed more suitable for achieving complete activation. Chapter 3 detailed the growth and fabrication of µLEDs with tunnel junction contacts [104]. However, there was still a voltage penalty as the smallest $5 \times 5$ µm$^2$ µLEDs still had an additional 1 V compared with µLEDs without tunnel junctions. The voltage penalty seemed to arise from a diffusion barrier at the sidewall. Chemical treatments and anneals were done to remove the barrier, but the voltage penalty still existed. This diffusion barrier is still a large issue for µLEDs with tunnel junction contacts.

Chapter 4 outlined a way to overcome the drop in efficiency with µLED size. Since the loss was due to surface recombination at the sidewall, the active region sidewall was physically separated from the physical mesa sidewall. Current apertures were designed to electrically confine current and define µLED areas. The current apertures were created by implanting areas outside of the µLED with Al ions. The implantation was successful in defining µLED areas, but there was a larger loss of efficiency with size. This loss may have been due to to the damage induced by the implant and a reduced extraction efficiency. However, the "mesa-less" design seems to be the best way to keep µLED efficiencies high.

Chapter 5 presented a new mass transfer method that combined PEC liftoff and transfer printing. The advantage of this technique is that it is compatible with µLEDs

grown on freestanding GaN substrate. While the majority of LEDs and µLEDs use GaN on sapphire (or silicon and silicon carbide), µLEDs on freestanding GaN offer advantages of narrow emission linewidths, stable wavelengths (with current), and longer wavelength emission that may reach the red regime. This method was successful in transferring red, green, and blue InGaN µLEDs to a flexible and transparent acrylic substrate.

## 6.2 Future directions and potential solutions

It is truly an exciting time for µLED research and development. There are many directions in which to continue µLED work. For the tunnel junction project, solving the voltage penalty is the biggest problem. Incorporating InGaN tunnel junctions (rather than GaN) will help reduce the tunneling barrier by taking advantage of the polarization within those layers. However, the most pressing issue is the diffusion barrier at the sidewall. Dry etching results in type conversion ($p$-type to $n$-type) at the very edge, and that $n$-GaN prevents complete diffusion of hydrogen out of the sidewalls. Chemical treatments may not be effective in removing this barrier, but further regrowth on the sidewall after etching the mesa may help recover the $p$-GaN. However, the regrowth is not trivial and requires careful design.

A more promising research direction is addressing the nonradiative recombination at the sidewall that lowers the efficiencies. Sidewall passivation with different materials such as AlN or even GaN by sputter deposition (or for a more complex method, MOCVD) may be promising. On the other hand, a selective MOCVD growth method would eliminate the dry etch from the process. A selective growth of full µLED structures in the desired areas may prevent traps at the sidewall. However, the growth is complicated by faceting of the sidewalls. The µLED dimensions are small enough that faceting would be significant. Furthermore, there may still be surface recombination issues and sidewall passivation

might be necessary. Other directions include continuing with ion implantation to define current apertures. It is unclear whether the lower efficiencies of the ion implanted µLEDs in Chapter 4 were a result of a lowered extraction efficiency, a lowered IQE, or both. Further characterization of the implanted regions combined with ray tracing modeling would elucidate whether the implantation was reducing only the extraction efficiency or the IQE as well.

Indubitably, companies have already answered some of these questions and developed solutions. However, the µLED field is still very young, and there will be much more exciting work to be done. The applications are wide-ranging and may still be in the heads of inventors and dreamers. µLEDs will have a profound impact on the way we receive, use, and transmit information in the world.

# Bibliography


[1] Rolf R. Hainich and Oliver Bimber. *Displays: Fundamentals and Applications*. A K Peters/CRC Press, Boca Raton, second edition, 2011.

[2] Takatoshi Tsujimura. *OLED Display Fundamentals and Applications*. John Wiley & Sons, second edition, 2017.

[3] Daisaku Tanaka, Hisahiro Sasabe, Yan-Jun Li, Shi-Jian Su, Takashi Takeda, and Junji Kido. Ultra high efficiency green organic light-emitting devices. *Japanese J. Appl. Phys. Part 2-Letters Express Lett.*, 46(1-3):L10—-L12, 2007.

[4] Neetu Chopra, Jaewon Lee, Ying Zheng, Sang-Hyun Eom, Jiangeng Xue, and Franky So. High efficiency blue phosphorescent organic light-emitting device. *Appl. Phys. Lett.*, 93(14):143307, 2008.

[5] N. Thejo Kalyani and S.J. Dhoble. Organic light emitting diodes: Energy saving lighting technology-A review. *Renew. Sustain. Energy Rev.*, 16(5):2696–2723, 2012.

[6] Dong Ryun Lee, Bo Seong Kim, Chil Won Lee, Yirang Im, Kyoung Soo Yook, Seok-Ho Hwang, and Jun Yeob Lee. Above 30% External Quantum Efficiency in Green Delayed Fluorescent Organic Light-Emitting Diodes. *ACS Appl. Mater. Interfaces*, page 150429101015009, 2015.

[7] Shuji Nakamura and Michael R. Krames. History of Gallium-Nitride-Based Light-Emitting Diodes for Illumination. *Proc. IEEE*, 101(10):2211–2220, oct 2013.

[8] Christophe A. Hurni, Aurelien David, Michael J. Cich, Rafael I. Aldaz, Bryan Ellis, Kevin Huang, Anurag Tyagi, Remi A. Delille, Michael D. Craven, Frank M. Steranka, and Michael R. Krames. Bulk GaN flip-chip violet light-emitting diodes with optimized efficiency for high-power operation. *Appl. Phys. Lett.*, 106(3):031101, 2015.

[9] Jacob Day, J. Li, D. Y C Lie, Charles Bradford, J. Y. Lin, and H. X. Jiang. III-Nitride full-scale high-resolution microdisplays. *Appl. Phys. Lett.*, 99(3):2–4, 2011.

[10] H. X. Jiang and J. Y. Lin. Nitride micro-LEDs and beyond - a decade progress review. *Opt. Express*, 21(S3):A475, 2013.

[11] H. X. Jiang and J. Y. Lin. Advances in III-nitride microstructures and micro-size emitters. *J. Korean Phys. Soc.*, 42(February):S757–S764, 2003.

[12] Zheng Gong, E. Gu, S. R. Jin, David Massoubre, B. Guilhabert, H. X. Zhang, M. D. Dawson, V. Poher, G. T. Kennedy, P. M. W. French, and M. A. A. Neil. Efficient flip-chip InGaN micro-pixellated light-emitting diode arrays: promising candidates for micro-displays and colour conversion. *J. Phys. D. Appl. Phys.*, 41(9):094002, 2008.

[13] Johannes Herrnsdorf, Jonathan J. D. McKendry, Shuailong Zhang, Enyuan Xie, Ricardo Ferreira, David Massoubre, Ahmad Mahmood Zuhdi, Robert K. Henderson, Ian Underwood, Scott Watson, Anthony E Kelly, Erdan Gu, and Martin D. Dawson. Active-Matrix GaN Micro Light-Emitting Diode Display With Unprecedented Brightness. *IEEE Trans. Electron Devices*, 62(6):1918–1925, 2015.

[14] A. R. Lingley, M. Ali, Y. Liao, R. Mirjalili, M. Klonner, M. Sopanen, S. Suihkonen, T. Shen, B. P. Otis, H. Lipsanen, and B. A. Parviz. A single-pixel wireless contact lens display. *J. Micromechanics Microengineering*, 21(12):125014, 2011.

[15] Zhao Jun Liu, Wing Cheung Chong, Ka Ming Wong, Ka Ho Tam, and Kei May Lau. A novel BLU-free full-color LED projector using LED on silicon micro-displays. *IEEE Photonics Technol. Lett.*, 25(23):2267–2270, 2013.

[16] James R. Bonar, Gareth J. Valentine, Zheng Gong, James Small, and Steve Gorton. High-brightness low-power consumption microLED arrays. In Heonsu Jeon, Li-Wei Tu, Michael R. Krames, and Martin Strassburg, editors, *Proc. SPIE*, volume 9768, page 97680Y, mar 2016.

[17] Woo Sik Jeon, Tae Jin Park, Sun Young Kim, Ramchandra Pode, Jin Jang, and Jang Hyuk Kwon. Low roll-off efficiency green phosphorescent organic light-emitting devices with simple double emissive layer structure. *Appl. Phys. Lett.*, 93(6):063303, 2008.

[18] Michael R. Krames, M. Ochiai-Holcomb, G. E. Höfler, C. Carter-Coman, E. I. Chen, I.-H. Tan, P. Grillot, N. F. Gardner, H. C. Chui, J.-W. Huang, S. A. Stockman, F. A. Kish, M. G. Craford, T. S. Tan, C. P. Kocot, M. Hueschen, J. Posselt, B. Loh, G. Sasser, and D. Collins. High-power truncated-inverted-pyramid AlGaInP/GaP light-emitting diodes exhibiting >50% external quantum efficiency. *Appl. Phys. Lett.*, 75(16):2365–2367, oct 1999.

[19] Abdullah I. Alhassan, Robert M. Farrell, Burhan Saifaddin, Asad Mughal, Feng Wu, Steven P. DenBaars, Shuji Nakamura, and James S. Speck. High luminous efficacy green light-emitting diodes with AlGaN cap layer. *Opt. Express*, 24(16):17868, 2016.

[20] Yukio Narukawa, Masatsugu Ichikawa, Daisuke Sanga, Masahiko Sano, and Takashi Mukai. White light emitting diodes with super-high luminous efficacy. *J. Phys. D. Appl. Phys.*, 43(35), 2010.

[21] P. Royo, R. P. Stanley, M. Ilegems, K. Streubel, and K. H. Gulden. Experimental determination of the internal quantum efficiency of AlGaInP microcavity light-emitting diodes. *J. Appl. Phys.*, 91(5):2563–2568, 2002.

[22] Jeong-Tak Oh, Sang-Youl Lee, Yong-Tae Moon, Ji Hyung Moon, Sunwoo Park, Ki Yong Hong, Ki Young Song, Chan-Hyoung Oh, Jong-In Shim, Hwang-Hee Jeong, June-O Song, Hiroshi Amano, and Tae-Yeon Seong. Light output performance of red AlGaInP-based light emitting diodes with different chip geometries and structures. *Opt. Express*, 26(9):11194–11200, 2018.

[23] Michael R. Krames, Oleg B. Shchekin, Regina Mueller-Mach, Gerd O. Mueller, Ling Zhou, Gerard Harbers, and M. George Craford. Status and Future of High-Power Light-Emitting Diodes for Solid-State Lighting. *J. Disp. Technol.*, 3(2):160–175, jun 2007.

[24] S. D. Lester, F. A. Ponce, M. G. Craford, and D. A. Steigerwald. High dislocation densities in high efficiency GaN-based light-emitting diodes. *Appl. Phys. Lett.*, 66(10):1249–1251, 1995.

[25] Nick Holonyak and S. F. Bevacqua. Coherent (visible) light emission from GaAsP junctions. *Appl. Phys. Lett.*, 1(4):82–83, 1962.

[26] D. A. Vanderwater, I. H. Tan, G. E. Höfler, D. C. Defevere, and F. A. Kish. High-brightness AlGaInP light emitting diodes. *Proc. IEEE*, 85(11):1752–1763, 1997.

[27] Klaus Streubel, Norbert Linder, Ralph Wirth, and Arndt Jaeger. High brightness AlGaInP light-emitting diodes. *IEEE J. Sel. Top. Quantum Electron.*, 8(2):321–332, 2002.

[28] Th. Gessmann and E. F. Schubert. High-efficiency AlGaInP light-emitting diodes for solid-state lighting applications. *J. Appl. Phys.*, 95(5):2203–2216, 2004.

[29] C. P. Kuo, R. M. Fletcher, T. D. Osentowski, M. C. Lardizabal, M. G. Craford, and V. M. Robbins. High performance AlGaInP visible light-emitting diodes. *Appl. Phys. Lett.*, 57(27):2937–2939, 1990.

[30] H. Sugawara, M. Ishikawa, and G. Hatakoshi. High-efficiency InGaAlP/GaAs visible light-emitting diodes. *Appl. Phys. Lett.*, 58(10):1010–1012, 1991.

[31] F. A. Kish, F. M. Steranka, D. C. Defevere, D. A. Vanderwater, K. G. Park, C. P. Kuo, T. D. Osentowski, M. J. Peanasky, J. G. Yu, R. M. Fletcher, D. A. Steigerwald,

M. G. Craford, and V. M. Robbins. Very high-efficiency semiconductor wafer-bonded transparent-substrate AlGaInP/GaP light-emitting diodes. *Appl. Phys. Lett.*, 64(21):2839–2841, 1994.

[32] F. A. Kish, D. A. Vanderwater, M. J. Peanasky, M. J. Ludowise, S. G. Hummel, and S. J. Rosner. Low-resistance Ohmic conduction across compound semiconductor wafer-bonded interfaces. *Appl. Phys. Lett.*, 67(1995):2060, 1995.

[33] G. E. Höfler, D. A. Vanderwater, D. C. DeFevere, F. A. Kish, M. D. Camras, F. M. Steranka, and I.H. Tan. Wafer bonding of 50mm diameter GaP to AlGaInP-GaP light-emitting diode wafers. *Appl. Phys. Lett.*, 69(6):803–805, 1996.

[34] Daniel F. Feezell, James S. Speck, Steven P. DenBaars, and Shuji Nakamura. Semipolar (20-2-1) InGaN/GaN Light-Emitting Diodes for High-Efficiency Solid-State Lighting. *J. Disp. Technol.*, 9(4):190–198, apr 2013.

[35] Jea-Hyun Ryou, P Douglas Yoder, Jianping Liu, Zachary Lochner, Hyunsoo Kim, Hee Jin Kim, and Russel D. Dupuis. Control of Quantum-Confinement Stark Effect in InGaN-Based Quantum Wells. *IEEE J. Sel. Top. Quantum Electron. Vol. 15, No. 4*, 15(4):1080–1091, 2009.

[36] M. Khoury, M. Leroux, M. Nemoz, G. Feuillet, J. Zúñiga-Pérez, and P. Vennéguès. Growth of semipolar (2021) GaN layers on patterned silicon (114) 1 off by Metal Organic Vapor Phase Epitaxy. *J. Cryst. Growth*, 419:88–93, 2015.

[37] Michel Khoury, Hongjian Li, Leah Y. Kuritzky, Asad J. Mughal, Philippe DeMierry, Shuji Nakamura, James S. Speck, and Steven P. DenBaars. 444-nm InGaN light-emitting diodes on low-defect-density (11-22) GaN templates on patterned sapphire. *Appl. Phys. Express*, 10:106501, 2017.

[38] Hongjian Li, Michel Khoury, Bastien Bonef, Abdullah I. Alhassan, Asad J. Mughal, Ezzah Azimah, Muhammad E.A. Samsudin, Philippe De Mierry, Shuji Nakamura, James S. Speck, and Steven P. DenBaars. Efficient Semipolar (11-22) 550 nm Yellow/Green InGaN Light-Emitting Diodes on Low Defect Density (11-22) GaN/Sapphire Templates. *ACS Appl. Mater. Interfaces*, 9(41):36417–36422, 2017.

[39] Yuji Zhao, Sang Ho Oh, Feng Wu, Yoshinobu Kawaguchi, Shinichi Tanaka, Kenji Fujito, James S. Speck, Steven P. DenBaars, and Shuji Nakamura. Green Semipolar (20-2-1) InGaN Light-Emitting Diodes with Small Wavelength Shift and Narrow Spectral Linewidth. *Appl. Phys. Express*, 6(6):062102, jun 2013.

[40] Yuji Zhao, Qimin Yan, Chia-Yen Huang, Shih-Chieh Huang, Po Shan Hsu, Shinichi Tanaka, Chih-Chien Pan, Yoshinobu Kawaguchi, Kenji Fujito, Chris G. Van de Walle, James S. Speck, Steven P. DenBaars, Shuji Nakamura, and Daniel Feezell. Indium incorporation and emission properties of nonpolar and semipolar InGaN quantum wells. *Appl. Phys. Lett.*, 100(20):201108, 2012.

[41] S. X. Jin, J. Li, J. Y. Lin, and H. X. Jiang. InGaN/GaN quantum well interconnected microdisk light emitting diodes. *Appl. Phys. Lett.*, 77(20):3236, 2000.

[42] H. X. Jiang, S. X. Jin, J. Li, J. Shakya, and J. Y. Lin. III-nitride blue microdisplays. *Appl. Phys. Lett.*, 78(9):1303–1305, 2001.

[43] S. X. Jin, J. Shakya, J. Y. Lin, and H. X. Jiang. Size dependence of III-nitride microdisk light-emitting diode characteristics. *Appl. Phys. Lett.*, 78(22):3532–3534, 2001.

[44] Z. Y. Fan, J. Y. Lin, and H. X. Jiang. III-nitride micro-emitter arrays: development and applications. *J. Phys. D. Appl. Phys.*, 41:094001, 2008.

[45] Zheng Gong, Shirong Jin, Yujie Chen, Jonathan McKendry, David Massoubre, Ian M. Watson, Erdan Gu, and Martin D. Dawson. Size-dependent light output, spectral shift, and self-heating of 400 nm InGaN light-emitting diodes. *J. Appl. Phys.*, 107(1):013103, jan 2010.

[46] C. W. Jeon, H. W. Choi, and M. D. Dawson. Fabrication of matrix-addressable InGaN-based microdisplays of high array density. *IEEE Photonics Technol. Lett.*, 15(11):1516–1518, 2003.

[47] S Lu, W Liu, Z H Zhang, S T Tan, Z Ju, Y Ji, X Zhang, Y Zhang, B Zhu, Z Kyaw, N Hasanov, X W Sun, and Hilmi Volkan Demir. Low thermal-mass LEDs: size effect and limits. *Opt. Express*, 22(26):32200–32207, 2014.

[48] Jonathan J. D. McKendry, R.P. Green, A.E. Kelly, Zheng Gong, B. Guilhabert, David Massoubre, E. Gu, and M. D. Dawson. High-Speed Visible Light Communications Using Individual Pixels in a Micro Light-Emitting Diode Array. *IEEE Photonics Technol. Lett.*, 22(18):1346–1348, 2010.

[49] Pengfei Tian, Jonathan J D McKendry, Zheng Gong, Benoit Guilhabert, Ian M. Watson, Erdan Gu, Zhizhong Chen, Guoyi Zhang, and Martin D. Dawson. Size-dependent efficiency and efficiency droop of blue InGaN micro-light emitting diodes. *Appl. Phys. Lett.*, 101(23):231110, dec 2012.

[50] François Olivier, Sauveur Tirano, Ludovic Dupré, Bernard Aventurier, Christophe Largeron, and François Templier. Influence of size-reduction on the performances of GaN-based micro-LEDs for display application. *J. Lumin.*, pages 1–5, sep 2016.

[51] Kirill A. Bulashevich and Sergey Yu Karpov. Impact of surface recombination on efficiency of III-nitride light-emitting diodes. *Phys. Status Solidi - Rapid Res. Lett.*, 484(6):480–484, 2016.

[52] Sergey S. Konoplev, Kirill A. Bulashevich, and Sergey Yu. Karpov. From Large-Size to Micro-LEDs: Scaling Trends Revealed by Modeling. *Phys. Status Solidi*, 1700508:1700508, 2017.

[53] David Hwang, Asad Mughal, Christopher D. Pynn, Shuji Nakamura, and Steven P. DenBaars. Sustained high external quantum efficiency in ultrasmall blue IIInitride micro-LEDs. *Appl. Phys. Express*, 10(3):032101, 2017.

[54] M. Boroditsky, I. Gontijo, M. Jackson, R. Vrijen, E. Yablonovitch, T. Krauss, Chuan-Cheng Cheng, A. Scherer, R. Bhat, and Michael R. Krames. Surface recombination measurements on III-V candidate materials for nanostructure light-emitting diodes. *J. Appl. Phys.*, 87(7):3497, 2000.

[55] Sergey Karpov. ABC-model for interpretation of internal quantum efficiency and its droop in III-nitride LEDs. *Proc. Int. Conf. Numer. Simul. Optoelectron. Devices, NUSOD*, pages 17–18, 2014.

[56] Claude Weisbuch, Marco Piccardo, Lucio Martinelli, Justin Iveland, Jacques Peretti, and James S. Speck. The efficiency challenge of nitride light-emitting diodes for lighting. *Phys. Status Solidi Appl. Mater. Sci.*, 212(5):899–913, 2015.

[57] Francois Olivier, Anis Daami, Christophe Licitra, and Francois Templier. Shockley-Read-Hall and Auger non-radiative recombination in GaN based LEDs: A size effect study. *Appl. Phys. Lett.*, 111(2):022104, jul 2017.

[58] Ja-Yeon Kim Ja-Yeon Kim, Min-Ki Kwon Min-Ki Kwon, Jae-Pil Kim Jae-Pil Kim, and Seong-Ju Park Seong-Ju Park. Enhanced Light Extraction From Triangular GaN-Based Light-Emitting Diodes. *IEEE Photonics Technol. Lett.*, 19(23):1865–1867, 2007.

[59] Han-Youl Ryu and Jong-In Shim. Effect of current spreading on the efficiency droop of InGaN light-emitting diodes. *Opt. Express*, 19(4):2886, 2011.

[60] Matthew S. Wong, David Hwang, Abdullah I. Alhassan, Changmin Lee, Ryan Ley, Shuji Nakamura, and Steven P. DenBaars. High efficiency of III-nitride micro-light-emitting diodes by sidewall passivation using atomic layer deposition. *Opt. Express*, 26(16):21324–21331, 2018.

[61] Justin Iveland, Lucio Martinelli, Jacques Peretti, James S. Speck, and Claude Weisbuch. Direct measurement of auger electrons emitted from a semiconductor light-emitting diode under electrical injection: Identification of the dominant mechanism for efficiency droop. *Phys. Rev. Lett.*, 110(17):1–5, 2013.

[62] Ji Myon Lee, Chul Huh, Dong Joon Kim, and Seong Ju Park. Dry-etch damage and its recovery in InGaN/GaN multi-quantum-well light-emitting diodes. *Semicond. Sci. Technol.*, 18(6):530–534, 2003.

[63] Keita Kataoka, Masakazu Kanechika, Tetsuo Narita, Yasuji Kimoto, and Akira Uedono. Positron annihilation and cathodoluminescence study on inductively coupled plasma etched GaN. *Phys. Status Solidi Basic Res.*, 252(5):913–916, 2015.

[64] Silvia H. Chan, Stacia Keller, Maher Tahhan, Haoran Li, Brian Romanczyk, Steven P. Denbaars, and Umesh K. Mishra. High electron mobility recovery in AlGaN/GaN 2DEG channels regrown on etched surfaces. *Semicond. Sci. Technol.*, 31(6):1–8, 2016.

[65] Jun Hee Choi, Eun Hyoung Cho, Yun Sung Lee, Mun Bo Shim, Ho Young Ahn, Chan Wook Baik, Eun Hong Lee, Kihong Kim, Tae Ho Kim, Sangwon Kim, Kyung Sang Cho, Jongseung Yoon, Miyoung Kim, and Sungwoo Hwang. Fully flexible gan light-emitting diodes through nanovoid-mediated transfer. *Adv. Opt. Mater.*, 2(3):267–274, 2014.

[66] Yuanzheng Yue, Xiaodong Yan, Wenjun Li, Huili Grace Xing, Debdeep Jena, and Patrick Fay. Faceted sidewall etching of n-GaN on sapphire by photoelectrochemical wet processing. *J. Vac. Sci. Technol. B, Nanotechnol. Microelectron. Mater. Process. Meas. Phenom.*, 32(6):061201, 2014.

[67] C. H. Chou, C. L. Lin, Y. C. Chuang, H. Y. Bor, and C. Y. Liu. High thermally stable Ni/Ag(Al) alloy contacts on p-GaN. *Appl. Phys. Lett.*, 90:31–33, 2007.

[68] Benjamin P. Yonkee, Robert M. Farrell, John T. Leonard, Steven P. DenBaars, James S. Speck, and Shuji Nakamura. Demonstration of low resistance ohmic contacts to p-type (20-2-1) GaN. *Semicond. Sci. Technol.*, 30(7):075007, 2015.

[69] Giuseppe Greco, Ferdinando Iucolano, and Fabrizio Roccaforte. Applied Surface Science Ohmic contacts to Gallium Nitride materials. *Appl. Surf. Sci.*, 383:324–345, 2016.

[70] Asad J. Mughal, Sang Ho Oh, Anisa Myzaferi, Shuji Nakamura, James S. Speck, and Steven P. DenBaars. High-power LEDs using Ga-doped ZnO current-spreading layers. *Electron. Lett.*, 52(4):304–306, feb 2016.

[71] B. Pödör. Acceptor ionization energies in gallium nitride : chemical trends and electronegativities. *Semicond. Sci. Technol.*, 11:827–829, 1996.

[72] Francisco Mireles and Sergio E Ulloa. Acceptor binding energies in GaN and AlN. *Phys. Rev. B*, 58(7):3879–3887, 1998.

[73] Chris G. Van De Walle, C. Stampfl, Jörg Neugebauer, M. D. McClusckey, and N. M. Johnson. Doping of AlGaN Alloys. *Mrs Internet J. Nitride Semicond. Res.*, 4S1(G10.4):1–12, 1999.

[74] H. Wang and A. B. Chen. Calculation of shallow donor levels in GaN. *J. Appl. Phys.*, 87(11):7859–7863, 2000.

[75] John Simon, Ze Zhang, Kevin Goodman, Huili Xing, Thomas Kosel, Patrick Fay, and Debdeep Jena. Polarization-Induced Zener Tunnel Junctions in Wide-Band-Gap Heterostructures. *Phys. Rev. Lett.*, 103(2):026801, 2009.

[76] Seong Ran Jeon, Young Ho Song, Ho Jin Jang, Gye Mo Yang, Soon Won Hwang, and Sung Jin Son. Lateral current spreading in GaN-based light-emitting diodes utilizing tunnel contact junctions. *Appl. Phys. Lett.*, 78(21):3265–3267, 2001.

[77] Tetsuya Takeuchi, Ghulam Hasnain, Scott Corzine, Mark Hueschen, Richard P. Schneider, Chris Kocot, Mats Blomqvist, Ying-lan Chang, Dale Lefforge, Mike R. Krames, Lou W. Cook, and Steve A. Stockman. GaN-Based Light Emitting Diodes with Tunnel Junctions. *Jpn. J. Appl. Phys.*, 40(Part 2, No. 8B):L861 – L863, 2001.

[78] Seong Ran Jeon, Chang Sok Oh, Jeon Wook Yang, Gye Mo Yang, and Byueng Su Yoo. GaN tunnel junction as a current aperture in a blue surface-emitting light-emitting diode. *Appl. Phys. Lett.*, 80(11):1933–1935, 2002.

[79] Shuji Nakamura, N Iwasa, M Senoh, and Takashi Mukai. Hole Compensation Mechanism of P-Type GaN Films. *Jpn. J. Appl. Phys.*, 1992.

[80] Shuji Nakamura, Takashi Mukai, M Senoh, and N Iwasa. Thermal Annealing Effects on P-Type Mg-Doped GaN Films. *Jpn. J. Appl. Phys*, 31:139–142, 1992.

[81] Jörg Neugebauer and Chris G. Van de Walle. Role Of Hydrogen And Hydrogen Complexes In Doping Of Gan. *MRS Proc.*, 423:619, feb 1996.

[82] Jörg Neugebauer and Chris G. Van de Walle. Hydrogen in GaN: Novel Aspects of a Common Impurity. *Phys. Rev. Lett.*, 75(24):4452–4456, 1995.

[83] Huili Xing, Daniel S. Green, Haijiang Yu, Tom Mates, Peter Kozodoy, Stacia Keller, Steven P. DenBaars, and Umesh K. Mishra. Memory Effect and Redistribution of Mg into Sequentially Regrown GaN Layer by Metalorganic Chemical Vapor Deposition. *Jpn. J. Appl. Phys.*, 42(Part 1, No. 1):50–53, jan 2003.

[84] Kazuyoshi Tomita, Kenji Itoh, Osamu Ishiguro, Tetsu Kachi, and Nobuhiko Sawaki. Reduction of Mg segregation in a metalorganic vapor phase epitaxial grown GaN layer by a low-temperature AlN interlayer. *J. Appl. Phys.*, 104(1):014906, jul 2008.

[85] Srabanti Chowdhury, Brian L. Swenson, Jing Lu, and Umesh K. Mishra. Use of Sub-nanometer Thick AlN to Arrest Diffusion of Ion-Implanted Mg into Regrown AlGaN/GaN Layers. *Jpn. J. Appl. Phys.*, 50(10):101002, oct 2011.

[86] Anchal Agarwal, Maher Tahhan, Tom Mates, Stacia Keller, and Umesh Mishra. Suppression of Mg propagation into subsequent layers grown by MOCVD. *J. Appl. Phys.*, 121(2):025106, 2017.

[87] Yuka Kuwano, Mitsuru Kaga, Takatoshi Morita, Kouji Yamashita, Kouta Yagi, Motoaki Iwaya, Tetsuya Takeuchi, Satoshi Kamiyama, and Isamu Akasaki. Lateral Hydrogen Diffusion at p-GaN Layers in Nitride-Based Light Emitting Diodes with Tunnel Junctions. *Jpn. J. Appl. Phys.*, 52(8S):08JK12, aug 2013.

[88] S Neugebauer, M. P. Hoffmann, H Witte, J Bläsing, A Dadgar, A Strittmatter, T Niermann, M Narodovitch, and M Lehmann. All metalorganic chemical vapor phase epitaxy of p/n-GaN tunnel junction for blue light emitting diode applications. *Appl. Phys. Lett.*, 110(10):102104, mar 2017.

[89] Zi-Hui Zhang, Swee Tiam Tan, Zabu Kyaw, Yun Ji, Wei Liu, Zhengang Ju, Namig Hasanov, Xiao Wei Sun, and Hilmi Volkan Demir. InGaN/GaN light-emitting diode with a polarization tunnel junction. *Appl. Phys. Lett.*, 102(19):193508, may 2013.

[90] Mitsuru Kaga, Takatoshi Morita, Yuka Kuwano, Kouji Yamashita, Kouta Yagi, Motoaki Iwaya, Tetsuya Takeuchi, Satoshi Kamiyama, and Isamu Akasaki. GaInN-Based Tunnel Junctions in n-p-n Light Emitting Diodes. *Jpn. J. Appl. Phys.*, 52(8S):08JH06, aug 2013.

[91] Daiki Takasuka, Yasuto Akatsuka, Masataka Ino, Norikatsu Koide, Tetsuya Takeuchi, Motoaki Iwaya, Satoshi Kamiyama, and Isamu Akasaki. GaInN-based tunnel junctions with graded layers. *Appl. Phys. Express*, 9(8):4–7, 2016.

[92] M. Malinverni, Denis Martin, and N. Grandjean. InGaN based micro light emitting diodes featuring a buried GaN tunnel junction. *Appl. Phys. Lett.*, 107(5):051107, 2015.

[93] Sriram Krishnamoorthy, Fatih Akyol, and Siddharth Rajan. InGaN/GaN tunnel junctions for hole injection in GaN light emitting diodes. *Appl. Phys. Lett.*, 105(14):141104, oct 2014.

[94] Erin C. Young, Benjamin P. Yonkee, Feng Wu, Sang Ho Oh, Steven P. DenBaars, Shuji Nakamura, and James S. Speck. Hybrid tunnel junction contacts to III-nitride light-emitting diodes. *Appl. Phys. Express*, 9(2):022102, feb 2016.

[95] Benjamin P. Yonkee, Erin C. Young, Changmin Lee, John T. Leonard, Steven P. DenBaars, James S. Speck, and Shuji Nakamura. Demonstration of a III-nitride edge-emitting laser diode utilizing a GaN tunnel junction contact. *Opt. Express*, 24(7):7816, apr 2016.

[96] Benjamin P. Yonkee, Erin C. Young, Steven P. DenBaars, Shuji Nakamura, and James S. Speck. Silver free III-nitride flip chip light-emitting-diode with wall plug efficiency over 70% utilizing a GaN tunnel junction. *Appl. Phys. Lett.*, 109(19):191104, nov 2016.

[97] Ho Won Jang and Jong Lam Lee. Low-resistance and high-reflectance Ni/Ag/Ru/Ni/Au ohmic contact on p-type GaN. *Appl. Phys. Lett.*, 85(19):4421–4423, 2004.

[98] Ho Won Jang, Jun Ho Son, and Jong-Lam Lee. Formation of High-Quality Ag-Based Ohmic Contacts to p-Type GaN. *J. Electrochem. Soc.*, 155:H563, 2008.

[99] Jun Ho Son, Yang Hee Song, Hak Ki Yu, and Jong Lam Lee. Effects of Ni cladding layers on suppression of Ag agglomeration in Ag-based Ohmic contacts on p-GaN. *Appl. Phys. Lett.*, 95(6):1–4, 2009.

[100] Munsik Oh and Hyunsoo Kim. High-efficiency GaN-based light-emitting diodes fabricated with identical Ag contact formed on both n- and p-layers. *Opt. Express*, 21(18):20857–20862, 2013.

[101] P. Boguslawski, E. L. Briggs, and J. Bernholc. Native defects in gallium nitride. *Phys. Rev. B*, 51(23):17255–17258, 1995.

[102] Stacy J. Kowsz, Erin C. Young, Benjamin P. Yonkee, Christopher D. Pynn, Robert M. Farrell, James S. Speck, Steven P. DenBaars, and Shuji Nakamura. Using tunnel junctions to grow monolithically integrated optically pumped semipolar III-nitride yellow quantum wells on top of electrically injected blue quantum wells. *Opt. Express*, 25(4):3841, 2017.

[103] Abdullah I. Alhassan, Erin C. Young, Ahmed Y. Alyamani, Abdulrahman Albadri, Shuji Nakamura, Steven P. DenBaars, and James S. Speck. Reduced-droop green III-nitride light-emitting diodes utilizing GaN tunnel junction. *Appl. Phys. Express*, 11(4), 2018.

[104] David Hwang, Asad Mughal, Matthew S. Wong, Abdullah I. Alhassan, Shuji Nakamura, and Steven P. DenBaars. Micro-light-emitting diodes with III-nitride tunnel junction contacts grown by metalorganic chemical vapor deposition. *Appl. Phys. Express*, 11, 2018.

[105] Emmanouil Kioupakis, Patrick Rinke, André Schleife, Friedhelm Bechstedt, and Chris G. Van De Walle. Free-carrier absorption in nitrides from first principles. *Phys. Rev. B - Condens. Matter Mater. Phys.*, 81(24):2–5, 2010.

[106] Emmanouil Kioupakis, Patrick Rinke, and Chris G. Van De Walle. Determination of internal loss in nitride lasers from first principles. *Appl. Phys. Express*, 3(8):17–20, 2010.

[107] X. A. Cao, S. J. Pearton, A. P. Zhang, G. T. Dang, F. Ren, R. J. Shul, L. Zhang, R. Hickman, and J. M. Van Hove. Electrical effects of plasma damage in p-GaN. *Appl. Phys. Lett.*, 75(17):2569–2571, 1999.

[108] X. A. Cao, A. P. Zhang, G. T. Dang, F. Ren, S. J. Pearton, J. M. Van Hove, R. A. Hickman, R. J. Shul, and L. Zhang. Plasma damage in p-GaN. *J. Electron. Mater.*, 29(3):256–261, 2000.

[109] Y. Yang and X. A. Cao. Removing plasma-induced sidewall damage in GaN-based light-emitting diodes by annealing and wet chemical treatments. *J. Vac. Sci. Technol. B Microelectron. Nanom. Struct.*, 27(6):2337, 2009.

[110] X. A. Cao, H. T. Hu, Y. Dong, X. M. Ding, and X. Y. Hou. The structural, chemical, and electronic properties of a stable GaS/GaAs interface. *J. Appl. Phys.*, 86(12):6940–6944, 1999.

[111] Keon Hwa Lee, Ki Man Kang, Gi Cheol Hong, Seung Hwan Kim, Woo Young Sun, and Gye Mo Yang. Improved light extraction of GaN-based light-emitting diodes by an ion-damaged current blocking layer. *Jpn. J. Appl. Phys.*, 51(8 PART 1), 2012.

[112] S. D. Wolter, B. P. Luther, D. L. Waltemyer, C. Önneby, S. E. Mohney, and R. J. Molnar. X-ray photoelectron spectroscopy and x-ray diffraction study of the thermal oxide on gallium nitride. *Appl. Phys. Lett.*, 70(16):2156–2158, 1997.

[113] S. D. Wolter, J. M. Delucca, S. E. Mohney, R. S. Kern, and C. P. Kuo. Investigation into the early stages of oxide growth on gallium nitride. *Thin Solid Films*, 371(1):153–160, 2000.

[114] S. Pal, R. Mahapatra, S. K. Ray, B. R. Chakraborty, S. M. Shivaprasad, S. K. Lahiri, and D. N. Bose. Microwave plasma oxidation of gallium nitride. *Thin Solid Films*, 425(1-2):20–23, feb 2003.

[115] L. H. Peng, C. H. Liao, Y. C. Hsu, C. S. Jong, C. N. Huang, J. K. Ho, C. C. Chiu, and C. Y. Chen. Photoenhanced wet oxidation of gallium nitride. *Appl. Phys. Lett.*, 76(4):511–513, 2000.

[116] S. J. Pearton, C. B. Vartuli, J. C. Zolper, C. Yuan, and R. A. Stall. Ion implantation doping and isolation of GaN. *Appl. Phys. Lett.*, 67(1995):1435, 1995.

[117] J.C. Zolper, S.J. Pearton, R.G. Wilson, and R.a. Stall. Implant activation and redistribution of dopants in GaN. In *Proc. 11th Int. Conf. Ion Implant. Technol.*, pages 705–708. IEEE, 1996.

[118] J. C. Zolper and R. J. Shul. Implantation and dry etching of group-III-nitride semiconductors. *MRS Bull.*, 22(2):36–43, 1997.

[119] A. Edwards, Mulpuri V. Rao, B. Molnar, A. E. Wickenden, O. W. Holland, and P. H. Chi. Ion implantation doping of OMCVD grown GaN. *J. Electron. Mater.*, 26(3):334–339, 1997.

[120] H Paul Maruska, Mike Lioubtchenko, Thomas G Tetreault, Stephen J Pearton, Matthew Schurmant, Robert Vaudo, Qisheng Chen, and Randy J Shult. WIDE BAND GAP SEMICONDUCTORS. *Mat. Res. Soc. Symp. Proc.*, 483:333–344, 1998.

[121] S O Kucheyev, J S Williams, and Stephen J. Pearton. Ion implantation into GaN. *Mater. Sci. Eng.*, 33:51–107, 2001.

[122] I. O. Usov, D. Koleske, and K. E. Sickafus. Ion implantation damage recovery in GaN. *Nucl. Instruments Methods Phys. Res. Sect. B Beam Interact. with Mater. Atoms*, 267(17):2962–2964, 2009.

[123] K. Lorenz, E. Wendler, A. Redondo-Cubero, N. Catarino, M. P. Chauvat, S. Schwaiger, F. Scholz, E. Alves, and P. Ruterana. Implantation damage formation in a-, c- and m-plane GaN. *Acta Mater.*, 123:177–187, 2017.

[124] Shih-Yung Huang, Ray-Hua Horng, Hao-Chung Kuo, and Dong-Sing Wuu. Fabrication and Characterization of InGaN-Based Green Resonant-Cavity LEDs Using Hydrogen Ion-Implantation Techniques. *J. Electrochem. Soc.*, 154(11):H962, 2007.

[125] Juho Kim, Jeongwoo Hwang, Kwangsun Song, Namyun Kim, Jae Cheol Shin, and Jongho Lee. Ultra-thin flexible GaAs photovoltaics in vertical forms printed on metal surfaces without interlayer adhesives. *Appl. Phys. Lett.*, 108(25):1–5, 2016.

[126] Bo Siao Cheng, Chia En Lee, Hao Chung Kuo, Tien Chang Lu, and Shing Chung Wang. Power enhancement of GaN-based flip-chip light-emitting diodes with triple roughened surfaces. *Jpn. J. Appl. Phys.*, 48(4 PART 2):48–50, 2009.

[127] David S. Meyaard, Ming Ma, E Fred Schubert, Chel-Jong Choi, Jaehee Cho, and Morgan Evans. Mesa-Free III-V Nitride Light-Emitting Diodes with Flat Surface. *ECS Solid State Lett.*, 3(4):17–19, 2014.

[128] John T. Leonard, Daniel A. Cohen, Benjamin P. Yonkee, Robert M. Farrell, Tal Margalith, Seunggeun Lee, Steven P. Denbaars, James S. Speck, and Shuji Nakamura. Nonpolar III-nitride vertical-cavity surface-emitting lasers incorporating an ion implanted aperture. *Appl. Phys. Lett.*, 107(1), 2015.

[129] J. F. Ziegler, J. P. Biersack, and M. D. Ziegler. *The Stopping and Range of Ions in Solids*. Pergamon, Oxford, 1985.

[130] Chuan Wang, David Hwang, Zhibin Yu, Kuniharu Takei, Junwoo Park, Teresa Chen, Biwu Ma, and Ali Javey. User-interactive electronic skin for instantaneous pressure visualization. *Nat. Mater.*, 12(10):899–904, oct 2013.

[131] A. R. Clawson. Guide to references on III-V semiconductor chemical etching. *Mater. Sci. Eng. R Reports*, 31:1–438, 2001.

[132] D. A. Stocker and E. Fred Schubert. Crystallographic wet chemical etching of GaN. *Appl. Phys. Lett.*, 73(18):2654–2656, 1998.

[133] D. Zhuang and J. H. Edgar. Wet etching of GaN, AlN, and SiC: A review, jan 2005.

[134] W. S. Wong, T. Sands, and N. W. Cheung. Damage-free separation of GaN thin films from sapphire substrates. *Appl. Phys. Lett.*, 72(5):599–601, 1998.

[135] Michael K. Kelly, Robert P. Vaudo, Vivek M. Phanse, Lutz Gorgens, Oliver Ambacher, and Martin Stutzmann. Large Free-Standing GaN Substrates by Hydride Vapor Phase Epitaxy and Laser-Induced Liftoff. *Jpn. J. Appl. Phys.*, 38(3):L217–L219, 1999.

[136] Ralph Delmdahl, Rainer Pätzel, Jan Brune, Rolf Senczuk, Christian Goßler, Rüdiger Moser, Michael Kunzer, and Ulrich T. Schwarz. Line beam processing for laser lift-off of GaN from sapphire. *Phys. Status Solidi*, 209(12):2653–2658, dec 2012.

[137] Ralph Delmdahl, Rainer Pätzel, and Jan Brune. Large-Area Laser-Lift-Off Processing in Microelectronics. *Phys. Procedia*, 41:241–248, jan 2013.

[138] Daisuke Iida, Syunsuke Kawai, Nobuaki Ema, Takayoshi Tsuchiya, Motoaki Iwaya, Tetsuya Takeuchi, Satoshi Kamiyama, and Isamu Akasaki. Laser lift-off technique for freestanding GaN substrate using an In droplet formed by thermal decomposition of GaInN and its application to light-emitting diodes. *Appl. Phys. Lett.*, 105(7):072101, aug 2014.

[139] A. Tauzin, T. Akatsu, M. Rabarot, J. Dechamp, M. Zussy, H. Moriceau, J. F. Michaud, A.M. Charvet, L. Di Cioccio, F. Fournel, J. Garrione, B. Faure, F. Letertre, and N. Kernevez. Transfers of 2-inch GaN films onto sapphire substrates using Smart Cut technology. *Electron. Lett.*, 41(11):11–12, 2005.

[140] M. Bruel. Silicon on Insulator Material Technology. *Electron. Lett.*, 31(14):1201–1202, 1995.

[141] E. Padilla, M. Jackson, and M. S. Goorsky. The role of the nucleation annealing temperature annealing on the exfoliation of hydrogen-implanted GaN. *ECS Trans.*, 33(4):263–270, 2010.

[142] Oussama Moutanabbir and Ulrich Gösele. Heterogeneous Integration of Compound Semiconductors. *Annu. Rev. Mater. Res.*, 40(1):469–500, jun 2010.

[143] Uday Dadwal and Rajendra Singh. A Comparative Study of Hydrogen Implantation Induced Blistering and Exfoliation in GaN and AlN. *Jpn. J. Appl. Phys.*, 52(8S):08JE12, aug 2013.

[144] T. Detchprohm, Hiroshi Amano, Kazumasa Hiramatsu, and Isamu Akasaki. The growth of thick GaN film on sapphire substrate by using ZnO buffer layer. *J. Cryst. Growth*, 128:384–390, 1993.

[145] H. F. Liu, W. Liu, and S. J. Chua. Epitaxial growth and chemical lift-off of GaInN/GaN heterostructures on c- and r-sapphire substrates employing ZnO sacrificial templates. *J. Vac. Sci. Technol. A Vacuum, Surfaces, Film.*, 28(4):590, 2010.

[146] S. Gautier, T. Moudakir, G. Patriarche, D.J. Rogers, V.E. Sandana, F. Hosseini Téherani, P. Bove, Y. El Gmili, K. Pantzas, Suresh Sundaram, D. Troadec, P.L. Voss, M. Razeghi, and a. Ougazzaden. Structural and compositional characterization of MOVPE GaN thin films transferred from sapphire to glass substrates using chemical lift-off and room temperature direct wafer bonding and GaN wafer scale MOVPE growth on ZnO-buffered sapphire. *J. Cryst. Growth*, 370:63–67, may 2013.

[147] Andreas Bibl, John A. Higginson, Huang-Fai Stephen Law, and Hsin-Hua Hu. Method of Transferring a Micro Device, 2012.

[148] Matthew A. Meitl, Zheng-Tao Zhu, Vipan Kumar, Keon Jae Lee, Xue Feng, Yonggang Y. Huang, Ilesanmi Adesida, Ralph G. Nuzzo, and John a. Rogers. Transfer printing by kinetic control of adhesion to an elastomeric stamp. *Nat. Mater.*, 5(1):33–38, 2006.

[149] Sang-Il Park, Yujie Xiong, Rak-Hwan Kim, Paulius Elvikis, Matthew A. Meitl, Dae-hyeong Kim, Jian Wu, Jongseung Yoon, Chang-jae Yu, Zhuangjian Liu, Yonggang Y. Huang, Keh-chih Hwang, Placid Ferreira, Xiuling Li, Kent Choquette, and John A. Rogers. Printed assemblies of inorganic light-emitting diodes for deformable and semitransparent displays. *Science*, 325(5943):977–981, 2009.

[150] Hoon-sik Kim, Eric Brueckner, Jizhou Song, Yuhang Li, Seok Kim, Chaofeng Lu, Joshua Sulkin, Kent Choquette, Yonggang Huang, Ralph G Nuzzo, and John A. Rogers. Unusual strategies for using indium gallium nitride grown on silicon (111) for solid-state lighting. *Proc. Natl. Acad. Sci. U. S. A.*, 108(25):10072–10077, 2011.

[151] Gholamreza Chaji. Selective transfer of micro devices, 2017.

[152] Reza Chaji, Fathi Ehsan, and Afshin Zamani. Low-Cost Micro-LED Displays for All Applications. *SID 2017 Dig.*, pages 264–267, 2017.

[153] David Hwang, Benjamin P. Yonkee, Burhan Saif Addin, Robert M. Farrell, Shuji Nakamura, James S. Speck, and Steven DenBaars. Photoelectrochemical liftoff of LEDs grown on freestanding c-plane GaN substrates. *Opt. Express*, 24(20):22875, oct 2016.

[154] Ludovico Megalini, Leah Y. Kuritzky, John T. Leonard, Renuka Shenoy, Kenneth Rose, Shuji Nakamura, James S. Speck, Daniel A. Cohen, and Steven P. DenBaars. Selective and controllable lateral photoelectrochemical etching of nonpolar and semipolar InGaN/GaN multiple quantum well active regions. *Appl. Phys. Express*, 8(6):066502, 2015.

[155] Benjamin P. Yonkee, Burhan SaifAddin, John T. Leonard, Steven P. DenBaars, and Shuji Nakamura. Flip-chip blue LEDs grown on (20-21) bulk GaN substrates

utilizing photoelectrochemical etching for substrate removal. *Appl. Phys. Express*, 9:056502, 2016.

[156] Casey O. Holder, John T. Leonard, Robert M. Farrell, Daniel A. Cohen, Benjamin P. Yonkee, James S. Speck, Steven P. DenBaars, Shuji Nakamura, and Daniel F. Feezell. Nonpolar III-nitride vertical-cavity surface emitting lasers with a polarization ratio of 100% fabricated using photoelectrochemical etching. *Appl. Phys. Lett.*, 105(3):031111, jul 2014.

[157] John T. Leonard, Benjamin P. Yonkee, Daniel A. Cohen, Ludovico Megalini, Seunggeun Lee, James S. Speck, Steven P. Denbaars, and Shuji Nakamura. Nonpolar III-nitride vertical-cavity surface-emitting laser with a photoelectrochemically etched air-gap aperture. *Appl. Phys. Lett.*, 108(3), 2016.

[158] Chris Youtsey, Robert McCarthy, Rekha Reddy, Kamran Forghani, Andy Xie, Ed Beam, Jingshan Wang, Patrick Fay, Timothy Ciarkowski, Eric Carlson, and Louis Guido. Wafer-scale epitaxial lift-off of GaN using bandgap-selective photoenhanced wet etching. *Phys. Status Solidi Basic Res.*, 254(8), 2017.

[159] Yan Gao, Tetsuo Fujii, Rajat Sharma, Kenji Fujito, Steven P. DenBaars, Shuji Nakamura, and Evelyn L. Hu. Roughening Hexagonal Surface Morphology on Laser Lift-Off (LLO) N-Face GaN with Simple Photo-Enhanced Chemical Wet Etching. *Jpn. J. Appl. Phys.*, 43(5A):L637–L639, apr 2004.

[160] Hock M. Ng, Nils G. Weimann, and Aref Chowdhury. GaN nanotip pyramids formed by anisotropic etching. *J. Appl. Phys.*, 94(1):650, 2003.

[161] Yan Gao, M. D. Craven, James S. Speck, Steven P. DenBaars, and Evelyn L. Hu. Dislocation- and crystallographic-dependent photoelectrochemical wet etching of gallium nitride. *Appl. Phys. Lett.*, 84(17):3322–3324, 2004.

[162] Tetsuo Fujii, Yan Gao, Rajat Sharma, Evelyn L. Hu, Steven P. DenBaars, and Shuji Nakamura. Increase in the extraction efficiency of GaN-based light-emitting diodes via surface roughening. *Appl. Phys. Lett.*, 84(6):855–857, 2004.

[163] Dongsheng Li, M. Sumiya, S. Fuke, Deren Yang, Duanlin Que, Y. Suzuki, and Y. Fukuda. Selective etching of GaN polar surface in potassium hydroxide solution studied by x-ray photoelectron spectroscopy. *J. Appl. Phys.*, 90(8):4219, 2001.

[164] M. S. Minsky, M. White, and Evelyn L. Hu. Room-temperature photoenhanced wet etching of GaN. *Appl. Phys. Lett.*, 68(11):1531–1533, 1996.

[165] Reena Khare and Evelyn L Hu. Dopant Selective Photoelectrochemical Etching of GaAs Homostructures. *J. Electrochem. Soc.*, 138(5):1516–1519, 1991.

[166] Reena Khare, D. B. Young, and Evelyn L. Hu. The Bandgap-Selective Photoelectrochemical Etching of GaAs / AIGaAs Heterostructures with Varying Mole Fraction. *J. Electrochem. Soc.*, 140(7):L117, 1993.

[167] J. van de Ven and H. J. P. Nabben. Anisotropic Photoetching of III-V Semiconductors. *J. Electrochem. Soc.*, 137(5), 1990.

[168] T. Rotter, D. Mistele, J. Stemmer, F. Fedler, J. Aderhold, J. Graul, and M. Heuken. Photoinduced oxide film formation on n-type GaN surfaces using alkaline solutions. *Appl. Phys. Lett.*, 76(26):3923–3925, 2000.

[169] A. R. Stonas, P. Kozodoy, H. Marchand, P. Fini, Steven P. DenBaars, Umesh K. Mishra, and Evelyn L. Hu. Backside-illuminated photoelectrochemical etching for the fabrication of deeply undercut GaN structures. *Appl. Phys. Lett.*, 77(16):2610–2612, 2000.

[170] Yan Gao. *Highly Selective PEC Etching of GaN Device Structures*. PhD thesis, Universiy of California, Santa Barbara, 2004.

[171] D. Segev and C. G. Van de Walle. Origins of Fermi-level pinning on GaN and InN polar and nonpolar surfaces. *Europhys. Lett.*, 76(2):305–311, oct 2006.

[172] Adele C. Tamboli. *Photoelectrochemical Etching of GaN for High Quality Optical Devices*. PhD thesis, University of California, Santa Barbara, 2009.

[173] Chris Youtsey, I Adesida, L. T. Romano, and G. Bulman. Smooth n-type GaN surfaces by photoenhanced wet etching. *Appl. Phys. Lett.*, 72(5):560–562, 1998.

[174] E. D. Haberer, Rajat Sharma, A. R. Stonas, Shuji Nakamura, Steven P. DenBaars, and Evelyn L. Hu. Removal of thick (>100 nm) InGaN layers for optical devices using band-gap-selective photoelectrochemical etching. *Appl. Phys. Lett.*, 85(5):762, 2004.

[175] T. Palacios, F. Calle, M. Varela, C. Ballesteros, E. Monroy, F. B. Naranjo, M. A. Sánchez-García, E. Calleja, and E. Muñoz. Wet etching of GaN grown by molecular beam epitaxy on Si(111). *Semicond. Sci. Technol.*, 15(10):996–1000, oct 2000.

[176] W. Guo, J. Xie, C. Akouala, S. Mita, A. Rice, J. Tweedie, I. Bryan, R. Collazo, and Z. Sitar. Comparative study of etching high crystalline quality AlN and GaN. *J. Cryst. Growth*, 366:20–25, mar 2013.

[177] X. H. Wu, C. R. Elsass, A. Abare, M. Mack, Stacia Keller, Pierre M Petroff, Steven P. DenBaars, and James S. Speck. Structural origin of V-defects and correlation with localized excitonic centers in InGaN / GaN multiple quantum wells. *Appl. Phys. Lett.*, 72(6):692–694, 1998.

[178] Yuji Zhao, Feng Wu, Chia-Yen Huang, Yoshinobu Kawaguchi, Shinichi Tanaka, Kenji Fujito, James S. Speck, Steven P. DenBaars, and Shuji Nakamura. Suppressing void defects in long wavelength semipolar (2021) InGaN quantum wells by growth rate optimization. *Appl. Phys. Lett.*, 102(9):091905, 2013.

[179] John T. Leonard, Erin C. Young, Benjamin P. Yonkee, Daniel A. Cohen, Chao Shen, Tal Margalith, T. K. Ng, Steven P. DenBaars, Boon S. Ooi, James S. Speck, and Shuji Nakamura. Comparison of nonpolar III-nitride vertical-cavity surface-emitting lasers with tunnel junction and ITO intracavity contacts. Number February 2016, page 97481B, feb 2016.